Numerical coupling of thermal-electric network models and energy-transport equations including optoelectronic semiconductor devices

Dissertation
zur Erlangung des Grades
Doktor der Naturwissenschaften

Am Fachbereich Physik, Mathematik und Informatik
der Johannes Gutenberg-Universität Mainz

Markus Brunk,
geboren in Idar-Oberstein

Mainz, 2008

Tag der mündlichen Prüfung: 11. März 2008

Abstract

In this work the numerical coupling between electric and thermal network as well as electronic and optoelectronic semiconductor device models is treated. An overview over electric and thermal network modeling as well as the hierarchy of semiconductor models is given.

For electric network modeling the modified nodal approach (MNA) is applied what results in a system of differential-algebraic equations. Thermally the network is modeled by an accompanying thermal network resulting in a system of differential or differential-algebraic equations of parabolic type.

Semiconductor devices are modeled by use of the energy-transport model. The model allows for the computation of the charge carrier temperature and thus accounts for local thermal effects in the device. In this work the energy-transport model is extended to a model for optoelectronic devices like laser and photo diodes for the first time. Mathematically, the energy-transport equations constitute a elliptic-parabolic cross-diffusion system. It can be written in a drift-diffusion-type formulation, which allows for an efficient numerical approximation. For more detailed thermal consideration of devices non isothermal crystal lattice modeling is included. The temperature of the crystal lattice is modeled by the heat flow equation. The corresponding energy conserving source term is derived under thermodynamical and phenomenological considerations of energy fluxes.

The coupling of the different subsystems is described. We follow the approach to include the energy-transport model into the network equations directly. The heat flow equation for the lattice temperature is included into the accompanying thermal network model. The final thermoelectric network-device model results in a coupled system of *partial differential-algebraic equations (PDAE)*.

For numerical examples we consider the case of one-dimensional devices. For space discretization of the device equations a hybridized mixed finite element scheme is applied that allows to maintain the continuity of the device current and the positivity of charge carrier densities. Exponential fitting is applied for good approximation in the convection dominated case. To keep positivity of charge carriers also for the coupled system and to account for the differential algebraic character of the system backward difference formulas are applied for time discretization.

For efficient solution of the coupled system resulting from optoelectronic device modeling and thermoelectric network device coupling, iterative solvers are presented. Numerical examples are presented for (opto)electronic network device coupling. A focus is on the numerical results for semiconductor devices including non-isothermal crystal lattice. Finally numerical results for a complete thermoelectrically simulated circuit are presented.

Contents

II. Discretization and numerical solution of thermoelectric coupled network-device systems

Introduction

The advance in telecommunications and computer technology within the last decades is representative for the technological progress of the society. This highly visible progress is strongly driven by the development of new and more powerful electronic and optoelectronic devices and integrated circuits. On nowadays chips millions of network elements are included. The ongoing miniaturization of single elements and integrated circuits, leading from micro- to nanotechnology, will allow for increasing performance in telecommunications in the near future.

Chip design and development strongly depends an reliable circuit simulation, predicting the electrical behavior of circuits before the expensive production of prototypes. Thus, reliable circuit simulators will serve as time- and money-saving tool in application and speed up the technological progress.

In traditional circuit simulators semiconductor devices are replaced by compact circuits consisting of basic elements (resistances, capacitances, inductances and sources) rebuilding the electrical behavior of the device. This strategy was advantageous up to now since integrated circuit simulation was possible without computationally expensive device simulation. Miniaturization, however, leads to smaller devices driven by higher frequencies. Parasitic and local thermal effects occur and may become predominant. This requires to take into account a very large number of basic elements and adjust carefully a large number of parameters to achieve required accuracy. Moreover device heating and localization of hot spots are not covered by the compact model approach.

This makes it preferable to employ distributed models for the electric and thermal description of devices. The first approaches to couple circuits and devices were based on an extension of existing device simulators by more complex boundary conditions [**67**, **82**] or the combination of device simulators with circuit simulators as a "black box" solver [**37**]. Both approaches, however, are not suitable for complex circuits in the high-frequency domain.

The mathematical analysis and numerical approximation of coupled network and device equations were studied only recently. The first mathematical results were obtained in [**41**, **44**] where a semiconductor device was coupled to a simple circuit in such a way that the currents entering the de-

vice can be expressed by a function of the applied voltage. In this case, the network is treated only as a special boundary condition for the semiconductor. This approach fails for integrated circuits.

Later, networks containing semiconductor devices described by the drift-diffusion equations were studied. An existence analysis containing the drift-diffusion model was developed in [**4, 5**]. In [**97, 98**] it is shown that the index of the coupled network-device system for devices modeled by the drift-diffusion equations is at most two under weak conditions on the circuit (local passivity, no shortcuts). The exact index depends on the topology of the circuit. The same results were obtained in [**88**] for the discretized drift-diffusion equations. For detail we refer also to the review paper [**48**].

For optoelectronic devices the semiconductor model has to be enhanced in order to capture the optical effects. In [**13, 78**] models for laser diodes based on the drift-diffusion model have been proposed. Corresponding models for photo diodes have been presented in [**59, 31, 55**].

The advantages of the coupled system of network and drift-diffusion equations compared to the compact model approach are numerous. Thermal effects, however, are not taken into account.

To allow for thermal effects in devices more complex semiconductor models including the consideration of the thermal energy can be applied. The first so-called energy-transport model has been derived in 1962 by Stratton [**92**]. Additionally to the drift-diffusion model Stratton considers the temperature of the charge carriers and thus allows for thermal effects. Since then different energy-transport models have been presented [**18, 19**]. A widespread energy-transport model is presented by Chen et. al. in [**27**]. The model can be derived from the semi-classical Boltzmann equation in the diffusion limit under the assumption of dominant electron-electron scattering [**19**]. It consists of the conservation laws for the electron density and the electron energy density with constitutive relations for the particle and energy current densities, coupled to the Poisson equation for the electric potential. Mathematically, the energy-transport equations (without the Poisson equation) constitute a parabolic cross-diffusion system in the entropic variables [**33**]. The system can be written in a drift-diffusion-type formulation, which allows for an efficient numerical approximation [**34**].

A more accurate thermal description of the device is achieved by additionally allowing non-constant temperature of the crystal lattice. Non isothermal lattice modeling started in the 70s, when the carrier transport in the devices was modeled by the drift-diffusion equations. Up to now the widespread approach is to model the lattice temperature by the heat flow equation. In the past, different source terms for the heat flow equation coupled to the drift-diffusion equations have been proposed [**1, 30, 42, 87, 89**]. In [**101**] Wachutka gave the first derivation of a source term for the heat flow equation coupled to the energy-transport model for the carrier transport.

Thermal effects in circuit simulation has been taken into account only

recently. Due to miniaturization and increasing packing density of network elements thermal effects and thermal interaction can no longer be neglected, as device heating influences material parameters and thus influences the electrical performance of the entire circuit. The common approach is to model the heat effects in circuits by providing an accompanying thermal network consisting of lumped and distributed thermal elements. This thermal network model is established in [**20, 36**], where the heat exchange of the network elements with the environment is taken into account. The mutual thermal interference of the circuit elements is not considered. In [**16, 17**] the model has been extended such that thermal interaction between lumped and distributed thermal elements could be taken into account. Semiconductor devices, however, have been considered as lumped thermal elements with a constant temperature. This is a proper model only for semiconductor devices with very high thermal conductivity or devices where local thermal effects do not have strong influence on the electrical behavior of the devices.

Compendious, the ingredients for complete thermoelectric modeling and simulation of optoelectronic circuit-device systems are largely given. Nonetheless the proper coupling of all mentioned models and effects builds a cumbersome task.

Outline of the thesis

In this work we will describe the numerical coupling of electric and thermal network equations with energy-transport and heat flow equations to allow for a detailed thermoelectric simulation of circuit-device systems. We will follow and extend the approach of [**97, 98**] and include the energy-transport model into the network equations directly. Compared to the coupling with the drift-diffusion equations, we are able to simulate the electron temperature what allows for the consideration of (local) thermal effects in the devices. We will apply (non-standard) boundary conditions of Robin-type and will give numerical examples clarifying the drawback of Dirichlet boundary conditions in bipolar devices. We will model the lattice temperature of the devices by the heat flow equation. The source term for the heat flow equation will be derived under thermodynamic considerations and differs slightly from the source term described by Wachutka in [**101**]. The heat flow equation will be included into the accompanying thermal network model described in [**16, 17**].

As the device model is described by partial differential equations (of parabolic type) and the network equations are given by differential-algebraic equations (DAE), this results in a coupled system of *partial differential-algebraic equations (PDAE)*.

This work is separated into two parts. The first part, consisting of the chapters 1 to 4, describes the complete modeling of thermoelectric network

device systems. Chapters 1 and 2 contain the modeling of electric and thermal networks without inclusion of semiconductor devices. Chapter 3 is devoted to the modeling of semiconductor devices. We give a short overview of the hierarchy of semiconductor models and present the energy-transport and drift-diffusion model. Moreover we extend the energy-transport model to the application to optoelectronic devices like laser and photo diodes. Finally we derive under thermodynamic considerations a source term for the heat flow equation for distributed modeling of the crystal lattice temperature of the device. As closure of part one, in chapter 4 the complete coupling of thermal and electric network equations with the energy-transport, drift-diffusion and heat flow equations is presented.

The second part is concerned with the special numerical treatment and the numerical examples. In chapter 5 we state the nondimensionalization of the coupled system. Chapter 6 is devoted to the discretization of the coupled system. We apply backward difference formulas for time discretization in order to take into account the differential algebraic character of the system. Moreover we describe the discretization of the device equations using a hybridized mixed finite element scheme that allows for good approximation of the current values and the charge carrier densities. In chapter 7 the applied iterative algorithms for solution of the complete model and the solution of different subsystems are presented. Finally in chapter 8 we present the numerical examples to clarify the importance of inclusion of thermal effects into the simulation of single semiconductor devices as well as circuit-device systems.

Part I

Thermoelectric modeling of semiconductor devices and integrated circuits

Chapter 1

Electric network modeling

Simulation of electric circuits requires proper modeling of networks. However, proper models for electric circuits have to fulfill two properties. On the one hand the physical behavior of the circuit has to be rebuilt with highest possible accuracy. On the other hand the model has to be as simple as possible in order to reduce the numerical effort that is necessary to solve the model equations.

A well accepted approach as compromise between these two obviously conflicting properties is to consider the electric network as a directed graph containing branches and nodes only. Thereafter the node potentials are defined with respect to one arbitrarily chosen reference node and the branch currents and branch voltages are introduced.

Each branch thereby corresponds to a network element, whose physical behavior is given as a direct relation between the branch current i and the branch voltage v. The characteristic current-voltage relations of the different types of network elements will be described below. Thereby we distinguish between two types of branches:

- current-defined branches
  The branch current is given in terms of circuit and device parameters.

- voltage-defined branches
  The branch voltage is given in terms of circuit and device parameters.

Besides the current-voltage characteristics of the network elements the network topology has to be considered in order to take into account the mutual interference of the network elements. The network topology will be described by the Kirchhoff laws, as we will see below.

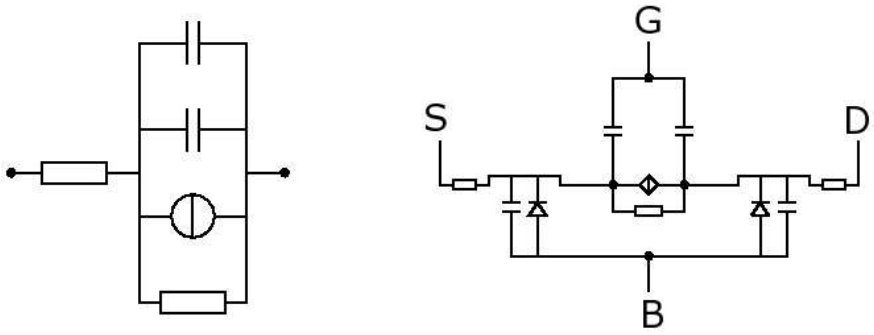

Figure 1.1: Low level compact models of a *pn* diode (left) and a MOSFET (right)

1.1 Network elements

To model electric circuits, it is necessary to approximate the real network elements by adequate models. The models for circuit elements cover a wide range of complexity depending on the complexity of the element and the needed accuracy of the describing model. The models range from simple algebraic equations for linear resistances, for instance, up to quantum mechanical models based on the Schrödinger equation for semiconductor devices like transistors.

As in integrated circuits and on computer chips the number of semiconductor devices is very high and can reach several millions, such a detailed modeling and simulation for all devices is numerically impracticable. Thus we have to restrict ourselves to simple models for most of the devices.

The common approach to construct simple models for semiconductor devices is to replace them by so-called compact models. These are equivalent circuits of basic network elements rebuilding the electrical behavior of the complex device. The basic elements are described by simple algebraic or ordinary differential equations, such that semiconductor devices are modeled by a system of these simple equations. In figure 1.1 we see a low level compact model for a *pn* diode, consisting of a current source, capacitances and resistances. Additionally, we see a compact model for a MOSFET (metal oxide semiconductor field effect transistor), consisting of a voltage source, capacitances, resistances and diodes, which in turn have to be replaced by the corresponding equivalent circuit. The depicted low level models enforce a set of five parameters for the diode and 18 parameters for the MOSFET to be fitted.

The size of the equivalent circuits depends strongly on the complexity of the device and the needed accuracy of the model. Ongoing miniaturization of integrated circuits and semiconductor devices leads to parasitic effects in devices - like thermal effects and increasing signal to noise ratio - which have

significant impact on the electrical behavior of the devices. They have to be taken into account what leads to further increase of the size of compact models.

The development of compact models is far from being trivial and forms an own field of research. In [61], for instance, it is suggested to determine compact models and adjust the corresponding parameters from measurement and simulation data by us of neural networks.

Compact models for nowadays transistors can consist of up to 800 parameters. The adjustment of these parameters is a very time-consuming work and requires many laboratory tests or detailed numerical simulations of the device.

This makes it preferable to use distributed models for semiconductor devices instead, as they can be applied to many devices and the parameter fitting for a single device can be omitted. As compromise between detailed and efficient modeling distributed models are applied to devices with crucial behavior for the entire circuit, only. The remaining ones are model by compact models. The inclusion of distributed semiconductor models into the circuit model will be discussed in § 4.

In this section we consider circuits consisting of basic elements. As basic elements we consider ideal resistors, capacitors, inductors and voltage and current sources. Current sources have to be considered, as they play a very important role in compact models for complex devices (see figure 1.1).

The current-voltage characteristic for a resistor is given by

$$i_R(t) = g_R(v_R(t), t), \tag{1.1}$$

where $v_R(t)$ denotes the voltage applied to the resistor and $i_R(t)$ stands for the current through the resistor. The function $g_R(v, t)$ describes the conductivity of the resistor.

In capacitors the energy is stored in the electric field. The charge of the capacitor

$$Q_C(t) = \widetilde{Q}_C(v_C(t), t)$$

depends on the applied voltage v_C. With the definition of electric current we then get for the current-voltage relation

$$i_C(t) = \frac{d\widetilde{Q}_C(v_C(t), t)}{dt}, \tag{1.2}$$

where i_C denotes the current through the capacitor.

In inductors the energy is stored in the magnetic field. The corresponding flux

$$\Phi_L(t) = \widetilde{\Phi}_L(i_L(t), t)$$

depends on the current through the inductor i_L. Thus the current-voltage relation for inductors is given by

$$v_L(t) = \frac{d\widetilde{\Phi}_L(i_L(t), t)}{dt}. \tag{1.3}$$

As voltage and current sources we consider elements, for which the voltage or current, respectively, is directly given by

$$v(t) = v_s(t) \qquad \text{or} \qquad i(t) = i_s(t). \tag{1.4}$$

If additionally the sources depend on the applied voltage or driving current, we refer to the sources as voltage or current controlled sources, see [98] for details.

1.2 Network topology

To complete the network model the network topology has to be considered in order to model the mutual electrical interference of the network elements. Neglecting quantum mechanical interaction between the elements the network model has to fulfill the Kirchhoff laws, that are:

- Kirchoff's current law (KCL)
  The sum of all currents entering and leaving one network node has to be zero
  $$\sum_{k=1}^{n} i_k = 0.$$
- Kirchhoff's voltage law (KVL)
  The sum of all branch voltages around one loop in the circuit has to be zero
  $$\sum_{k=1}^{n} v_k = 0.$$

We remark that we consider the circuit as directed graph and that each branch gets a direction. We assign one node as reference or mass node. Then the network topology is described via the following definition.

Definition 1.1. *For an electric network consisting of n_n nodes and n_b branches the (reduced) incidence matrix $\mathcal{A} = (a_{ij}) \in \mathbb{R}^{(n_n-1)\times n_b}$ describing the node to branch relation of the entire circuit (without the reference node) is defined as*

$$a_{ij} = \begin{cases} 1 & \textit{if the branch } j \textit{ leaves the node } i, \\ -1 & \textit{if the branch } j \textit{ enters the node } i, \\ 0 & \textit{else.} \end{cases} \tag{1.5}$$

With this matrix the Kirchhoff current law can be easily expressed as

$$\mathcal{A}\, i = 0, \tag{1.6}$$

where i denotes the vector containing all branch currents. Moreover the matrix can be used to express the relation between the node potentials e and the vector of all branch voltages v as

$$v = \mathcal{A}^\top e. \tag{1.7}$$

Applying (1.7) to all branches around one loop leads directly to the Kirchhoff voltage law.

With the current-voltage characteristics of the basic network elements (1.1)-(1.3) and the network topology in terms of the Kirchhoff laws (1.6) and (1.7) we have the necessary ingredients to describe the complete network model.

1.3 Nodal approach (NA)

The most simple of the described approaches to model electric circuits is the so called nodal approach (NA). The name of the approach comes from the choice of variables occurring. The only variables we namely consider are

- the node potentials e,

which have been determined with respect to the reference node. This guarantees Kirchhoff's voltage law. With these variables the KCL is stated for each node except for the reference node and the resulting system of equations stands as model for the entire circuit.

For simple circuits containing conductances and current sources only, the NA leads to a final system of equations with good condition as the resulting matrix is diagonally dominant. For circuits containing current sources the final system however looses this stability property [**43**]. The big disadvantage of the nodal approach is, however, that it only allows for current-defined branches. Voltage-defined branches however can only be included by use of gyrators as in [**91**] and [**95**]. Moreover, ideal voltage sources and current controlled elements can not be modeled, as for these elements the current necessarily has to be considered. The effort to include current dependencies in this approach leads to small or even negative resistances what results in numerical instabilities, see [**90**].

1.4 Modified nodal approach (MNA)

In order to overcome the disadvantages of the nodal approach and allow for an adequate modeling of voltage sources and current controlled elements

the modified nodal approach has been introduced [**54**]. It is based on the same simple idea as the NA, but as additional variables the currents in the voltage-defined branches are considered (see below). This change, however, allows for a proper modeling of more complex circuits, as voltage defined branches can be easily included. This complexity combined with its simplicity is the reason for the large popularity of the MNA. It has been employed in SPICE, the standard circuit simulator developed at the university of Berkeley [**76**] and the circuit simulator TITAN developed by SIEMENS / Infineon Technologies / Qimonda, for instance.

The basic tools for the MNA are the Kirchhoff laws in form of the network equations (1.6) and (1.7)

$$\mathcal{A}\, i = 0 \tag{1.8}$$

$$v = \mathcal{A}^\top e \tag{1.9}$$

with the incidence matrix $\mathcal{A}$ described in (1.5). Moreover we need the current-voltage characteristics of the basic elements (1.1)-(1.3)

$$i_R(t) = g_R(v_R(t), t), \quad i_C(t) = \frac{d\widetilde{Q}_C(v_C(t), t)}{dt}, \quad v_L(t) = \frac{d\widetilde{\Phi}_L(i_L(t), t)}{dt}, \tag{1.10}$$

and the given current and voltage sources (1.4)

$$v(t) = v_s(t) \qquad \text{or} \qquad i(t) = i_s(t). \tag{1.11}$$

The classical modified nodal approach

In the classical approach the set of variables is increased (compared to the NA) by the currents in the voltage-defined branches. Thus we consider as variables

- the node potentials e,
- the currents through the voltage-defined (or current-controlled) elements i_L and i_v.

In the modified nodal approach we replace the branch currents of all current-defined elements in (1.8) by the corresponding relations in (1.10) and additionally replace all branch voltages by the node potentials according to (1.9).

Further on, the network branches are numbered in such a way that the incidence matrix forms a block matrix with blocks describing the different types of the network elements, i.e.

$$\mathcal{A} = (\mathcal{A}_R, \mathcal{A}_C, \mathcal{A}_L, \mathcal{A}_I, \mathcal{A}_V),$$

where the index indicates the resistive, capacitive, inductive and current and voltage source branches. With that we finally get the differential algebraic system of equations

$$\begin{aligned}\mathcal{A}_C\mathcal{C}(\mathcal{A}_C^\top e,t)\mathcal{A}_C^\top\frac{de}{dt}+\mathcal{A}_C\frac{\partial\widetilde{Q}_C}{\partial_t}(\mathcal{A}_C^\top e,t)&\\ +\mathcal{A}_R g_R(A_R^\top e,t)+\mathcal{A}_L i_L+\mathcal{A}_V i_V=-\mathcal{A}_I i_s(t),&\qquad(1.12)\\ \mathcal{L}(i_L,t)\frac{di_L}{dt}+\frac{\partial\widetilde{\Phi}_L}{\partial_t}(i_L,t)-\mathcal{A}_L^\top e=0,&\qquad(1.13)\\ \mathcal{A}_V^\top e=v_s(t),&\qquad(1.14)\end{aligned}$$

with

$$\mathcal{C}(v,t):=\frac{\partial\widetilde{Q}_c}{\partial v}(v,t),\qquad \mathcal{L}(i,t):=\frac{\partial\widetilde{\Phi}_L}{\partial i}(i,t).\qquad(1.15)$$

The charge oriented modified nodal approach

In the charge oriented modified nodal approach we additionally consider the charge of the capacitances and the flux of the inductances as variables. All in all the set of variables consists of

- the node potentials e,
- the currents through the voltage-defined elements i_L and i_v,
- the charge of the capacitances Q_C
- the flux of the inductances Φ_L.

With those variables we get the system equivalent to (1.12)-(1.14)

$$\begin{aligned}\mathcal{A}_C\frac{dQ_C}{dt}+\mathcal{A}_R g_R(\mathcal{A}_R^\top e)+\mathcal{A}_L i_L+\mathcal{A}_v i_v=-\mathcal{A}_i i_s,&\qquad(1.16)\\ \frac{d\Phi_L}{dt}-\mathcal{A}_L^\top e=0,&\qquad(1.17)\\ \mathcal{A}_v^\top e=v_s&\qquad(1.18)\\ Q_C=\widetilde{Q}_C(\mathcal{A}_C^\top e,t),&\qquad(1.19)\\ \Phi_L=\widetilde{\Phi}_L(i_L,t).&\qquad(1.20)\end{aligned}$$

As the dimension of this system is larger than the dimension of system (1.12)-(1.14) it might seem to be disadvantageous. However, it is the main approach used in industrial circuit simulators, as it has many advantages in relation to the classical approach. These advantages are based on physical, modeling as well as numerical considerations.

In semiconductor physics charges and fluxes are primal variables used to describe charge- and flux-storing elements in semiconductor devices. Thus compact models are mainly given in a charge oriented formulation. Moreover in the charge oriented formulation (1.16)-(1.20) charge conservation is fulfilled exactly. The classical approach (1.12)-(1.14) can be derived from the charge oriented one by the derivatives given in (1.15). Thus the two systems are analytically equivalent. By differentiation, however, we loose information on the charge and flux, what finally leads to the fact that in numerical approximation the physically reasonable property of charge conservation is only fulfilled approximately.

Furthermore the classical approach does not allow for a physical model of transistors covering charge conservation and the reciprocal flux of charges [**46**], at once. The advantages of the charge oriented MNA compared to the classical MNA are numerous and a detailed description can be found in [**45**] and [**46**].

Moreover due to the simplicity of equations (1.19) and (1.20) only function evaluations are needed to determine the values for Q_C and Φ_L. Thus the numerical treatment of the charge oriented system does not enforce more numerical effort than the evaluation of the classical approach. The system that has to be treated numerically reads

Electric network equations

$$\mathcal{A}_C \frac{d\widetilde{Q}_C}{dt}(\mathcal{A}_C^\top e, t) + \mathcal{A}_R g_R(\mathcal{A}_R^\top e) + \mathcal{A}_L i_L + \mathcal{A}_v i_v = -\mathcal{A}_i i_s, \tag{1.21}$$

$$\frac{d\widetilde{\Phi}_L}{dt}(i_L, t) - \mathcal{A}_L^\top e = 0, \tag{1.22}$$

$$\mathcal{A}_v^\top e = v_s. \tag{1.23}$$

In the final system achieved by the MNA the equations (1.12), (1.21) state the Kirchhoff current law for the entire circuit, equations (1.13), (1.22) describe the voltage-current characteristics for inductors and the equations (1.14), (1.23) determine the node potentials in the nodes adjacent to the given voltage sources.

Equations (1.21)-(1.23) represent a system of differential-algebraic equations (DAE) with a properly stated leading term [**70, 71**] if the matrices $\mathcal{C}(v,t)$ and $\mathcal{L}(i,t)$ in (1.15) are positive definite for all arguments v, i, and t. Under the assumptions that the matrices $\mathcal{C}$, $\mathcal{L}$, and $\mathcal{G} = \partial g_R/\partial v$ are positive definite and that the circuit does neither contain loops of voltage sources only nor cutsets of current sources only, it is proved in [**97, 99**] that the (tractability) index of the DAE system is at most two. Furthermore, if the circuit does neither contain LI-cutsets nor CV-loops with at least one voltage source then the index is at most one.

Initial conditions The system (1.21)-(1.23) has to be completed by initial conditions for the variables e, i_L and i_v, actually also for $\widetilde{Q}_C$ and $\widetilde{\Phi}_L$. We assume the initial conditions

$$e(0) = e_I, \quad i_L(0) = i_{L,I}, \quad i_v(0) = i_{v,I}.$$

The corresponding initial values for $\widetilde{Q}_C$ and $\widetilde{\Phi}_L$ can then be determined from (1.19) and (1.20). We remark that the choice of initial values is not arbitrary. Since the system of network equations is of differential-algebraic type, the initial values have to be consistent. For consistent initialization of DAEs we refer to [**39**] and [**64**].

Chapter 2

Thermal network modeling

In this chapter we describe the thermal network model given in [**16, 17**] without special consideration of semiconductor devices. A detailed description of thermal effects in semiconductor devices will be given in § 3.4. In § 4.2 we then describe the coupling of the detailed thermal semiconductor model with the thermal network.

2.1 Thermal network topology

For industrial purposes the model of the thermal network has to rebuild the thermal behavior of the network elements as accurate as possible, but on the other hand the final model has to be as simple as possible in order to allow for cheap computations. The widespread compromise is to model all thermally relevant elements in a circuit by zero- or one-dimensional structures. We distinguish between:

- Lumped thermal elements,
  that are thermally relevant elements with very small spatial extension or very high thermal conductivity such that the temperature can be assumed to be constant. These elements are modeled as 0D-elements and the associated temperature is denoted by $\hat{T}^l(t)$. Lumped elements can be, for instance, resistors with high thermal conductivity, metal contacts or any other tiny element in the network. Semiconductor devices with high thermal conductivity can be modeled as lumped thermal element, if local thermal effects are not critical for the electrical behavior of the considered device and thus for the entire circuit.

- Distributed thermal elements,
  that are space distributed elements whose electrical behavior depends

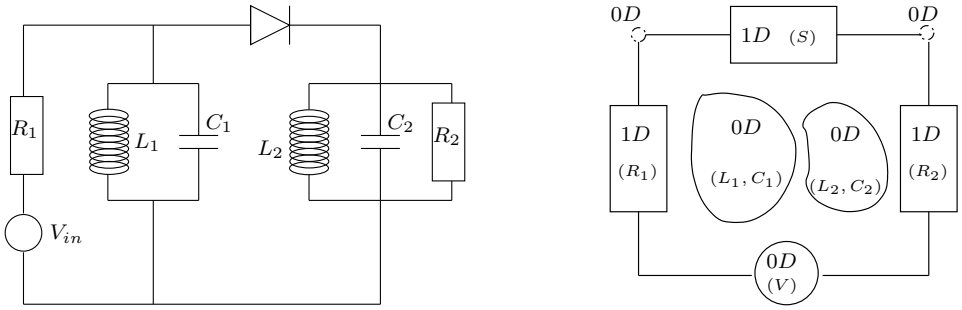

Figure 2.1: Circuit diagram of a frequency multiplier (left) and a schematic draw of a corresponding thermal network (right).

on the space distributed temperature. They are modeled by one-dimensional thermal lines characterized by the interval $I_{\text{th}} = [0, L_{\text{th}}]$. The distributed temperature associated with a thermal line is denoted by $T^d(x,t)$. Thermal lines can be resistors with small thermal conductivity, interconnects or even macrostructures on computer chips or integrated circuits. Semiconductor devices can be modeled as thermal lines what allows for a rough consideration of local thermal effects.

Lumped thermal elements are usually elements of the electric network, the distributed ones do not necessarily belong to the electric network.

In order to characterize the network topology we have to define the nodes and branches of the thermal network (according to § 1). The suggestive assumption to use the lumped thermal elements as network nodes and the distributed thermal elements as branches is not a proper choice, as in the hitherto described model all possible interfaces between lumped and distributed (e.g. lumped-lumped, distributed-distributed) elements can occur.

The structure of the different couplings depend on the dimension of the connected elements. The general concept of coupling, however, is that the elements are coupled via a flux across the boundary of the distributed elements and, moreover, adjacent elements are coupled by a common interface. Thus they have a common temperature at this interface what is assigned in terms of (Dirichlet) boundary conditions. Accordingly, adjacent lumped elements have the same temperature and can be considered as a 0D-unit with one temperature $\hat{T}$ only. Furthermore, we identify the temperature at the interfaces of connected distributed elements and assign this temperature to an artificial lumped element without thermal mass.

This way we end up with a network containing lumped-distributed interfaces only. In this network the nodes are represented by the 0D-units and the branches by the distributed elements.

We remark, that the resulting thermal network not necessarily has to be connected. If the electric devices are connected by thermally irrelevant

or thermally nonconducting elements, the thermal network can consist of several sub-networks. In Figure 2.1 we see the schematic draw of a thermal network corresponding to the circuit diagram of a frequency multiplier. If we model the inductances, capacitances and the voltage source thermally lumped, the resistances and the semiconductor device thermally distributed, we get a not connected thermal network including two artificial 0D-units.

To identify the temperature $\hat{T}^l$ of the lumped elements with the temperature $\hat{T}$ of the corresponding 0D-units we introduce the following matrix:

Definition 2.1. *For a thermal network with m_l lumped thermal elements described by m_n thermal nodes, we define the matrix $\mathcal{M} = (m_{ij}) \in \mathbb{R}^{m_n \times m_l}$ as:*

$$m_{ij} = \begin{cases} 1 & \text{if the lumped element } j \text{ belongs to the thermal node } i, \\ 0 & \text{else.} \end{cases}$$

Lemma 2.1. *Denoting the vector containing the temperatures of all lumped elements by $\hat{\boldsymbol{T}}^l$ and the vector containing the temperatures of all 0D-units by $\hat{\boldsymbol{T}}$ it holds*

$$\hat{\boldsymbol{T}} = \mathcal{M}\, \hat{\boldsymbol{T}}^l,$$

with the matrix $\mathcal{M}$ defined in Definition 2.1.

Having introduced the thermal nodes and the thermal branches, we can describe the network topology by an incidence matrix. We remark that in each thermal line we distinguish between the contact at $x = 0$ and the one at $x = L_{\text{th}}$ in the spatial model. This corresponds to the consideration of a directed graph when we defined the incidence matrix for the electric network (see § 1).

Definition 2.2. *For the thermal network with m_n thermal nodes and m_d thermal lines the thermal incidence matrix $\mathcal{A}_d^{\text{th}} = (a_{ij}) \in \mathbb{R}^{m_n \times 2m_b}$ is given by*

$$a_{ij} = \begin{cases} 1 & \text{if contact at } x = 0 \text{ of branch } j \text{ is connected to node } i, \\ 1 & \text{if contact at } x = L_{\text{th}} \text{ of branch } j - m_d \text{ is connected to node } i, \\ 0 & \text{else.} \end{cases} \tag{2.1}$$

In [**6, 16**] the incidence matrix $\mathcal{A}_d^{\text{th}}$ is defined via the incidence matrix of the electric network. Therefor it is necessary to identify the nodes of the electric network with the nodes of the thermal network. The resulting thermal incidence matrix is the same as $\mathcal{A}_d^{\text{th}}$ in Definition 2.2. However, if we follow the definition in [**6, 16**] electric nodes always have to be thermal nodes. Thus, for instance, interconnects that have been considered as nodes in the electric network can not be modeled thermally distributed. The direct definition of the incidence matrix $\mathcal{A}_d^{\text{th}}$ in Definition 2.2 allows for that.

2.2 Network components

Lumped elements and thermal nodes

We recall that, when considering the lumped thermal elements and the thermal nodes, we have to distinguish three things. We have to differ between the lumped elements, artificial lumped elements and 0D-units. The lumped elements correspond to physical thermally relevant devices in the network, whereas the 0D-units are combinations of eventually several adjacent lumped elements. The artificial lumped elements are models for the contacts between distributed elements and do not have a physical extension or mass. Each artificial lumped element simultaneously builds one 0D-unit.

The lumped elements are thermally modeled by the lumped version of the heat flow equation for the corresponding temperature $\hat{T}^l$

$$\hat{M} d_t \hat{T}^l = \hat{F}^d - \hat{S}(\hat{T}^l - T_{\text{env}}) + \hat{P}. \tag{2.2}$$

There $\hat{M} = \hat{c}^l \hat{\rho}^l \hat{V}^l$ denotes the thermal mass of the element, which is given as the product of the heat capacity $\hat{c}^l$, the material density $\hat{\rho}^l$ and the physical volume $\hat{V}^l$. $\hat{S}$ describes the lumped transmission coefficient that models the radiation to the environment with temperature T_{env}, and is usually considered to be proportional to the physical surface of the modeled device. $\hat{P}$ denotes the electro-thermal source of the lumped element caused by Joule heat, for instance, and will be described when considering the electro-thermal coupling in § 4.3. $\hat{F}^d$ describes the heat flux coming from the distributed elements and is part of the coupling conditions described in § 2.3. Equation (2.2) is completed by the initial condition $\hat{T}^l(0) = \hat{T}^l_I$.

For the artificial 0D-elements the lumped heat flow equation has to be fulfilled, as well. As for the artificial elements thermal mass, radiation and electro-thermal source vanish, the equation results in

$$0 = \hat{F}^d, \tag{2.3}$$

with the flux from the connected distributed elements $\hat{F}^d$. Equation (2.3) simply describes that the complete flux into the artificial element sums up to zero and the thermal inflow equals the thermal outflow.

With the thermal description of the lumped elements we can proceed to the thermal description of the thermal nodes. Having m_l (artificial) lumped thermal elements with thermal masses $\hat{M}_1, \dots, \hat{M}_{m_l}$, transmission functions $\hat{S}_1, \dots, \hat{S}_{m_l}$ and electro-thermal sources $\hat{P}_1, \dots, \hat{P}_{m_l}$ by use of the matrix $\mathcal{M}$ from Definition 2.1 we define the diagonal matrix $\hat{\boldsymbol{M}}$ containing the thermal masses of the thermal nodes (0D-units) by

$$\hat{\boldsymbol{M}} = \mathcal{M} \operatorname{diag}(\hat{M}_1, \dots, \hat{M}_{m_l}) \mathcal{M}^\top,$$

where the thermal mass of each unit is given by the sum of the masses of the elements belonging to this unit.

Analogously we define the transmission function for the thermal nodes by

$$\hat{\boldsymbol{S}} = \mathcal{M}\,\mathrm{diag}(\hat{S}_1, \ldots, \hat{S}_{m_l})\mathcal{M}^\top.$$

Moreover the electro-thermal sources for the thermal nodes and the heat flux from the distributed elements into the thermal nodes are collected in the vectors

$$\hat{\boldsymbol{P}} = \mathcal{M}\begin{pmatrix} \hat{P}_1 \\ \vdots \\ \hat{P}_{m_l} \end{pmatrix}, \qquad \hat{\boldsymbol{F}}^d = \begin{pmatrix} \hat{F}_1^d \\ \vdots \\ \hat{F}_{m_n}^d \end{pmatrix}.$$

With the vector $\hat{\boldsymbol{T}}$ containing the temperature values for all thermal nodes we end up with the final version of the lumped heat flow equation for all thermal nodes

$$\hat{\boldsymbol{M}} d_t \hat{\boldsymbol{T}} = \hat{\boldsymbol{F}}^d - \hat{\boldsymbol{S}}(\hat{\boldsymbol{T}} - T_{\mathrm{env}}\boldsymbol{I}) + \hat{\boldsymbol{P}}, \tag{2.4}$$

where $\boldsymbol{I}$ represents the unity matrix.

Distributed components and thermal branches

The branches in the thermal network correspond to the distributed elements which are modeled as thermal lines. The thermal lines are characterized by the interval $I_{\mathrm{th}} = [0, L_{\mathrm{th}}]$. The thermal line with temperature T^d is thermally described by the heat flow equation

$$M\partial_t T^d = \partial_x(\kappa \partial_x T^d) - S(T^d - T_{\mathrm{env}}) + P, \tag{2.5}$$

for $(x,t) \in (0, L_{\mathrm{th}}) \times [0, \infty)$. Thereby $M = c^d \rho^d A^d$ denotes the thermal mass, given as product of the heat capacity c^d, the material density ρ^d and the area of the cross section A^d of the considered element. κ represents the thermal conductivity and S denotes the transmission function that models the thermal radiation to the environment and is considered to be proportional to the physical surface of the modeled device. P denotes a source term, caused by electro-thermal effects and will be discussed in § 4.3 . Equation (2.5) is completed by initial and boundary conditions:

$$T^d(x,0) = T_I^d(x), \quad x \in [0, L_{\mathrm{th}}], \tag{2.6}$$

$$T^d(0,t) = T_0^d(t), \quad T^d(L_{\mathrm{th}}, t) = T_1^d(t), \quad t \in [0, \infty). \tag{2.7}$$

2.3 Coupling between thermal nodes and branches

So far we have described the lumped heat flow equation (2.4) for the thermal nodes and the heat flow equations for the thermal branches (2.5). We still

have to clarify the thermal interaction using the thermal network topology described by the thermal incidence matrix $\mathcal{A}_d^{\text{th}}$. The heat equations for the lumped and distributed elements are coupled via two effects.

- The boundary conditions (2.7) for the distributed heat equations are determined by the temperature in the thermal nodes.
- The heat flux from the distributed elements enters the thermal nodes.

The temperature of the thermal lines coincides at the boundary with the temperature of the adjacent thermal nodes. We collect all temperature values of the thermal lines in the vector $\boldsymbol{T}^d$ and denote by $\boldsymbol{T}_0^d(t)$ the vector containing the boundary values for all thermal lines at $x = 0$ and the vector $\boldsymbol{T}_1^d(t)$ containing the boundary values at $x = L_{\text{th}}$

$$\boldsymbol{T}^d(0,t) = \boldsymbol{T}_0^d(t), \qquad \boldsymbol{T}^d(L_{\text{th}},t) = \boldsymbol{T}_1^d(t).$$

With the thermal incidence matrix $\mathcal{A}_d^{\text{th}}$ and the temperature in the thermal nodes $\hat{\boldsymbol{T}}$ the boundary conditions (2.7) are given as

$$\begin{pmatrix} \boldsymbol{T}_0^d \\ \boldsymbol{T}_1^d \end{pmatrix} = \mathcal{A}_d^{\text{th}^\top} \hat{\boldsymbol{T}}. \tag{2.8}$$

The second type of coupling is realized via the thermal flux across the boundary of the thermal lines. For the thermal line the heat flux is given by Fourier's law

$$J_{\text{th}}^d(x,t) = -\kappa(x)\partial_x T^d(x,t) \tag{2.9}$$

with the thermal conductivity κ. The inflow, respectively outflow, across the boundary is then given by

$$\begin{aligned} F_0(t) &= A^d \cdot \kappa(0)\partial_x T^d(0,t), \\ F_1(t) &= -A^d \cdot \kappa(L_{\text{th}})\partial_x T^d(L_{\text{th}},t), \end{aligned}$$

where the area of the cross section of the considered element is given by A^d. Using the thermal incidence matrix $\mathcal{A}_d^{\text{th}}$, the coupling can be expressed by the flux vector

$$\hat{\boldsymbol{F}}^d = \mathcal{A}_d^{\text{th}} \begin{pmatrix} \Lambda(0)\partial_x \boldsymbol{T}(0,t) \\ -\Lambda(L_{\text{th}})\partial_x \boldsymbol{T}(L_{\text{th}},t) \end{pmatrix} \tag{2.10}$$

with

$$\Lambda = \text{diag}(A_1^d\kappa_1, \ldots, A_{m_d}^d\kappa_{m_d}),$$

where A_i^d and κ_i, for $i = 1, ..., m_d$, denote the cross section and the thermal conductivity of the i-th thermal line. $\hat{\boldsymbol{F}}^d$ then enters the lumped heat flow equation (2.4) and $\hat{\boldsymbol{F}}_i^d$ stands for the complete heat flux from the distributed elements into thermal node i.

2.4 The complete thermal network model

The complete model for a thermal network consisting of m_d thermal branches and m_n thermal nodes consists of the following equations:

Thermal network equations

$$M_i \partial_t T_i^d = \partial_x(\kappa_i \partial_x T_i^d) - S_i(T_i^d - T_{\text{env}}) + P_i, \qquad i = 1, ..., m_d. \tag{2.11}$$

$$\hat{\boldsymbol{M}} d_t \hat{\boldsymbol{T}} = \mathcal{A}_d^{\text{th}} \begin{pmatrix} \Lambda(0)\partial_x \boldsymbol{T}(0,t) \\ -\Lambda(L_{\text{th}})\partial_x \boldsymbol{T}(L_{\text{th}},t) \end{pmatrix} - \hat{\boldsymbol{S}}(\hat{\boldsymbol{T}} - T_{\text{env}}\boldsymbol{I}) + \hat{\boldsymbol{P}}, \tag{2.12}$$

$$\begin{pmatrix} \boldsymbol{T}_0^d \\ \boldsymbol{T}_1^d \end{pmatrix} = \mathcal{A}_d^{\text{th}^\top} \hat{\boldsymbol{T}}. \tag{2.13}$$

The heat flow equations for the distributed elements (2.11) result in a system of partial differential equations of parabolic type. The thermal nodes are described by the lumped version of the heat flow equation (2.12) what describes a system of ordinary differential equations unless artificial units occur. For artificial units algebraic equations (2.3) occur. Lastly the coupling between thermal nodes and thermal branches is given in terms of the boundary conditions (2.13). The dissipated power of the components results in heat source terms expressed by the terms P_i and $\hat{\boldsymbol{P}}$. They will be described in detail in § 4.3.

The system (2.11)-(2.13) results in a system of partial differential equations, if no artificial 0D-unit occurs in the network. If artificial units are introduced, the final system is of partial differential algebraic type. About the index of the system no results are known hitherto, however, due to the simplicity of the algebraic constraints we expect the index not to be higher than one.

Initial conditions The thermal network equations (2.11)-(2.13) have to be completed by initial conditions for the temperature variables

$$\hat{\boldsymbol{T}}(0) = \hat{\boldsymbol{T}}_I, \qquad T_i^d(\cdot, 0) = T_{i,I}^d \qquad \text{for } x \in (0, L_{\text{th,i}}), \quad i = 1, ..., m_d$$

We notice that the system (2.11)-(2.13) is of differential-algebraic type if the corresponding thermal network contains artificial lumped elements. In this case the initial values have to be consistent.

Chapter 3

Semiconductor device modeling

The trend of miniaturization and acceleration of computer chips leads to the development of smaller and more powerful semiconductor devices. For the development of new devices numerical simulation is indispensable as it replaces laboratory testing and thus spares the expensive production of prototypes.

Moreover, in most industrially used circuit simulators semiconductor devices are modeled by use of compact models (see § 1). However, the determination of a detailed compact model for a single device requires many numerical tests as partially several hundreds of parameters have to be extracted. As this parameter fitting is a very cumbersome and time consuming task it becomes preferable to couple distributed models for a manageable number of crucial semiconductor devices directly with the circuit equations.

As in all types of industrial application numerous simulations have to be accomplished detailed but efficient models for the semiconductor devices are required in order to reduce the numerical effort.

3.1 Hierarchy of semi-classical models

For semiconductor devices in the literature many models with a different level of detailedness are proposed. The most detailed of them are based on quantum mechanical considerations and model the movement of single electrons in the device. Those models are based on the Schrödinger equation whose solution requires high numerical effort.

Another approach leads to the semi-classical transport models, where the electrons in the device are considered as continuum. The most detailed one in the hierarchy of those models is the semi-classical Boltzmann equation, where the quantum effects of the semiconductor crystal are taken into account coarsely via special parameters. However, the semi-classical Boltz-

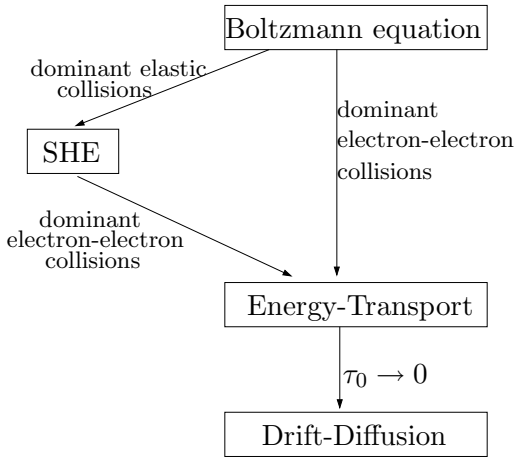

Figure 3.1: Hierarchy of semi-classical semiconductor models. τ_0 denotes the energy relaxation time

mann equation is a nonlinear integro-differential system and is numerically treatable with high effort, only (e.g. Monte Carlo simulation). This makes it preferable to use macroscopic models that are derived as approximation to the Boltzmann equation.

The drift-diffusion model is the least complex and best understood one in this hierarchy. It consists of mass conservation equation and the constitutive current relation, only. It has been derived under phenomenological considerations by van Roosbroeck in [**81**]. A rigorous derivation has been performed by Poupaud in [**80**]. For detailed semiconductor device and circuit simulation, however, the drift-diffusion model is not detailed enough as it completely neglects thermal effects.

Bløtekjær in [**21**] and Baccarani and Wordemann in [**12**] derived the hydrodynamic model as approximations to the Boltzmann equation by means of the method of moments. However, the model contains hyperbolic modes and therefore enforces special numerical treatment.

In [**92**] Stratton derived the first energy-transport model. It is more complex than the drift-diffusion model as it allows for thermal effects by considering the electron temperature as additional variable. As it keeps the parabolic structure of the drift-diffusion model its intermediate complexity and numerical effort makes it appropriate for detailed semiconductor device simulation. Moreover, the energy-transport model we consider can be written in a drift-diffusion-formulation [**34**]. Therefore, algorithms and discretization schemes developed for the drift-diffusion model can be employed or extended to the energy-transport model.

In [**19**] the energy-transport model is derived from the semi-classical Boltzmann equation via an intermediate model by means of the Hilbert

expansion method. Under the assumption of dominant elastic scattering the diffusion limit leads to the so-called SHE (Spherical Harmonic Expansion) model. Assuming dominant particle-particle scattering compared to particle-phonon scattering Hilbert expansion leads to the energy-transport model.

The direct limit from Boltzmann equation to an energy-transport model was performed in [**18**]. Extra numerical effort is necessary to get all coefficients in this model. More recently in [**35**] the same model as in [**19**] has been derived directly from the semi-classical Boltzmann equation via a different scaling limit. Under a simple relaxation time limit ($\tau_0 \to 0$) for the energy relaxation time τ_0 (see below) we derive the drift-diffusion model from the energy-transport model. Figure 3.1 shows the hierarchy of the mentioned transport models. Depending on conditions on the microscopic relaxation times, various energy-transport models can be derived [**34**].

In this work we consider the energy-transport model proposed in [**27**] for the majority charge carriers, the electrons. All devices considered in this work are assumed to be majority carrier devices, what implies that the terminal current mainly is determined by the current induced by the majority charge carriers. The minority charge carriers, the holes, are modeled by the less detailed drift-diffusion model. In § 3.4 we will make an exception and consider the complete thermal model for the bipolar energy-transport model.

3.2 Energy-transport and drift-diffusion equations

In this work we consider the energy-transport model under the following simplifying assumptions:

- We use the parabolic band approximation

$$E(k) = \frac{\hbar^2}{2m^*}|k|^2,$$

  with the effective mass m^*, the reduced Planck constant $\hbar$ and the pseudo wave vector k.

- We assume non-degenerate semiconductors. This implies, that the particle distribution f is given by the Maxwell-Boltzmann statistics.

- The elastic collision operator is given as a relaxation time operator, (see (3.10)).

In [**34**] it is shown that under these assumptions the model can be written in a drift-diffusion formulation. This has the advantage that discretization techniques and iteration schemes developed for the well understood drift-diffusion model can be applied or extended to the energy-transport model.

More precisely, it will allow for a discretization that guarantees positivity of the discrete carrier densities (see § 6.2).

In the following the semiconductor device is described by the domain Ω_S. The device boundary is assumed to split into two parts, the union of ohmic contacts Γ_C and the union of insulating boundary segments Γ_I, where $\partial\Omega_S = \Gamma_C \cup \Gamma_I$.

The physical model described in [**34**] consists of the conservation laws for the electron density n and the energy density $w = \frac{3}{2}k_B n T_n$ with electron temperature T_n and Boltzmann constant k_B

$$\partial_t n - \frac{1}{q}\operatorname{div} J_n = -R(n,p,) \tag{3.1}$$

$$\partial_t w - \operatorname{div} J_w = -\nabla V \cdot J_n + W(n,T) - \frac{3}{2}k_B T_n R(n,p), \tag{3.2}$$

together with the constitutive relations for the electron and energy current density J_n and J_w

$$J_n = q\left[\nabla\left(\mu_\beta^{(1)}(T_n)\frac{k_B T_n}{q}n\right) - \mu_\beta^{(1)}(T_n)n\nabla V\right], \tag{3.3}$$

$$J_w = \left[\nabla\left(\mu_\beta^{(2)}(T_n)\frac{(k_B T_n)^2}{q}n\right) - \mu_\beta^{(2)}(T_n)nk_B T_n\nabla V\right], \tag{3.4}$$

where $\mu_\beta^{(i)}(T_n)$ denote the electron and energy mobility relation, which depend on hot carrier effects. Moreover the index β refers to the dependence on inelastic scattering (see (3.11)). The equations are coupled to the Poisson equation for the electric potential V

$$\varepsilon_s \Delta V = q(n - p - C(x)), \tag{3.5}$$

where q is the elementary charge and ε_s the permittivity constant. The space dependent function $C(x)$ models fixed charged background ions in the semiconductor crystal, the doping profile.

The distribution of the hole density p is modeled by the drift-diffusion equations

$$\partial_t p + \frac{1}{q}\operatorname{div} J_p = -R(n,p), \tag{3.6}$$

$$J_p = -q\left[\nabla\left(\mu_p(T_L)\frac{k_B T_L}{q}p\right) + \mu_p(T_L)p\nabla V\right], \tag{3.7}$$

where T_L denotes the lattice temperature of the device and $\mu_p(T_L)$ the low field mobility of holes that depends on the lattice temperature (see below).

The function

$$R(n,p) = R_{\mathrm{SRH}}(n,p) + R_{\mathrm{Au}}(n,p)$$

models the generation-recombination effects in the device.

The two terms denote the Shockley-Read-Hall and Auger recombination terms given by

$$R_{\mathrm{SRH}}(n,p) = \frac{np - n_i^2}{\tau_p(n+n_i) + \tau_n(p+n_i)}, \tag{3.8}$$

$$R_{\mathrm{Au}}(n,p) = (C_n n + C_p p)(np - n_i^2), \tag{3.9}$$

with the intrinsic density n_i and the material dependent electron and hole lifetimes τ_n and τ_p. The Auger recombination parameters are denoted by C_n and C_p. For high carrier densities the consideration of Auger processes is crucial as it exceeds the SRH-recombination. In optoelectronic devices further generation processes occur. This will be discussed in § 3.3.

The relaxation to the equilibrium energy is given by the Fokker-Planck approximation

$$W(n,T) = \frac{3}{2}\frac{nk_B(T_L - T_n)}{\tau_\beta(T_n)}. \tag{3.10}$$

The expression τ_β stands for the relaxation time where the index β, as in $\mu_\beta^{(i)}$, refers to the dependence on inelastic scattering. These material dependent parameters will be expressed in terms of the low field mobility μ_n and the typical relaxation time τ_0. We employ the relations for $\beta = \frac{1}{2}$, what results in (see [**34**])

$$\mu_{\frac{1}{2}}^{(1)}(T) = \mu_n \frac{T_L}{T}, \qquad \mu_{\frac{1}{2}}^{(2)}(T) = \frac{3}{2}\mu_n \frac{T_L}{T}, \qquad \tau_{\frac{1}{2}}(T) = \tau_0. \tag{3.11}$$

The resulting model coincides with the model proposed by Chen et. al. in [**27**] and therefore is referenced to as *Chen-model*. Moreover in [**43**] the same relation for the carrier mobility as in (3.11) has been presented.

Low field mobility

The values for μ_n, μ_p and τ_0 can be determined from measurement and for our examples we will use values from literature [**65**]. For the exact determination of these values from microscopic quantities like effective mass and scattering effects, as well as for the models for different values of β, we refer to [**34**]. The low field mobilities strongly depend on the lattice temperature, what is modeled by the power law (see [**43, 87**])

$$\mu_\nu(T_L) = \mu_{\nu,0}\left(\frac{T_0}{T_L}\right)^{\alpha_\nu}, \quad \nu = n,p, \tag{3.12}$$

with the temperature $T_0 = 300\,\mathrm{K}$. A detailed list of measured values for the parameters α_ν and $\mu_{\nu,0}$ can be found in [**87**, Table 4.1-1]. For silicon the values are in the range of $2.2 \leq \alpha_\nu \leq 2.7$.

In addition, for high doping concentration (in silicon for about $10^{22}\mathrm{m}^{-3}$), the low field mobility for electrons and holes are influenced by impurity scattering. In [68] this is modeled via

$$\mu_{\nu,0} = \mu_{\nu,\min} + \frac{\mu_{\nu,\max} - \mu_{\nu,\min}}{1 + (C/C_{\mathrm{ref}})},$$

where the corresponding parameters for silicon are given.

In our simulations, we will incorporate the temperature dependence of the low field mobilities (3.12), the dependence on the doping level will be neglected.

3.2.1 Boundary and initial conditions

For the model equations we impose appropriate initial and boundary conditions. We prescribe the initial conditions for the energy-transport equations for the particle densities and the temperature

$$n(\cdot,0) = n_I, \quad p(\cdot,0) = p_I, \quad T_n(\cdot,0) = T_I \quad \text{in } \Omega_S. \tag{3.13}$$

We recall that the device boundary is given as the union of ohmic contacts and the insulating boundary segments by $\partial\Omega_S = \Gamma_C \cup \Gamma_I$. Although we will present later one-dimensional simulations, we give the boundary conditions for the multidimensional situation. On the insulating parts, it is assumed that the normal components of the current densities, of the electric field and the temperature flux vanish. With the outer normal ν we state the boundary conditions

$$J_n \cdot \nu = J_p \cdot \nu = J_w \cdot \nu = \nabla V \cdot \nu = \nabla T_n \cdot \nu = 0 \quad \text{on } \Gamma_I,\ t > 0. \tag{3.14}$$

The semiconductor contacts connecting the device to the surrounding network are assumed to be ohmic semiconductor-metal contacts. At these contacts, the electric potential equals the sum of the applied voltage V_{ap} and the so-called built-in potential V_{bi} (see [73]),

$$V = V_{\mathrm{ap}} + V_{\mathrm{bi}} \quad \text{on } \Gamma_C,\ t > 0, \qquad \text{with} \qquad V_{\mathrm{bi}} = \operatorname{arcsinh}\Big(\frac{C}{2n_i}\Big), \tag{3.15}$$

where C denotes the doping profile and n_i the intrinsic carrier density.

Dirichlet boundary conditions at the contacts

In [34, 52, 53] Dirichlet conditions are assigned to the electron temperature T_n at the contacts

$$T_n = T_a \quad \text{on } \Gamma_C,\ t > 0, \tag{3.16}$$

with the ambient temperature T_a (usually 300 K). Moreover for ideal ohmic contacts the particle densities are often assigned to fulfill Dirichlet boundary conditions

$$n = n_a, \quad p = p_a \qquad \text{on } \Gamma_C,\ t > 0, \tag{3.17}$$

as in [**85**], where the values for n_a and p_a can be derived under the assumption of charge neutrality, $n_a - p_a - C(x) = 0$, and thermal equilibrium, $n_a p_a = n_i^2$. Solving these equations for n_a and p_a gives

$$n_a = \frac{1}{2}\Big(C + \sqrt{C^2 + 4n_i^2}\Big), \quad p_a = \frac{1}{2}\Big(-C + \sqrt{C^2 + 4n_i^2}\Big). \tag{3.18}$$

The boundary conditions for the energy w then can be easily computed out of (3.16) and (3.17) and result in

$$w = w_a \quad \text{on } \Gamma_C,\ t > 0, \tag{3.19}$$

with $w_a = \frac{3}{2} k_B n_a T_a$.

Boundary conditions of Robin type at the contacts

In [**10**] the application of homogeneous Neumann boundary conditions to the temperature T_n

$$\nabla T_n \cdot \nu = 0 \quad \text{on } \Gamma_C,\ t > 0, \tag{3.20}$$

is suggested, motivated by comparison with the solution of the Boltzmann-equation. Furthermore, in [**103**] Yamnahakki derived second order boundary conditions for the drift-diffusion model for semiconductors which result in boundary conditions of Robin type

$$n + (\theta_n \mu_n)^{-1} J_n \cdot \nu = n_a \quad \text{and} \quad p - (\theta_p \mu_p)^{-1} J_p \cdot \nu = p_a \quad \text{on } \Gamma_C,\ t > 0, \tag{3.21}$$

with parameters θ_n and θ_p. We apply this type of conditions with the ambient particle densities n_a and p_a given in (3.18). The boundary conditions for the energy density w then are derived from (3.20) and (3.21). Under a constant approximation of T_L they result in

$$\nabla w \cdot \nu - (k_B T_L)^{-1} \theta_n (w_a - w) = \frac{3}{2} T_0^{-1} \theta_n n_a (T_n - T_a) + \frac{3}{2} q n \nabla V \cdot \nu \quad \text{on } \Gamma_C,\ t > 0, \tag{3.22}$$

with the ambient temperature T_a and the ambient energy density w_a.

In § 8.1 we will give a numerical comparison of the different types of boundary conditions. We will see that the choice of Dirichlet boundary conditions results in strong boundary layers for bipolar devices like *pn* and *p-i-n* diodes under large forward bias. These boundary layers indicate that the choice of Dirichlet values is not a physical appropriate one.

3.2.2 Thermal equilibrium

A distinguished state in semiconductor devices is the state of thermal equilibrium. The stationary state of thermal equilibrium corresponds to a state of zero current flow $J_n = J_p = 0$. Moreover in thermal equilibrium the electron temperature and lattice temperature coincide with the ambient temperature $T_L = T_n = T_0 = 300\,\mathrm{K}$. Thus, the energy-transport model reduces to the drift-diffusion model. In addition, no recombination effects occur what implies $np = n_i^2$. According to [**73**] the particle densities in Ω_S are given by

$$n_{\mathrm{eq}} = n_i e^{(qV_{\mathrm{eq}})/k_B T_0}, \qquad p_{\mathrm{eq}} = n_i e^{-(qV_{\mathrm{eq}})/k_B T_0},$$

where V_{eq} is the equilibrium potential determined by

$$\begin{aligned} \varepsilon_s \Delta V_{\mathrm{eq}} &= q(n_{\mathrm{eq}} - p_{\mathrm{eq}} - C) = q\big(n_i[e^{(qV_{\mathrm{eq}})/k_B T_0} - e^{-(qV_{\mathrm{eq}})/k_B T_0}] - C\big) \\ &= q(2n_i \sinh \frac{qV_{\mathrm{eq}}}{k_B T_0} - C) \qquad \text{in } \Omega_S. \end{aligned} \tag{3.23}$$

The corresponding boundary conditions read

$$\begin{aligned} V_{\mathrm{eq}} &= \frac{k_B T_0}{q} \operatorname{arcsinh}\big(\frac{C}{2n_i}\big) && \text{on } \Gamma_C, \\ \nabla V_{\mathrm{eq}} \cdot \nu &= 0 && \text{on } \Gamma_I, \end{aligned}$$

and are chosen in such way that the right hand side of (3.23) vanishes in order to avoid boundary layers for the potential. For a more detailed description of the thermal equilibrium we refer to [**73, 51**].

3.3 Optoelectronic device modeling

Semiconductor lasers are important devices in optoelectronic integrated circuits for high-speed communication systems. First phenomenological approaches to model laser diodes consisted in a direct relation between the driving current and the output power [**29**]. Increasingly complex device structures made it necessary to include semiconductor device equations for better accuracy. In [**13**] and [**78**], for instance, the drift-diffusion equations are employed to model the charge transport in the device, coupled with an appropriate model for the optical effects.

Thermal effects play an important role in laser diodes and have to be included in the mathematical models. By considering an equivalent thermal circuit, a linear second-order equation for the laser temperature has been derived in [**7**]. Temperature-dependent models are also included in the commercial laser diode simulators LASTIP and PICS3D which are based on the drift-diffusion model [**32**]. A heat flow equation for the lattice temperature was recently derived in [**14**] from a thermodynamics-based model.

In the following we describe some models for optical effects in photonic devices used in the literature. The optical effects in the laser diode can be modeled by a rate equation for the number of photons. In [2] (§6.2) and [102], the intensity of the optical field confined to the active region is approximated by the so-called confinement factor. However, this does not allow for a local coupling between the electrical and optical effects. The model can be improved by replacing the confinement factor by the local intensity distribution computed from the waveguide equation [13]. Further improvements are obtained by considering several rate equations for each laser mode and by including quantum effects [13]. Another possibility to increase the accuracy of the models is to decompose the optical field inside the laser into forward and backward propagating waves whose amplitudes are calculated from the travelling wave equation [15, 60]. Also in this approach, thermal effects may be included [66].

Photo diodes can be described by equivalent circuit models [94] or drift-diffusion equations [59], where the optical effects are taken into account by a generation term [31, 55]. Since the drift-diffusion equations cannot capture thermal effects in the device, we employ the energy-transport equations for the electron transport.

3.3.1 Laser diode

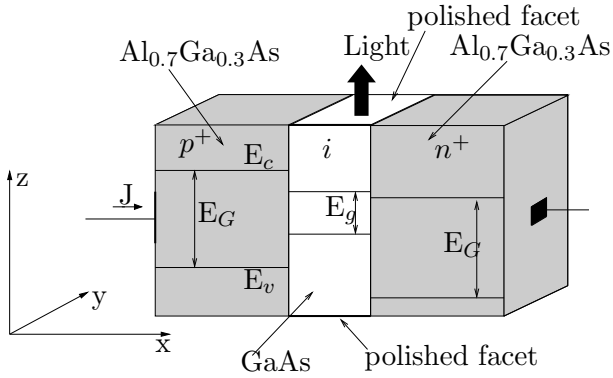

Figure 3.2: Simplified structure of a laser diode including a schematic illustration of the energy bands before assembling the different materials. Here, E_c denotes the conduction band energy, E_v the valence band energy, and E_G and E_g the energy gaps of the corresponding materials.

As a simplified model of a laser diode we consider a heterostructure *p-i-n* diode as displayed in Figure 3.2. It consists of an intrinsic or lowly doped part of a low band-gap semiconductor material like GaAs sandwiched by highly doped cladding layers made from a semiconductor material with a higher band-gap like $Al_{0.7}Ga_{0.3}As$. The different band gaps of the het-

erostructure result in a bending of the energy bands (see [**78**], §3.3, and [**31**]). Due to the lower band gap the charge carriers tend to move to the intrinsic region as this corresponds to a state of lower energy, causing carrier confinement. For a forward biased device the number of free charge carriers increases and spontaneous and stimulated emission of photons occur due to recombination effects. Thus, an optical field represented by photons arises in the intrinsic region and, as the facets of the device are polished, the intrinsic region works as a laser cavity or a simple Fabry-Perot laser [**13**].

In the device, we assume that the electron flow is described by the energy-transport equations (3.1)-(3.4). There the electric potential is replaced by the effective potential

$$V_n = V + U_n,$$

given as the sum of the electric potential V, described by the Poisson equation (3.5), and the band potential U_n. The band potential is a simple model of the carrier confinement caused by the difference of the material band gaps. It is positive inside the active region and zero outside. The hole flow is described by the drift-diffusion equations (3.6)-(3.7), where the effective potential for holes is given by

$$V_p = V + U_p.$$

The band potential for holes U_p is negative within the active region and zero outside.

Recombination-generation terms

The coupling between optical and electrical effects in the device is taken into account in terms of recombination-generation processes

$$R = R_{\mathrm{SRH}} + R_{\mathrm{Au}} + R_{\mathrm{spon}} + R_{\mathrm{stim}}, \tag{3.24}$$

where the first two terms denote the Shockley-Read-Hall and Auger recombination terms given in (3.8) and (3.9).

The last two recombination terms in (3.24) model recombination processes that account for the generation of photons, the spontaneous and stimulated emission [**2, 31**]

$$R_{\mathrm{spon}}(n,p) = Bnp, \quad R_{\mathrm{stim}}(n) = \sum_m v_g g_m(n) |\Xi_m|^2 S_m, \tag{3.25}$$

respectively, where $B = \sum_m B_m$ is the material-dependent spontaneous recombination parameter, given as the sum of the parameters of all laser modes m. In the stimulated emission term, $v_g = c/\mu_{\mathrm{opt}}$ denotes the group velocity of the photons with the speed of light c and the refractive index of the material μ_{opt}. Furthermore, $g_m(n)$ denotes the optical gain, which is

the amplification factor for the number of photons per unit length, $|\Xi_m|^2$ is the intensity distribution of the optical field, and S_m is the number of photons in the device. For a one-dimensional and two-dimensional modeling of the device, the number of photons has to be replaced by the number of photons in the considered cross-section of the cavity, i.e. $S_m/L_c d_c$ in the one-dimensional and S_m/L_c in the two-dimensional situation, where L_c denotes the length and d_c the width of the laser cavity.

In the following we discuss the modeling of the optical gain and the intensity distribution. The optical gain $g_m(n)$ is approximated by the common approach [**2**]

$$g_m(n) = g_{0,m}(n - n_{\text{th}}), \tag{3.26}$$

where $g_{0,m}$ is the differential gain of the m-th mode and n_{th} is the threshold density. Assuming an undoped intrinsic region, we may assume local charge neutrality $n = p$ such that we can write $g_m(p) = g_{0,m}(p - n_{\text{th}})$ in the stimulated recombination term occurring in the hole transport equations (3.6). This allows for a discretization of the drift-diffusion equations guaranteeing positivity of the discretized hole density (see Remark 6.2).

The optical field intensity $|\Xi_m|^2$ for the transverse modes is computed from the solution of the waveguide equation

$$\Big(\Delta + \frac{\omega^2}{c^2}\varepsilon_{\text{opt}}(n)\Big)\Xi_m = \beta_m^2 \Xi_m, \tag{3.27}$$

where β_m^2 is the corresponding eigenvalue, ω denotes the angular frequency of the emitted light, and $\varepsilon_{\text{opt}}(n)$ the complex-valued dielectric function of the pumped laser averaged over one section in a longitudinal direction. It is given by $\varepsilon_{\text{opt}}(n) = (\mu_{\text{opt}} + ic(g_m(n) - \alpha_{\text{bg}})/2\omega)^2$ (see [**13**]). Here, $i^2 = -1$ and α_{bg} is the background absorption. The solutions of (3.27) describe the transverse modes for which the corresponding number of photons S_m is balanced by the rate equation

$$d_t S_m = v_g(2\text{Im}(\beta_m) - \alpha_f)S_m + R_{\text{spon},m}, \tag{3.28}$$

where the spontaneous emission rate into the mode m is given as

$$R_{\text{spon},m} = \int_{\Omega_c} B_m np \, ds,$$

with the transverse cross-section of the laser cavity Ω_c and the total facet loss by external output α_f. The modal gain $\text{Im}(\beta_m)$ is the imaginary part of the eigenvalue corresponding to the solution of (3.27).

Finally, the output power of the mode m is computed according to [**14**] by

$$P_{\text{out},m} = \hbar\omega v_g \alpha_f |\Xi_m|^2 S_m, \tag{3.29}$$

where $\hbar = h/2\pi$ is the reduced Planck constant.

Model simplifications

We make three simplifying assumptions. The first assumption is that the optical field is dominated by the fundamental mode so that we restrict ourselves to a single-mode laser. Thus, we only need to consider a single rate equation (3.28) and the sum in (3.25) reduces to a single term. In the following, we omit the index m.

Furthermore, the intensity distribution of the fundamental mode can be computed from the effective index approximation [**2**]. Here, the dielectric function is simplified by $\varepsilon_{\mathrm{opt}}(n) = \mu_{\mathrm{opt}}^2$ such that the waveguide equation can be solved explicitly in each material, assuming that the total solution is smooth and vanishes far from the active region. We will present below a comparison of the solutions obtained from the complete model including the waveguide equation and from the simplified model.

Finally, if the simplified model is considered, we approximate the modal gain $\mathrm{Im}(\beta)$, needed in the rate equation (3.28), by

$$2\mathrm{Im}(\beta) \approx \int_{\Omega_c} (g(n) - \alpha_{\mathrm{bg}})|\Xi|^2 ds. \tag{3.30}$$

The approximation (3.30) can be derived from a first-order perturbation analysis (see [**2**] or [**75**], Chapter 9) and has been also mentioned in [**14**].

These simplifications result in a model which is similar to the treatment of the optical field by the number of photons and the so-called confinement factor [**2, 31**]. However, our model allows for a local coupling of the electrical and optical effects with only slightly higher computational effort.

Boundary and initial conditions

The initial and boundary conditions for the transient transport equations and the Poisson equation are described in § 3.2.1.

Additionally, the initial number of photons is prescribed by $S(0) = S_I$ in Ω_S. For the waveguide equation (3.27), we impose the boundary condition $\Xi = 0$ on $\partial\Omega_S$. This coincides with the assumption that the intensity of the optical field decreases to zero at the boundary, what seems reasonable as the optical field is confined to the active region.

3.3.2 Photo diode

We consider a p-i-n-homostructure (a heterostructure could also be used) as a simplified model of a vertical photo diode with optical irradiation at the p-doped contact as shown in Figure 3.3. The supplied light (photons) generates free charge carriers which cause the photo current.

The transport of charge carriers is modeled by the energy-transport equations (3.1)-(3.4) for electrons, the Poisson equation (3.5) for the electric

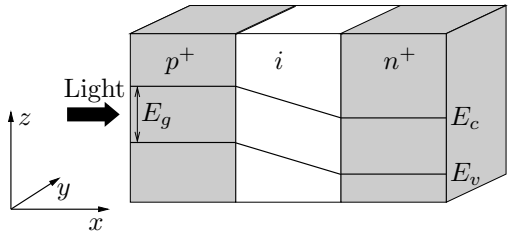

Figure 3.3: Simplified structure of a silicon photo diode including a schematic illustration of the energy bands.

potential V, and the drift-diffusion equations (3.6)-(3.7) for holes. The recombination term for the photo diode is given by

$$R = R_{\mathrm{SRH}} + R_{\mathrm{Au}} - G_{\mathrm{opt}}, \tag{3.31}$$

where

$$G_{\mathrm{opt}}(x) = \eta(1-r)\frac{P_{\mathrm{in}}}{\hbar\omega A}\alpha_{\mathrm{ab}} e^{-\alpha_{\mathrm{ab}}x} \tag{3.32}$$

denotes the generation rate of free charge carriers at depth x of the device caused by the optical irradiation power P_{in} with angular frequency ω (see [**31**, **55**, **59**]). The reflectivity of the surface of the diode is given by r, the optical absorption of the material by α_{ab}, the quantum efficiency (the fraction of photons that generates charge carriers) by η, and the area of the surface hit by the irradiation by A. Furthermore, $P_{\mathrm{in}}/\hbar\omega$ is the injected number of photons per second. The boundary and initial conditions are the same as in the previous section.

3.4 Heating of the crystal lattice

Employing the energy-transport model allows for the consideration of the carrier temperature and thus for thermal effects in the device. However, with increasing complexity of devices driven by higher frequencies, the heating of devices (i.e. the crystal lattice) becomes more and more significant. As additionally many electrical parameters in the hitherto presented models depend on the lattice temperature, isothermal modeling of the crystal lattice is no longer appropriate.

To extend the described model, besides the electron and hole subsystems we now additionally consider the crystal lattice of the device. These three subsystems, with optionally three different temperatures are thermally coupled by mutual energy and heat flux exchange. This is schematically shown in

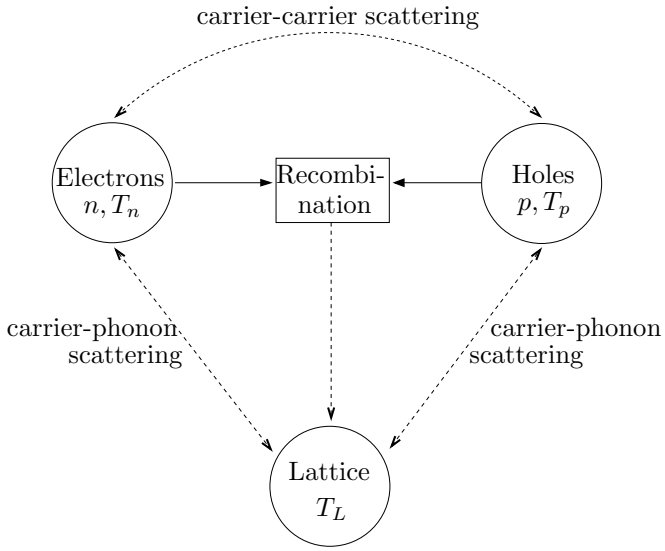

Figure 3.4: Schematic description of thermal interaction between electron, hole and lattice subsystem.

Figure 3.4. In the common approach the lattice subsystem is described by the heat flow equation for the lattice temperature T_L

$$\rho_L c_L \partial_t T_L - \operatorname{div}(\kappa_L \nabla T_L) = H, \tag{3.33}$$

where ρ_L is the material density, c_L stands for the heat capacity and κ_L for the heat conductivity of the material. For the heat source H different terms, depending on the employed models for the transport of charge carriers, have been suggested.

Non-isothermal device modeling started in the 70's, when the carrier subsystems have been modeled by the drift-diffusion equations. Thus only the lattice temperature was considered. In [**42**] Gaur and Navon suggested

$$H = J \cdot E, \tag{3.34}$$

the product of current J and the electric field E as source term, what solely takes into account the Joule heating. The same term was suggested by Sharma and Ramanathan in [**89**]. More accurate source terms, taking into account recombination heat as well, have been presented in [**1, 30, 87**]. In [**1**] Adler suggested the source term

$$H = \operatorname{div}\left(\frac{E_c}{q} J_n + \frac{E_v}{q} J_p\right),$$

with the conduction and valence band E_c and E_v, respectively. This term includes recombination effects as well as band gap narrowing. For non-degenerate semiconductors the Adler-model simplifies to

$$H = (J_n + J_p) \cdot E + R E_g. \tag{3.35}$$

In [**38**] a source term is suggested that even considers the time dependency of the electric field as heat source (i.e. the displacement current).

One of the most central works on the thermal coupling between carrier and lattice subsystems has been presented by Wachutka in 1990 [**100**]. He did the first rigorous thermodynamic treatment of the heat generation in semiconductors. In his final model besides Joule and recombination heat also the Thomson-, Peltier- and Seebeck effects turn up in the source term for the heat flow equation. The same source term has been derived in [**3**] from a general expression for the free energy under consideration of Onsager's reciprocal laws and the entropy maximum principle.

However, despite the complexity of this model, it does not take into account several temperatures and the temperature of the charge carriers are assumed to coincide with T_L.

Models including different lattice and charge carrier temperatures have been developed in the 90's. In [**58, 43**] the unipolar hydrodynamic model has been coupled to (3.33), where as source term for the heat flow equation the Fokker-Planck relaxation term (3.10) has been considered.

In [**101**] Wachutka presented a source term for the heat flow equation coupled to a bipolar energy-transport model for the carrier subsystems:

$$\begin{aligned} H = &- q\left[T_p\left(\frac{\partial\phi_p}{\partial T_p}\right) - T_n\left(\frac{\partial\phi_n}{\partial T_n}\right) + \phi_n - \phi_p\right]\cdot R \\ &+ \frac{3}{2}k_B n\frac{T_n - T_L}{\tau_0} + \frac{3}{2}k_B p\frac{T_p - T_L}{\tau_{0,p}} \end{aligned} \tag{3.36}$$

where ϕ_n and ϕ_p denote the quasi fermi-potentials for electrons and holes, respectively. The first term in (3.36) describes the energy transferred to the lattice subsystem due to recombination effects and the last two terms describe the temperature relaxation between carrier and lattice temperature (comp. (3.10)).

In the following we will derive a similar energy conserving heat source term for the heat flow equation coupled to our energy-transport model for bipolar modeling. As the heat source term for the drift-diffusion case has already been examined intensely, we will derive the heat flow equation for hole and electron subsystems modeled by the energy-transport model. This can then be easily adapted to the mixed energy-transport (for electrons) and drift-diffusion (holes) model suggested in § 3.2. The difference between the energy-transport and drift-diffusion case will be discussed.

To derive the heat source term for (3.33) we follow the approach presented recently in [**14**]. There, from a general expression for the free energy a source term for (3.33) coupled to the drift-diffusion model for optoelectronic devices has been derived under thermodynamic considerations and consideration of the entropy maximum principle.

We will adapt the free energy to the case of several temperatures and under a more phenomenological definition of the energy currents we will

achieve a heat flow equation coupled to our energy-transport model that guarantees energy conservation

$$\partial_t u + \operatorname{div} J_u = 0, \tag{3.37}$$

for the total energy u with the corresponding energy flux density J_u. The radiation that is emitted from the device is neglected for the moment. It will be taken into account in the final version of the heat flow equation.

3.4.1 Heat equation for the bipolar energy-transport model

The energy-transport model for the carrier densities n and p with the corresponding carrier temperatures T_n and T_p and energy densities $w = \frac{3}{2}k_B n T_n$ and $w_p = \frac{3}{2}k_B p T_p$ reads

$$\begin{aligned}
\varepsilon_s \Delta V =& q(n - p - C(x)),\\
\partial_t n - q^{-1}\operatorname{div} J_n = -R, \qquad & \partial_t w - \operatorname{div} J_w = -J_n \nabla V + W - \frac{3}{2}k_B T_n R,\\
\partial_t p + q^{-1}\operatorname{div} J_p = -R, \qquad & \partial_t w_p + \operatorname{div} J_{w_p} = -J_p \nabla V + W_p - \frac{3}{2}k_B T_p R,
\end{aligned}$$

with the energy relaxation terms

$$W = \frac{3}{2}k_B n \frac{T_L - T_n}{\tau_0} \qquad W_p = \frac{3}{2}k_B p \frac{T_L - T_p}{\tau_{0,p}}.$$

The current density relations for the electron subsystem are given in (3.3) and (3.4). The corresponding relations for the hole subsystem can be derived analogously.

Analogous to [**14**] we define the free energy for the system of Poisson and energy-transport equations as

$$\begin{aligned}
f = \frac{\varepsilon_s}{2}|\nabla V|^2 + \rho_L c_L T_L(1 - \log T_L) + n\left[k_B T_n\left(\log\frac{n}{N_c} - 1\right) + E_c\right]\\
+ p\left[k_B T_p\left(\log\frac{p}{N_v} - 1\right) - E_v\right]
\end{aligned} \tag{3.38}$$

with material density and heat capacity of the crystal lattice ρ_L, c_L and band edges E_c, E_v for the conduction and valence band, respectively. The effective densities of states are given by

$$N_c = 2\left(\frac{m_e^* k_B T_n}{2\pi\hbar}\right)^{\frac{3}{2}}, \qquad N_v = 2\left(\frac{m_h^* k_B T_p}{2\pi\hbar}\right)^{\frac{3}{2}},$$

with effective mass of the electrons and holes m_e^*, m_h^*, the Boltzmann constant k_B and the reduced Planck constant $\hbar$. The first term in (3.38) denotes

the energy of the electric field, the second term the energy of the lattice subsystem and the last two terms stand for the energy of the electron and hole subsystem, respectively. The particle energy thereby separates into the thermal energy and the energy of the particles due to their presence in the higher energetic conduction and lower energetic valence band, respectively.

With this we get the total internal energy of the system as

$$\begin{aligned} u &= f - T_n \frac{\partial f}{\partial T_n} - T_p \frac{\partial f}{\partial T_p} - T_L \frac{\partial f}{\partial T_L} \qquad (3.39)\\ &= \underbrace{\frac{\varepsilon_s}{2}|\nabla V|^2}_{u_E} + \underbrace{\rho_L c_L T_L}_{u_L} + \underbrace{n(E_c - T_L E_c')}_{u_n} + \underbrace{\frac{3}{2} k_B n T_n}_{u_w = w} + \underbrace{p(T_L E_v' - E_v)}_{u_p} + \underbrace{\frac{3}{2} k_B p T_p}_{u_{w_p} = w_p} \end{aligned}$$

where the prime in E_c' and E_v' denotes the derivative with respect to T_L. The total internal energy is the sum of the energy of the electric field u_E, the energy of the crystal lattice u_L, the thermal energy of the electrons w and holes w_p and the energy of the electrons in the conduction band u_n and the holes in the valence band u_p. Under the assumption of $T_L = T_n = T_p$ the expressions for the free and internal energy coincide with the expressions suggested in [**14**] for the drift-diffusion case.

To pose energy conservation we have to consider the corresponding energy flux densities:

$$u_E = \frac{\varepsilon_s}{2}|\nabla V|^2, \qquad J_u^E = -V\varepsilon_s \nabla \partial_t V, \qquad (3.40)$$

$$u_L = \rho_L c_L T_L, \qquad J_u^L = -\kappa_L \nabla T_L, \qquad (3.41)$$

$$u_n = n(E_c - T_L E_c'), \qquad J_u^n = -\left[E_c - T_L E_c'\right] q^{-1} J_n + V J_n, \qquad (3.42)$$

$$u_w = \frac{3}{2} k_B n T_n, \qquad J_u^w = -J_w, \qquad (3.43)$$

$$u_p = p(T_L E_v' - E_v), \qquad J_u^p = \left[T_L E_v' - E_v\right] q^{-1} J_p + V J_p, \qquad (3.44)$$

$$u_{w_p} = \frac{3}{2} k_B p T_p, \qquad J_u^{w_p} = J_{w_p}. \qquad (3.45)$$

The flux of the thermal energy for electrons is given by J_w in (3.4) and J_n denotes the electron current defined in (3.3). The minus signs in (3.42) and (3.43) result from the definition of J_w and J_n. The expressions for the hole density and thermal hole energy are defined analogously.

Observe that the second terms in the definition of J_u^n and J_u^p together with J_u^E denote the well accepted expression for the current of the dissipated power that is given as the product of total current and applied potential. The term $-\varepsilon_s \nabla \partial_t V$ in (3.40) namely denotes the so-called displacement current, that has to be considered in transient simulations in order to guarantee charge conservation (see § 4.1).

Using the energies and corresponding fluxes defined in (3.40)-(3.45), en-

ergy conservation (3.37) leads to

$$\begin{aligned}0 =&\partial_t(\frac{\varepsilon_s}{2}|\nabla V|^2) - \operatorname{div}(V\varepsilon_s\nabla\partial_t V) + \rho_L c_L \partial_t T_L - \operatorname{div}(\kappa_L \nabla T_L)\\ &+ \partial_t(n[E_c - T_L E_c']) - q^{-1}[E_c - T_L E_c']\ \operatorname{div} J_n - q^{-1} J_n \cdot \nabla[E_c - T_L E_c']\\ &- \partial_t(p[E_v - T_L E_v']) - q^{-1}[E_v - T_L E_v']\ \operatorname{div} J_p - q^{-1} J_p \cdot \nabla[E_v - T_L E_v']\\ &+ \operatorname{div}(V J_n) + \operatorname{div}(V J_p) + \partial_t w - \operatorname{div} J_w + \partial_t w_p + \operatorname{div} J_{w_p}.\end{aligned}$$

As the energy bands do not directly depend on time we get after partial differentiation

$$\begin{aligned}0 =&\varepsilon_s \nabla V \nabla\partial_t V - V\varepsilon_s \Delta\partial_t V - \varepsilon_s \nabla V \nabla\partial_t V + \rho_L c_L \partial_t T_L - \operatorname{div}(\kappa_L \nabla T_L)\\ &+ [E_c - T_L E_c'](\partial_t n - q^{-1} \operatorname{div} J_n) - n E_c' \partial_t T_L - q^{-1} J_n \cdot \nabla[E_c - T_L E_c']\\ &- [E_v - T_L E_v'](\partial_t p + q^{-1} \operatorname{div} J_p) + p E_v' \partial_t T_L - q^{-1} J_p \cdot \nabla[E_v - T_L E_v']\\ &+ \operatorname{div}(V J_n) + \operatorname{div}(V J_p) + \partial_t w - \operatorname{div} J_w + \partial_t w_p + \operatorname{div} J_{w_p}.\end{aligned}$$

Employing the Poisson equation (3.5) and the continuity equations for the charge carriers (3.1), (3.6) leads to the relation

$$\varepsilon_s \Delta\partial_t V = q(\partial_t n - \partial_t p) = \operatorname{div} J_n + \operatorname{div} J_p. \tag{3.46}$$

Inserting (3.46) and using the energy-transport model equations leads to

$$\begin{aligned}0 =& - V(\operatorname{div} J_n + \operatorname{div} J_p) + \rho_L c_L \partial_t T_L - \operatorname{div}(\kappa_L \nabla T_L)\\ &- R(E_c - T_L E_c') + R(E_v - T_L E_v') + \operatorname{div}(V J_n) + \operatorname{div}(V J_p)\\ &- J_n \cdot \nabla V + W - J_p \cdot \nabla V + W_p - \frac{3}{2} k_B R(T_n + T_p)\\ &- n E_c' \partial_t T_L - q^{-1} J_n \cdot \nabla[E_c - T_L E_c'] + p E_v' \partial_t T_L - q^{-1} J_p \cdot \nabla[E_v - T_L E_v'].\end{aligned}$$

This finally leads to the heat flow equation

$$\partial_t T_L \left[\rho_L c_L - n E_c' + p E_c'\right] - \operatorname{div}(\kappa_L \nabla T_L) = H \tag{3.47}$$

with the heat source term given by

$$\begin{aligned}H =& - W - W_p + R\left(E_g - T_L E_g' + \frac{3}{2} k_B (T_n + T_p)\right)\\ &+ q^{-1} J_n \cdot \nabla[E_c - T_L E_c'] + q^{-1} J_p \cdot \nabla[E_v - T_L E_v'],\end{aligned} \tag{3.48}$$

where $E_g = E_c - E_v$ denotes the energy gap.

For non-degenerate homostructure devices we can neglect the space dependency of the energy bands. If we further on neglect the direct dependency of the energy bands on the lattice temperature (what we can do as it is small [87]) we end up with a simpler heat source term

$$H = - W - W_p + R\left(E_g - T_L E_g' + \frac{3}{2} k_B (T_n + T_p)\right). \tag{3.49}$$

In order to complete the thermal model for the lattice temperature we have to include the radiation to the environment. The radiation occurs at the physical boundary of the device, only. It can be assumed to be proportional to the temperature difference between lattice temperature T_L and environmental temperature T_{env}. Including this into the heat flow equation we end up with the complete model for the semiconductor device:

$$\begin{aligned}
\varepsilon_s \Delta V =& q(n - p - C(x)),\\
\partial_t n - q^{-1} \operatorname{div} J_n = -R, \qquad & \partial_t w - \operatorname{div} J_w = -J_n \nabla V + W - \frac{3}{2} k_B T_n R,\\
\partial_t p + q^{-1} \operatorname{div} J_p = -R, \qquad & \partial_t w_p + \operatorname{div} J_{w_p} = -J_p \nabla V + W_p - \frac{3}{2} k_B T_p R,\\
\rho_L c_L \partial_t T_L - \operatorname{div}(\kappa_L \nabla T_L) =& - W - W_p + R \left(E_g + \frac{3}{2} k_B (T_n + T_p) \right)\\
& - S_L (T_L - T_{\text{env}}),
\end{aligned} \tag{3.50}$$

where $S_L = S_L(x)$ denotes the transmission function and models the thermal radiation of the device. If the model is stated in the physical 3 dimensions, the transmission function $S_L(x)$ is zero unless on the boundary. If we employ a reduced one- or two-dimensional model, the physical boundary of the device does not coincide with the model boundary what results in the effect that $S_L(x)$ also attains values different from zero inside the domain Ω_S. Analogous to the thermal radiation stated in § 2, the complete radiation can be considered to be proportional to the physical surface of the modeled device.

A deeper look to this model shows that the Joule heating term $-J\nabla V$ appears as source term for the thermal energy of the charge carriers. As heat source for the crystal lattice the energy relaxation terms are considered. In the drift-diffusion case, however, the equation for the carrier energy and with that the relaxation term disappears.

If we model the hole subsystem by the drift-diffusion model, as stated in § 3.2, we apply the source term (3.35) suggested by Adler. Thus the relaxation term W_p is replaced by $J_p \nabla V$ and moreover the term $\frac{3}{2} k_B T_p R$ vanishes in order to keep the energy balance. We summarize the heat flow equation for the mixed energy-transport and drift-diffusion model in the following remark.

Remark 3.1. *If we exchange the energy-transport model for the holes by the drift-diffusion model (as stated in § 3.2) the heat flow equation changes into*

$$\begin{aligned}
\rho_L c_L \partial_t T_L - \operatorname{div}(\kappa_L \nabla T_L) =& - W - J_p \nabla V + R \left(E_g + \frac{3}{2} k_B T_n \right)\\
& - S_L (T_L - T_{\text{env}}).
\end{aligned} \tag{3.51}$$

Obviously the significant difference between these two approaches is, that the Joule heat affects the crystal lattice directly if the charge carriers subsystems are modeled by the drift-diffusion equations. If we use the energy-transport model for the carrier subsystems the Joule heat affects the charge carriers directly.

Boundary and initial conditions

The heat flow equation (3.50) has to be completed by initial and boundary conditions for the lattice temperature T_L. We pose the initial conditions

$$T_L(x,0) = T_{L,I} \quad \text{for } x \in \Omega_S.$$

We recall that the device boundary $\partial\Omega_S = \Gamma_C \cup \Gamma_I$ splits into two parts. The boundary part covered by contacts $\Gamma_C = \bigcup_{k=1}^{n_S} \Gamma_k$ and the insulating boundary Γ_I. We provide the following boundary conditions of mixed type

$$\nabla T_L \cdot \nu = 0 \qquad \text{on } \Gamma_I, \tag{3.52}$$

$$-\kappa_L \nabla T_L = \nu \cdot \frac{T_L - T_a}{R_{\text{th}}} \qquad \text{on } \Gamma_C. \tag{3.53}$$

The first boundary condition (3.52) assumes perfect insulating boundary Γ_I. This choice is reasonable as besides the radiation no temperature exchange with the environment occurs. The radiation at the boundary is already taken into account by the transmission function S_L. At the contacts Γ_C we prescribe boundary conditions of mixed type to model the temperature exchange between the semiconductor device and the connected device (or interconnect) with the temperature T_a. The occurring proportionality constant R_{th} models the thermal resistance of the contact. If we, however, assume an infinite heat flux across the contacts, the lattice temperature coincides with the ambient temperature. This results in the boundary condition alternatively to (3.53)

$$T_L = T_a \qquad \text{on } \Gamma_C. \tag{3.54}$$

Finally we want to compare our result with those presented in literature.

Remark 3.2.

- *If we neglect the recombination and radiation terms in the source term of heat flow equation* (3.50) *completely, we get the same source term as used in* [**74**].
- *If we further on consider only the unipolar case, the equation coincides with the heat flow equation Knaipp coupled to the hydrodynamic model in* [**58**].

- *In the case of Maxwell-Boltzmann statistics our simplified heat source term* (3.50) *coincides with Wachutka's source term* (3.36) *presented in* [**101**]. *We namely can express the quasi Fermi potential as*

$$\phi_n = V - \frac{k_B T_n}{q} \ln\left(\frac{n}{n_i}\right) \qquad \text{and} \qquad \phi_p = V + \frac{k_B T_p}{q} \ln\left(\frac{p}{n_i}\right)$$

  with intrinsic carrier density n_i. *Inserting this to* (3.36) *leads with forward computation directly to* (3.50).

This shows that our approach is a proper one. Moreover the application of source term (3.48) allows for the consideration of band gap narrowing and the extension to heterostructure devices like laser diodes presented in § 3.3.

Chapter 4

Thermoelectric network-device coupling

4.1 Electric network-device coupling

Electric coupling of network device problems is not a new problem, neither from the engineering, nor from the mathematical point of view. First mathematical results for the coupled system have already been obtained in the late 80's in [**44**] and [**41**]. In both cases simple circuits have been considered, where, for instance, the current entering the semiconductor device has been expressed in terms of the applied voltage. This way the circuit was taken into account in terms of special boundary conditions for the device, what obviously leads to failure if we consider circuits containing more than one semiconductor device. In [**99**] this has been extended to a coupling of MNA (see § 1) and drift-diffusion equations, such that networks containing more than one semiconductor device described by the drift-diffusion model could be modeled. The coupled system of MNA- and drift-diffusion equations has been studied from the analytical as well as the numerical point of view in [**98**, **99**, **22**, **23**, **88**]. However, the coupled system of MNA and drift-diffusion equations does not allow for thermal consideration of the semiconductor devices. In this work we will apply the coupling described in [**99**] to the energy-transport model for semiconductors in order to allow for the thermal effects in the device.

For notational convenience we will restrict ourselves to the case of networks containing one semiconductor device, but it is easy to verify that the described procedure can be extended to the case of several devices.

Coupling via semiconductor current

We remember from § 1 that the network equations in the charge oriented formulation are described by

$$\mathcal{A}_C \frac{d\widetilde{Q}_C}{dt}(\mathcal{A}_C^\top e, t) + \mathcal{A}_R g_R(\mathcal{A}_R^\top e) + \mathcal{A}_L i_L + \mathcal{A}_v i_v = -\mathcal{A}_i i_s, \tag{4.1}$$

$$\frac{d\widetilde{\Phi}_L}{dt}(i_L, t) - \mathcal{A}_L^\top e = 0, \tag{4.2}$$

$$\mathcal{A}_v^\top e = v_s \tag{4.3}$$

with the unknown node potentials e, the current through voltage sources i_V and the current through inductors i_L. The incidence matrices thereby consist of the entries $-1, 0, 1$ only.

When considering circuits containing semiconductor devices, the semiconductor current has to be included in the Kirchhoff current law (4.1). The total semiconductor current is given by the corresponding density

$$J_{\text{tot}} = J_n + J_p + J_d. \tag{4.4}$$

which consists of three parts, the electron current density J_n, the hole current density J_p and the displacement current density $J_d = -\varepsilon_s \partial_t \nabla V$ caused by the electric potential. The displacement current appears in transient models only and guarantees charge conservation. Indeed, differentiating the Poisson equation (3.5) with respect to time and replacing the time derivatives of the particle densities by the corresponding conservation laws (3.1) and (3.6), we obtain

$$\operatorname{div} J_{\text{tot}} = \operatorname{div}(J_n + J_p) - \partial_t(n - p) = 0.$$

Using Gauss' law we then obtain for the complete charge Q_S of the device

$$\frac{dQ_S}{dt} = \int_\Gamma J_{\text{tot}} \cdot \nu \, d\sigma = \int_\Omega \operatorname{div} J_{\text{tot}} \, dx = 0. \tag{4.5}$$

We finally get for the semiconductor current leaving one terminal of the device

$$j_S^k = \int_{\Gamma_k} J_{\text{tot}} \cdot \nu \, d\sigma \tag{4.6}$$

if terminal k corresponds to the boundary part Γ_k.

As the sum of all semiconductor currents is zero we can express the current through one terminal by the negative sum of the currents leaving all other terminals. We can choose one terminal (usually the bulk terminal) as reference terminal and denote by j_S the vector containing all terminal

currents except for the reference terminal. In the one-dimensional case there remains only one terminal and the current is given by

$$j_S(t) = J_n(0,t) + J_p(0,t) - \varepsilon_s \partial_t V_x(0,t).$$

In order to include the current into the KCL (4.1) we define the semiconductor incidence matrix according to [**99**]:

Definition 4.1. *For an electric network consisting of n_n nodes containing one semiconductor device with n_S terminals we define the (reduced) semiconductor incidence matrix $\mathcal{A}_S = (a_{ik}^S) \in \mathbb{R}^{(n_n-1)\times(n_S-1)}$ via*

$$a_{ik}^S = \begin{cases} 1 & \text{if the current } j_k \text{ enters the circuit node } i, \\ -1 & \text{if the reference terminal is connected to the node } i, \\ 0 & \text{else.} \end{cases}$$

With this definition the matrix $\mathcal{A}_S$ has the same form as the incidence matrices given in Definition 1.1. Finally, the Kirchhoff current law for the circuit containing the semiconductor device reads

$$\mathcal{A}_C \frac{d\widetilde{Q}_C}{dt}(\mathcal{A}_C^\top e) + \mathcal{A}_R g_R(\mathcal{A}_R^\top e) + \mathcal{A}_L i_L + \mathcal{A}_v i_v + \mathcal{A}_S j_S = -\mathcal{A}_i i_s. \tag{4.7}$$

Coupling via the node potentials

The second part of the electric coupling between the semiconductor device and the circuit is realized via the boundary conditions for the potential in the device. We recall from § 3.2.1 that the electric potential at the boundary of the device is given as the sum of the applied voltage and the built-in potential V_{bi}. If the terminal (and thus the contact) k of the device is connected to circuit node i, the boundary conditions are given consequently by

$$V(t) = e_i(t) + V_{\mathrm{bi}} \qquad \text{on } \Gamma_k \tag{4.8}$$

where e_i denotes the node potential in node i.

The coupled network-device system

Thus the coupled system of the electric network equations and the energy-transport equations for the semiconductor device forms a partial differential-algebraic system of parabolic type. For a reliable and efficient numerical simulation, it is important to know the index of the PDAE system. It has been shown in [**97**] that the coupled system of MNA- and drift-diffusion equations is of (tractability) index one if and only if the network(s) without the semiconductors satisfy some topological conditions, i.e., if they contain neither

CV-loops nor LI-cutsets. Here, a loop consisting of capacitors and voltage sources only is called a CV-loop, whereas a cutset containing inductors and current sources only is called an LI-cutset. In [**98**] it was proved that the index of the coupled system is at most two under weak conditions on the circuit (local passivity, no shortcuts). Moreover, the index of the coupled system is two if and only if the circuit contains LI-cutsets or CVS-loops (loops of capacitors, voltage sources, and semiconductors) with at least one voltage source or one semiconductor device. The same results were obtained in [**88**] for the discretized drift-diffusion equations. A sensitivity analysis generalizing the DAE index for finite systems to infinite ones was presented in [**23**] and applied to the coupled PDAE system. It was shown that the system is of index one if the voltages applied to the semiconductors are low and the network without the semiconductors is of index one. We also refer to the review paper [**48**].

For the coupled system consisting of the MNA- and the energy-transport equations, no results about the index are known. For the numerical treatment of the coupled system, however, we make the conjecture that the index is at most two, according to the drift-diffusion case.

4.2 Thermal network-device coupling

In § 2 we described the thermal effects in networks without special consideration of semiconductor devices. Thermal effects in semiconductor devices are taken into account by the energy-transport model in terms of the electron temperature as described in § 3.2. A more detailed consideration has been achieved by additional description of the lattice temperature by the heat flow equation, see § 3.4. By these models only the thermal effects in a single device are considered. In order to take into account the thermal influence of the semiconductor devices onto the other thermal elements the thermal description of the device has to be coupled to the thermal network described in § 2.

In [**6**] the thermal network has been coupled to semiconductor devices described by the energy-transport model. There, the lattice temperature has been considered as constant and the thermal interaction with the surrounding network elements was realized via hot electrons. In this work we will extend the models of [**6, 16**] and [**17**] and couple the thermal network to semiconductor devices via hot electrons and the lattice temperature. Moreover, we will describe a model that allows for the inclusion of possibly more-dimensional models for the devices into the thermal network. In both cases the device has to be treated different from thermal lines.

In the following we assume, that the device is only attached to nodes in the thermal network. If it is directly connected to a thermally distributed element in the electric circuit, this interface is enlarged by an artificial lumped

element according to the procedure in § 2. Then we define the thermal semiconductor incidence matrix:

Definition 4.2. *For the thermal network with m_n thermal nodes containing one semiconductor device with n_s terminals, the thermal semiconductor incidence matrix $\mathcal{A}_S^{\text{th}} = (a_{ij}^s) \in \mathbb{R}^{m_n \times n_S}$ is given by*

$$a_{ij}^s = \begin{cases} 1 & \text{if terminal } j \text{ is connected to thermal node } i, \\ 0 & \text{else.} \end{cases} \tag{4.9}$$

Coupling via the semiconductor heat flux

We recall from § 2 that one way of coupling between nodes and branches of the thermal network is realized via the thermal flux $\hat{\boldsymbol{F}}^d$ from the branches into the nodes, occurring in the lumped heat equation (2.4)

$$\hat{\boldsymbol{M}} d_t \hat{\boldsymbol{T}} = \hat{\boldsymbol{F}}^d - \hat{\boldsymbol{S}}(\hat{\boldsymbol{T}} - T_{\text{env}} \boldsymbol{I}) + \hat{\boldsymbol{P}}.$$

Now besides the heat flux from the thermal lines $\hat{\boldsymbol{F}}^d$ the semiconductor heat flux into the nodes has to be taken into account.

Heat flux

As a first approximation of the semiconductor heat flux the Fourier law (2.9) can be used. Thus, the device can be coupled to the thermal network analogous to the thermal lines. If we apply the energy-transport model to model the device, the flow of hot electrons contributes to the heat flux and has to be taken into account (see [**6**]). In the following we will motivate a physically reasonable expression for the semiconductor heat flux.

We first recall that for the energy u_E and energy flux J_u^E of the electric field it holds (compare (3.40),(3.46))

$$\partial_t u_E + \operatorname{div} J_u^E = -V \varepsilon_s \Delta \partial_t V = -V \operatorname{div}(J_n + J_p).$$

Inserting this into the energy conservation (3.37) for the total energy u

$$\partial_t u + \operatorname{div} J_u = 0$$

and considering the stationary case by neglecting all time derivatives gives

$$\operatorname{div}(J_u^L + J_u^n + J_u^w + J_u^p + J_u^{w_p}) = V \operatorname{div}(J_n + J_p),$$

with the notation from § 3.4. This is equivalent to

$$\operatorname{div}(J_u^L + J_u^n + J_u^w + J_u^p + J_u^{w_p} - V(J_n + J_p)) = -\nabla V (J_n + J_p).$$

With the current densities, given in (3.41) -(3.45), and again neglecting the direct dependence of the energy bands on the lattice temperature we get

$$\operatorname{div} J_{\mathrm{th}}^S = E J_{\mathrm{tot}} \tag{4.10}$$

with the thermal flux

$$J_{\mathrm{th}}^S = \left(-\kappa_L \nabla T_L - q^{-1}\left[E_c J_n + E_v J_p\right] - J_w + J_{w_p}\right). \tag{4.11}$$

Equation (4.10) clarifies that the flux given in (4.11) is responsible for the heat production caused by the dissipated power (compare [**6**]) and therefore can be regarded as heat flux. We remark that the flux given by (4.11) denotes the heat flux for the semiconductor device modeled via the bipolar energy-transport model. If we use the drift-diffusion model for the holes instead, as suggested in § 3.2 and § 3.3, it simplifies to

$$J_{\mathrm{th}}^S = \left(-\kappa_L \nabla T_L - q^{-1}\left[E_c J_n + E_v J_p\right] - J_w\right). \tag{4.12}$$

If we moreover neglect the heat flux caused by the flux of the holes - they are the minority charge carriers - the resulting heat flux in the device modeled by the energy-transport model for the electrons results in

$$J_{\mathrm{th}}^S = \left(-\kappa_L \nabla T_L - q^{-1} E_c J_n - J_w\right). \tag{4.13}$$

The first term in (4.13) describes the heat flux according to Fourier's law (2.9), as it occurs in thermal lines. The second term determines the energy flux of the electrons with an energy E_c per electron and the last term describes the flux of the thermal energy of the electrons.

In [**6**] a slightly different energy-transport model is applied to the semiconductor devices. The presented heat flux coincides with the electron energy flux J_w in our model. Obviously, our model is an extension of the model described in [**6**].

The coupling between the thermal flux of the devices and the thermal nodes can be expressed by use of the thermal semiconductor incidence matrix $\mathcal{A}_S^{\mathrm{th}}$ as

$$\hat{\boldsymbol{F}}^{\mathrm{S}} = \mathcal{A}_S^{\mathrm{th}} \begin{pmatrix} F_1^S(t) \\ \vdots \\ F_{n_S}^S(t) \end{pmatrix}, \qquad \text{with} \qquad F_k^S = \int_{\Gamma_k} J_{\mathrm{th}}^S \cdot \nu \, d\sigma. \tag{4.14}$$

where $\hat{\boldsymbol{F}}_i^{\mathrm{S}}$ stands for the complete heat flux from the semiconductor device into the thermal node i and F_k^S is the heat flux across the contact Γ_k of the device.

The lumped version of the heat flow equation for the thermal nodes changes into

$$\hat{\boldsymbol{M}} d_t \hat{\boldsymbol{T}} = \hat{\boldsymbol{F}}^S + \hat{\boldsymbol{F}}^d - \hat{\boldsymbol{S}}(\hat{\boldsymbol{T}} - T_{\mathrm{env}} \boldsymbol{I}) + \hat{\boldsymbol{P}}.$$

Coupling via the temperature in the thermal nodes

We recall from § 2.3 that for thermal lines the temperature at the boundary coincides with the temperature in the attached thermal nodes and the coupling can be expressed in terms of Dirichlet boundary conditions. For semiconductor devices, however, we also employ boundary conditions of Robin type (see (3.53). These conditions now have to be expressed in terms of the nodal temperature values $\hat{\boldsymbol{T}}$.

We recall that the semiconductor device is thermally described by the electron and the lattice temperature. The lattice temperature T_L is the primary important value for the coupling to the thermal network. According to § 3.4 it is described by the heat flow equation (3.50)

$$\rho_L c_L \partial_t T_L = \operatorname{div}(\kappa_L \nabla T_L) - S(T_L - T_{\text{env}}) + H, \tag{4.15}$$

with the material density ρ_L, the heat capacity c_L and heat conductivity κ_L. The source term H depends on the employed semiconductor model, for details see § 3.4. In the thermal network the heat flow equation (4.15) is completed by initial and boundary conditions

$$\begin{aligned} T_L(x,0) &= T_{L,I}(x), && \text{for } x \in \Omega_S, \\ -\kappa_L \nabla T_L(x,t) &= \nu \frac{T_L - T_{a,k}}{R_{\text{th}}}, && \text{on } \Gamma_k, k = 1,\dots,n_s, \quad t \in [0,\infty) \\ \nabla T_L \cdot \nu &= 0 && \text{on } \Gamma_I, t \in [0,\infty). \end{aligned} \tag{4.16}$$

For one-dimensional semiconductor models, we remark that equation (4.15) coincides with the heat flow equation for thermal lines (2.5), where the electro-thermal source term for the semiconductor device is given by the source term H.

We assume that the boundary $\Gamma_C = \bigcup_{k=1}^{n_s} \Gamma_k$ of the device consists of the contacts. The ambient temperature values $T_{a,k}$ at device contact k

$$\boldsymbol{T}_{L,C} := \begin{pmatrix} T_{a,1}(t) \\ \vdots \\ T_{a,n_s}(t) \end{pmatrix}$$

are given in terms of the external temperature $\hat{\boldsymbol{T}}$. With the thermal semiconductor incidence matrix $\mathcal{A}_S^{\text{th}}$ defined in (4.9) this is expressed as

$$\boldsymbol{T}_{L,C} = \mathcal{A}_S^{\text{th}\top} \hat{\boldsymbol{T}} \tag{4.17}$$

analogous to (2.8). If we assume Dirichlet boundary conditions for T_L, the same holds. Solely (4.16) changes into $T_L = T_{a,k}$.

The presented procedure to include one semiconductor device into the thermal network can be easily extended to the case of several semiconductor devices in the network by simply defining a thermal semiconductor incidence matrix for each device.

4.3 Electro-thermal coupling

Having described the coupling between the device and the electric as well as the thermal network we still have to clarify the coupling between the electric and thermal effects and especially between the electric and thermal networks. In this work we restrict ourselves to semiconductor devices and resistors as thermally relevant elements as they are the most important devices exhibiting this behavior. For a more detailed consideration of electro-thermal coupling we refer to [**16, 47**] where also transmission lines have been considered by use of the telegrapher's equation.

Thermal to electric coupling

Firstly we consider the thermal to electric coupling, this is the impact of the thermal effects on the electric behavior. This is taken into account in terms of the temperature dependency of electrically relevant material parameters.

For resistors we assume a quadratic dependence of the resistance on the corresponding temperature T_R

$$R \sim 1 + \alpha_1 T_R + \alpha_2 T_R^2 \tag{4.18}$$

with $\alpha_i \geq 0$ (comp. [**16**, §5.3]). The temperature influences the electric network equations by adding the temperature dependency to the conductivity of the resistors $g_R(\mathcal{A}_R^\top e, T_R)$ in the Kirchhoff current law (4.1) or (4.7) in the charge oriented MNA-equations.

In order to determine the temperature values T_R of the resistors from the temperature values in the thermal network we have to relate the resistive branches of the electric network to the nodes and branches of the thermal network. This is done by the following matrices:

Definition 4.3. *For an electric network containing n_R resistive branches, corresponding to a thermal network consisting of m_n thermal nodes and m_d thermal branches we define the matrices $\mathcal{K} = (k_{ij}) \in \mathbb{R}^{m_d \times n_R}$ and $\hat{\mathcal{K}} = (\hat{k}_{ij}) \in \mathbb{R}^{m_n \times n_R}$ via*

$$k_{ij} = \begin{cases} 1 & \text{if resitor } j \text{ corresponds to thermal branch } i \\ 0 & \text{else,} \end{cases} \tag{4.19}$$

$$\hat{k}_{ij} = \begin{cases} 1 & \text{if resitor } j \text{ corresponds to thermal node } i \\ 0 & \text{else.} \end{cases} \tag{4.20}$$

We notice that the resistors are considered as electrically lumped elements and thus the temperature values T_R have to be lumped values. If a resistor corresponds to a thermally distributed element we determine the lumped value $\widetilde{\boldsymbol{T}}_i^d$ out of the distributed values $\boldsymbol{T}_i^d$ by simply taking the mean value.

Thus, the temperature of the resistors is related to the temperature values occurring in the thermal network by

$$T_R = \hat{\mathcal{K}}^\top \hat{\boldsymbol{T}} + \mathcal{K}^\top \tilde{\boldsymbol{T}}^d,$$

where $\hat{\boldsymbol{T}}$ denotes the temperature in the thermal nodes.

For semiconductor devices the thermal to electric coupling is taken into account by the carrier mobilities. The carrier mobilities μ_n and μ_p namely depend on the carrier temperature and lattice temperature, see (3.12), (3.11), [**43**]. The temperature dependency of further material parameters is neglected in the examples we will present in this work. However, the model can be refined by taking into account the temperature dependency of the relaxation time τ_0 presented in [**12**], for instance.

Electric to thermal coupling

The electric to thermal coupling appears in the thermal consideration via the electric source terms in the heat equations. For the semiconductor device this is the heat source term H in the heat flow equation (3.50).

For the resistors the coupling is handled via the source terms P_i and $\hat{\boldsymbol{P}}$ occurring in the (lumped) heat flow equations (2.11) and (2.12), depending on whether the resistor is modeled as thermally lumped or distributed. These terms denote the heat production caused by the dissipated power of the resistors, which is given as the product of the current through the resistor and the applied voltage, see [**6, 16**]. With i_R containing the current through all resistors the power dissipated by all resistors in the electric network is given by

$$\mathcal{P}_R(e) = \operatorname{diag}(i_R)\mathcal{A}_R^\top e \in \mathbb{R}^{n_R}, \tag{4.21}$$

where $\mathcal{A}_R$ denotes the resistor incidence matrix of the electric network and e is the vector containing the node potentials in the circuit described in § 1. Observe that the entries of $\mathcal{P}_R$ are all lumped quantities. Thus if the i-th resistor is thermally modeled as lumped element the corresponding electro-thermal source $\mathcal{P}_{R,i}$ enters the lumped heat flow equation (2.12) directly. If the corresponding resistor is thermally modeled as distributed element, the lumped quantity has to be transferred into a distributed one. This can easily be done by use of a space dependent function $\zeta(x,t)$

$$\tilde{\mathcal{P}}_{R,i}(x,t) = \mathcal{P}_{R,i}\frac{\zeta(x,t)}{Z(t)}, \qquad \text{with} \qquad Z(t) = \int_0^{L_R} \zeta(x,t)\,dx.$$

The simplest choice thereby is to assume a constant local power dissipation within the resistor, such that

$$\tilde{\mathcal{P}}_{R,i}(x,t) = \frac{1}{L_R}\mathcal{P}_{R,i}, \qquad \text{for } x \in (0, L_R),$$

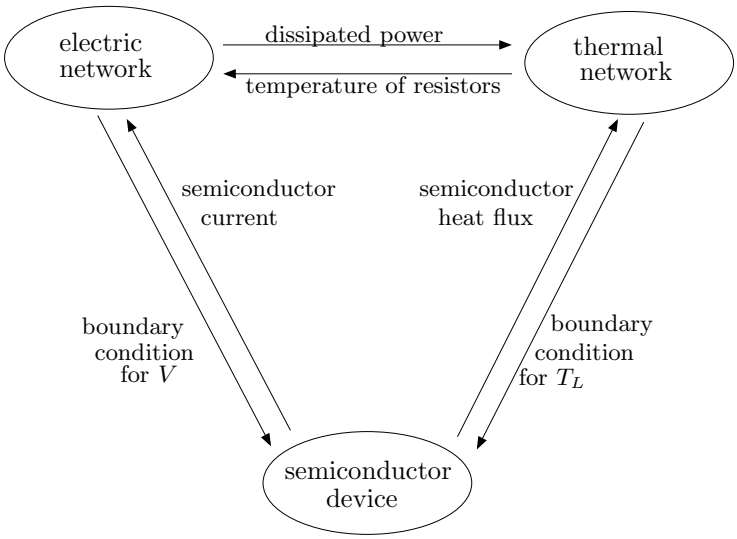

Figure 4.1: Schematic draw of the coupling conditions between electric network, thermal network and the semiconductor device.

with the length of the resistor model L_R. This simple choice corresponds to the assumption of a constant electric field inside the resistor. A more detailed discussion about the proper choice of the local power distribution function $\zeta(x,t)$ can be found in [**16**], where local thermal effects and passivity of the elements are taken into account.

With the matrices $\mathcal{K}$ and $\hat{\mathcal{K}}$ defined in (4.19) and (4.20) we can express the electro-thermal source terms as

$$\hat{\boldsymbol{P}} = \hat{\mathcal{K}}\mathcal{P}_R(e) \qquad \text{and} \qquad \boldsymbol{P} = \begin{pmatrix} P_1 \\ \vdots \\ P_{m_n} \end{pmatrix} = \mathcal{K}\tilde{\mathcal{P}}_R(e).$$

4.4 The complete coupled model

In § 1 we described the electric modeling of electric circuits by use of the modified nodal approach. In § 2 we described the accompanying thermal network model. In § 3 we described the electrical and thermal modeling of semiconductor devices. Finally the coupling conditions for the different types of coupling have been described in this chapter. They are schematically collected in Figure 4.1.

For sake of completeness we finally state the complete thermoelectric model of a circuit containing one semiconductor device, where only resistors and semiconductor devices are considered as thermally relevant:

Complete coupled thermoelectric network-device model

the electric network

$$\mathcal{A}_C \frac{d\widetilde{Q}_C}{dt}(\mathcal{A}_C^\top e, t) + \mathcal{A}_R g_R(\mathcal{A}_R^\top e, T_R) + \mathcal{A}_L i_L + \mathcal{A}_v i_v + \mathcal{A}_S j_S = -\mathcal{A}_i i_s,$$
$$\frac{d\widetilde{\Phi}_L}{dt}(i_L, t) - \mathcal{A}_L^\top e = 0,$$
$$\mathcal{A}_v^\top e = v_s,$$

the thermal network

$$M_i \partial_t T_i^d = \partial_x(\kappa_i \partial_x T_i^d) - S_i(T_i^d - T_{\text{env}}) + P_i, \qquad i = 1, ..., m_d$$
$$\hat{\boldsymbol{M}} d_t \hat{\boldsymbol{T}} = \hat{\boldsymbol{F}}^S + \hat{\boldsymbol{F}}^d - \hat{\boldsymbol{S}}(\hat{\boldsymbol{T}} - T_{\text{env}}\boldsymbol{I}) + \hat{\boldsymbol{P}},$$
$$\hat{\boldsymbol{F}}^d = \mathcal{A}_d^{\text{th}} \begin{pmatrix} \Lambda(0)\partial_x \boldsymbol{T}(0,t) \\ -\Lambda(L_{\text{th}})\partial_x \boldsymbol{T}(L_{\text{th}}, t) \end{pmatrix}, \qquad \begin{pmatrix} \boldsymbol{T}_0^d \\ \boldsymbol{T}_1^d \end{pmatrix} = \mathcal{A}_d^{\text{th}^\top} \hat{\boldsymbol{T}},$$

the semiconductor model

$$\epsilon_s \Delta V = q(n - p - C(x)),$$
$$\partial_t n - q^{-1} \operatorname{div} J_n = -R(n,p),$$
$$\partial_t w - \operatorname{div} J_w = -J_n \cdot \nabla V + W(n,T) - \frac{3}{2} k_B T_n R(n,p),$$
$$\partial_t p + q^{-1} J_p = -R(n,p),$$
$$\rho_L c_L \partial_t T_L - \operatorname{div}(\kappa_L \nabla T_L) = -W - J_p \nabla V + R\big(E_g + \frac{3}{2} k_B T_n\big) - S_L(T_L - T_{\text{env}}),$$

the electric-thermal network interface

$$T_R = \hat{\mathcal{K}}^\top \hat{\boldsymbol{T}} + \mathcal{K}^\top \tilde{\boldsymbol{T}}^d, \quad \text{with} \qquad \tilde{\boldsymbol{T}} = \operatorname{mean}(\boldsymbol{T}^d),$$
$$\hat{\boldsymbol{P}} = \hat{\mathcal{K}} \left[\operatorname{diag}(i_R)\mathcal{A}_R^\top e\right], \qquad P_i = \left(\mathcal{K}\tilde{\mathcal{P}}_R(e)\right)_i,$$
$$\left(\tilde{\mathcal{P}}_R(e)\right)_i = \left[\operatorname{diag}(i_R)\mathcal{A}_R^\top e\right]_i \cdot \frac{\zeta(x,t)}{Z(t)}, \qquad Z(t) = \int_0^1 \zeta(x,t)\, dx,$$

the electric network-semiconductor interface

$$j_S = J_n + J_p - \partial_t j_{d,S} \qquad \text{with} \qquad j_{d,S} = \varepsilon_s \partial_x V,$$
$$V(0,t) = e_i(t) + V_{\text{bi}}(0,t), \qquad V(1,t) = e_j(t) + V_{\text{bi}}(1,t),$$

the thermal network-semiconductor interface

$$\hat{\boldsymbol{F}}^S = \mathcal{A}_S^{\text{th}} \begin{pmatrix} J_{\text{th}}^S(0,t) \\ J_{\text{th}}^S(L,t) \end{pmatrix}, \qquad T_{L,C} = \mathcal{A}_S^{\text{th}^\top} \hat{\boldsymbol{T}},$$
$$\text{with} \quad J_{\text{th}}^S = \left(-\kappa_L \nabla T_L - q^{-1} E_c J_n - J_w\right).$$

Part II

Discretization and numerical solution of thermoelectric coupled network-device systems

Chapter 5

Nondimensionalization

As the values of parameters and variables occurring in the semiconductor models cover a wide range, for the numerical treatment it is reasonable to scale the values to the magnitude of 1 and make the equations dimensionless. As the scaled semiconductor equations will be coupled to models for optoelectronic effects as well as network and heat flow equations, we employ the scaling for these equations as well.

5.1 Transport equations

Firstly, we scale the semiconductor model presented in § 3.2, consisting of the energy-transport equations for the electrons, the drift-diffusion equations for the holes and the Poisson equation for the potential.

Let C_m be the maximum value of the doping profile, L the device diameter, $\mu_0 = \max(\mu_{n,0}, \mu_{p,0})$ the maximum value of the low field mobilities and $T_0 = 300\text{K}$. With the thermal voltage $U_T = \frac{k_B T_0}{q}$ we define the time scaling factor $t_0 = \frac{L^2}{\mu_0 U_T}$. Then we employ the following scaling

$$x \to Lx, \quad t \to t_0 t, \quad \tau_0 \to t_0 \tau_0, \quad \tau_n \to t_0 \tau_n, \quad \tau_p \to t_0 \tau_p.$$

The electron, hole and intrinsic density as well as the doping profile are scaled by the maximum value of the doping profile C_m

$$n \to C_m n, \qquad p \to C_m p, \qquad n_i \to C_m n_i, \qquad C \to C_m C. \tag{5.1}$$

The temperature values are scaled by $T_0 = 300\text{K}$, the mobilities by μ_0, voltages by the thermal voltage and the energy values by $k_B T_0$

$$\begin{aligned} &T_n \to T_0 T_n, \qquad T_L \to T_0 T_L \qquad \mu_n \to \mu_0 \mu_n, \qquad \mu_p \to \mu_0 \mu_p, \\ &V \to U_T V, \quad V_{\text{ap}} \to U_T V_{\text{ap}}, \quad V_{\text{bi}} \to U_T V_{\text{bi}}, \quad E_{c/v} \to k_B T_0 E_{c/v}. \end{aligned}$$

This results in the scaling of the current densities

$$J_{n,p} \to \frac{q \mu_0 U_T C_m}{L} J_{n/p}, \qquad J_w \to \frac{q \mu_0 U_T^2 C_m}{L} J_w. \tag{5.2}$$

The Auger recombination parameters C_n and C_p finally are scaled by

$$C_n \to (C_m^2 t_0)^{-1} C_n, \qquad C_p \to (C_m^2 t_0)^{-1} C_p.$$

For notational convenience we will not rename the scaled quantities.

5.1.1 Drift-diffusion formulation of the scaled ET-equations

In the following, we will introduce the drift-diffusion like formulation of the scaled energy-transport model, since this allows for a good approximation of the current densities (see 6.2 and, e.g. [**11, 25, 26**]). In [**34**] the drift-diffusion formulation is presented for the energy-transport model with constant lattice temperature. It can also be applied to the non isothermal lattice model. For this we define the variables $g_n = \widetilde{\mu}_n n$, $g_w = \frac{3}{2}\widetilde{\mu}_n n T_n$ and $g_p = \widetilde{\mu}_p p$, where the mobility parameters are given as

$$\widetilde{\mu}_n = \frac{\mu_n}{T_L^{\alpha_n - 1}}, \qquad \widetilde{\mu}_p = \frac{\mu_p}{T_L^{\alpha_p - 1}}, \tag{5.3}$$

with α_n and α_p introduced in (3.12). This way the lattice temperature dependency of the mobilities is given directly in the parameters $\widetilde{\mu}_n, \widetilde{\mu}_p$. With this we write the scaled formulation of (3.1)-(3.7) as

Drift-diffusion formulation of the ET-model

$$\widetilde{\mu}_n^{-1}\partial_t g_n - \operatorname{div} J_n = R(\widetilde{\mu}_n^{-1} g_n, \widetilde{\mu}_p^{-1} g_p,) \tag{5.4}$$

$$\widetilde{\mu}_n^{-1}\partial_t g_w - \operatorname{div} J_w = -J_n \nabla V + W(g_n, g_w) - \frac{3}{2} T_n R(\widetilde{\mu}_n^{-1} g_n, \widetilde{\mu}_p^{-1} g_p,) \tag{5.5}$$

$$\widetilde{\mu}_p^{-1}\partial_t g_p + \operatorname{div} J_p = -R(\widetilde{\mu}_n^{-1} g_n, \widetilde{\mu}_p^{-1} g_p) \tag{5.6}$$

with the current densities

$$J_n = \nabla g_n - \frac{g_n}{T_n}\nabla V, \quad J_w = \nabla g_w - \frac{g_w}{T_n}\nabla V, \quad J_p = -\big(\nabla g_p + \frac{g_p}{T_L}\nabla V\big). \tag{5.7}$$

The electron temperature is now given by $T_n = 2g_w/3g_n$. Thus the energy-transport equations correspond (up to a sign) to the drift-diffusion equations, where g_n or g_w is replaced by g_p, T_n by T_L, and only the right-hand side is different. The advantage of this formulation is that it "diagonalizes" the cross-diffusion energy-transport model [**34**]. Under the assumption of constant (scaled) lattice temperature $T_L = 1$, the mobility parameters $\widetilde{\mu}_n, \widetilde{\mu}_p$ coincide with μ_n, μ_p, respectively, and the drift-diffusion formulation (5.4)-(5.7) coincides with the formulation in [**34**].

The scaled Poisson equation becomes

$$\lambda^2 \Delta V = \widetilde{\mu}_n^{-1} g_n - \widetilde{\mu}_p g_p - C(x), \qquad \text{with} \qquad \lambda^2 = \frac{\varepsilon_s U_T}{q C_m L^2} \tag{5.8}$$

with Debye length λ. The scaled displacement current density is given as

$$J_D = \partial_t j_{S,D}, \qquad \text{with} \qquad j_{S,D} = -\lambda^2 \nabla V. \tag{5.9}$$

The Fokker-Planck relaxation term (3.10) reads in the new variables

$$W(g_n, g_w) = c_n g_n - c_w g_w$$

with $c_n = \frac{3}{2}\frac{T_L}{\tau_0 \widetilde{\mu}_n}$ and $c_w = \frac{1}{\tau_0 \widetilde{\mu}_n}$, and the recombination terms (3.8) and (3.9) appear the same in the scaled formulation.

Boundary and initial conditions. The boundary and initial conditions (3.13)-(3.20) appear the same in the scaled formulation, where the initial and boundary conditions for g_n and g_w can be easily determined from (3.13) and (3.17)-(3.19). Merely the shape of the Robin type boundary conditions (3.21) and (3.22) on Γ_C changes slightly into

$$g_n + \theta_n^{-1} J_n \cdot \nu = g_{n,a}, \qquad g_p - \theta_p^{-1} J_p \cdot \nu = g_{p,a}, \tag{5.10}$$

$$\nabla g_w \cdot \nu - \theta_n (g_{w,a} - g_w) = \frac{3}{2}\theta_n g_{n,a}(T_n - T_a) + \frac{3}{2} g_n \nabla V \cdot \nu \tag{5.11}$$

with $g_{n,a} = \widetilde{\mu}_n n_a$, $g_{p,a} = \widetilde{\mu}_p p_a$ and $g_{w,a} = \widetilde{\mu}_n w_a$.

5.2 Scaled optoelectronic device equations

When the model equations for the optoelectronic effects in the devices, described in § 3.3, are coupled to the scaled transport equations an appropriate scaling has to be applied. The threshhold density n_{th} is scaled by C_m according to (5.1) and the remaining values and parameters in the spontaneous and stimulated recombination terms (3.25) are scaled as follows

$$B \to (t_0 C_m)^{-1} B, \quad v_g \to L t_0^{-1} v_g, \quad g_0 \to (L C_m)^{-1} g_0, \quad S \to L^3 C_m S.$$

For the band potentials, the eigenvalue of the waveguide equation (3.27), the velocity of light c and the angular frequency of the light ω, we use the following scaling

$$U_n \to U_T U_n, \quad U_p \to U_T U_p, \quad \beta \to L^{-1}\beta, \quad c \to L t_0^{-1} c, \quad \omega \to t_0^{-1}\omega.$$

All absorption parameters are scaled by the inverse device diameter and for the generation term (3.32) we apply the scaling

$$\alpha_{\text{f}} \to L^{-1}\alpha_{\text{f}}, \quad \alpha_{\text{ab}} \to L^{-1}\alpha_{\text{ab}}, \quad A \to L^2 A, \quad \frac{P_{\text{in}}}{\hbar} \to \frac{L^3 C_m}{t_0^2}\frac{P_{\text{in}}}{\hbar}.$$

The equations (3.24)-(3.32) remain the same, where solely the physical quantities are replaced by the scaled ones. For convenience, we summarize

the complete scaled model for a single-mode laser diode with constant lattice temperature T_L under the assumption of boundary conditions of Robin type:

Scaled model for laser diode

Poisson equation for the potential

$$\lambda^2 \Delta V = \widetilde{\mu}_n^{-1} g_n - \widetilde{\mu}_p g_p - C(x),$$

Energy-transport model with $V_n = V + U_n$

$$\widetilde{\mu}_n^{-1} \partial_t g_n - \operatorname{div} J_n = -R_g(\widetilde{\mu}_n^{-1} g_n, \widetilde{\mu}_p^{-1} g_p),$$
$$\widetilde{\mu}_n^{-1} \partial_t g_w - \operatorname{div} J_w = -J_n \cdot \nabla V_n + W(g_n, g_w) - \frac{3}{2} T_n R_g(\widetilde{\mu}_n^{-1} g_n, \widetilde{\mu}_p^{-1} g_p),$$
$$J_n = \nabla g_n - \frac{g_n}{T_n} \nabla V_n, \qquad J_w = \nabla g_w - \frac{g_w}{T_n} \nabla V_n,$$

Drift-diffusion model with $V_p = V + U_p$

$$\widetilde{\mu}_p^{-1} \partial_t g_p + \operatorname{div} J_p = -R_p(\widetilde{\mu}_n^{-1} g_n, \widetilde{\mu}_p^{-1} g_p), \qquad J_p = -\nabla g_p - \frac{g_p}{T_L} \nabla V_p,$$

Electric-optical interface

$$R_\nu = R_{\mathrm{SRH}} + R_{\mathrm{Au}} + Bnp + v_g g(\nu) |\Xi|^2 S \qquad \text{for } \nu = n, p$$
$$g(\nu) = g_0(\widetilde{\mu}_\nu^{-1} g_\nu - n_{\mathrm{th}}).$$

Waveguide equation and Photon rate equation

$$\left[\Delta + \frac{\omega^2}{c^2} \varepsilon_{\mathrm{opt}}(n)\right] \Xi(x) = \beta^2 \Xi(x),$$
$$\partial_t S = v_g \left(2\mathrm{Im}(\beta) - \alpha_f\right) S + R_{\mathrm{spont}}.$$

Boundary conditions:

$$J_n \cdot \nu = J_p \cdot \nu = J_w \cdot \nu = \nabla V \cdot \nu = \nabla T_n \cdot \nu = 0 \qquad \text{on } \Gamma_I$$
$$V = V_{\mathrm{ap}} + V_{\mathrm{bi}}, \qquad \nabla T_n \cdot \nu = 0 \qquad \text{on } \Gamma_C$$
$$J_n \cdot \nu = \theta_n(g_{n,a} - g_n), \qquad J_p \cdot \nu = \theta_p(g_p - g_{p_a}) \qquad \text{on } \Gamma_C$$
$$\nabla g_w \cdot \nu - \theta_n(g_{w,a} - g_w) = \frac{3}{2} \theta_n g_{n,a} \left(T_n - T_a\right) - \frac{3}{2} g_n \nabla V \cdot \nu \qquad \text{on } \Gamma_C.$$

Initial conditions:

$$g_n = g_{n,I}, \quad g_w = g_{w,I}, \quad g_p = g_{p,I}, \quad T_n = T_{n,I}, \quad S = S_I, \qquad \text{in } \Omega_S,\ t = 0.$$

5.3 Scaled heat flow equation

According to § 5.1 the recombination terms are scaled by $R \to (C_m/t_0)R$, the energy values by $k_B T_0$ and all temperature variables are scaled by the temperature $T_0 = 300$ K. Further on, we employ the scaling

$$\kappa_L \to L^2 k_B C_m t_0^{-1} \kappa_L, \quad \rho_L c_L \to k_B C_m \rho_L c_L, \quad S_L \to k_B C_m t_0^{-1} S_L.$$

Then the scaled heat flow equation for the energy-transport model reads

$$\begin{aligned}\rho_L c_L \partial_t T_L - \operatorname{div}(\kappa_L \nabla T_L) =& \frac{3}{2} n \frac{T_n - T_L}{\tau_0} + \frac{3}{2} p \frac{T_p - T_L}{\tau_{p,0}} + R\left[E_g + \frac{3}{2}(T_n + T_p)\right] \\ & - S_L(T_L - T_{\text{env}}).\end{aligned}$$

If we employ the drift-diffusion model for the holes instead, we get

$$\begin{aligned}\rho_L c_L \partial_t T_L - \operatorname{div}(\kappa_L \nabla T_L) =& \frac{3}{2} n \frac{T_n - T_L}{\tau_0} - J_p \nabla V + R\big[E_g + \frac{3}{2} T_n\big] \\ & - S_L(T_L - T_{\text{env}}),\end{aligned} \tag{5.12}$$

with the scaling from § 5.1 for J_p and V. The heat flux J_{th}^S given in (4.11)-(4.13) reads in the scaled formulation

$$J_{\text{th}}^S = \big(- \kappa_L \nabla T_L - E_c J_n - J_w\big). \tag{5.13}$$

5.4 Scaled thermoelectric network-device model

Electric network. The scaling of time in the semiconductor model also changes the time variable in the network equations, what enforces the scaling

$$t \to t_0 t, \qquad d/dt \to t_0^{-1} d/dt. \tag{5.14}$$

The node potential e appearing in the boundary conditions (4.8) for the Poisson equation are scaled by U_T, thus the boundary conditions become

$$V(t) = U_T^{-1} e_i(t) + V_{\text{bi}}, \quad \text{on } \Gamma_k \tag{5.15}$$

if network node i is connected with terminal k of the device.

Lastly, the semiconductor current has to be unscaled by $q\mu_0 U_T C_m/L$ according to § 5.1 before entering the Kirchhoff current law (4.7).

Thermal network. Also in the thermal network equations the time has to be scaled according to (5.14). The temperature $\hat{\boldsymbol{T}}$ in the coupling condition (4.17) has to be scaled by T_0, such that the coupling condition becomes

$$\boldsymbol{T}_{L,C} = \mathcal{A}_S^{\text{th}^\top} \hat{\boldsymbol{T}} T_0^{-1}.$$

Lastly, the heat flux (5.13) has to be unscaled by $q\mu_0 U_T^2 C_m/L$ before being coupled to the thermal network equations, according to (5.2).

Finally we present the dimensionless formulation of the complete thermoelectric network-device system presented on page 53, where we apply the drift-diffusion formulation of the energy-transport equations:

Scaled coupled thermoelectric network-device model

the electric network

$$t_0^{-1}\mathcal{A}_C\frac{d\widetilde{Q}_C}{dt}(\mathcal{A}_C^\top e,t)+\mathcal{A}_R g_R(\mathcal{A}_R^\top e,T_R)+\mathcal{A}_L i_L+\mathcal{A}_v i_v+\mathcal{A}_S j_S=-\mathcal{A}_i i_s,$$

$$t_0^{-1}\frac{d\widetilde{\Phi}_L}{dt}(i_L,t)-\mathcal{A}_L^\top e=0,$$

$$\mathcal{A}_v^\top e=v_s,$$

the thermal network

$$t_0^{-1}M_i\partial_t T_i^d=\partial_x(\kappa_i\partial_x T_i^d)-S_i(T_i^d-T_{\rm env})+P_i,\qquad i=1,...,m_d$$

$$t_0^{-1}\hat{\boldsymbol{M}}d_t\hat{\boldsymbol{T}}=\hat{\boldsymbol{F}}^S+\hat{\boldsymbol{F}}^d-\hat{\boldsymbol{S}}(\hat{\boldsymbol{T}}-T_{\rm env}\boldsymbol{I})+\hat{\boldsymbol{P}},$$

$$\hat{\boldsymbol{F}}^d=\mathcal{A}_d^{\rm th}\begin{pmatrix}\Lambda(0)\partial_x\boldsymbol{T}(0,t)\\-\Lambda(L_{\rm th})\partial_x\boldsymbol{T}(L_{\rm th},t)\end{pmatrix},\qquad\begin{pmatrix}\boldsymbol{T}_0^d\\\boldsymbol{T}_1^d\end{pmatrix}=\mathcal{A}_d^{{\rm th}^\top}\hat{\boldsymbol{T}},$$

the semiconductor model

$$\lambda^2\Delta V=\widetilde{\mu}_n^{-1}g_n-\widetilde{\mu}_p^{-1}g_p-C(x),$$

$$\widetilde{\mu}_n^{-1}\partial_t g_n-\operatorname{div}J_n=-R(\widetilde{\mu}_n^{-1}g_n,\widetilde{\mu}_p^{-1}g_p),$$

$$\widetilde{\mu}_n^{-1}\partial_t g_w-\operatorname{div}J_w=-J_n\cdot\nabla V_n+W(g_n,g_w)-\frac{3}{2}T_nR_g(\widetilde{\mu}_n^{-1}g_n,\widetilde{\mu}_p^{-1}g_p),$$

$$\widetilde{\mu}_p^{-1}\partial_t g_p+\operatorname{div}J_p=-R(\widetilde{\mu}_n^{-1}g_n,\widetilde{\mu}_p^{-1}g_p),$$

$$\rho_L c_L\partial_t T_L-\operatorname{div}(\kappa_L\nabla T_L)=-W-J_p\cdot\nabla V+R\big(E_g+\frac{3}{2}T_n\big)-S_L(T_L-T_{\rm env}),$$

the electric-thermal network interface

$$T_R=\hat{\mathcal{K}}^\top\hat{\boldsymbol{T}}+\mathcal{K}^\top\tilde{\boldsymbol{T}}^d,\quad\text{with}\qquad\tilde{\boldsymbol{T}}=\operatorname{mean}(\boldsymbol{T}^d),$$

$$\hat{\boldsymbol{P}}=\hat{\mathcal{K}}\left[\operatorname{diag}(i_R)\mathcal{A}_R^\top e\right],\qquad P_i=\Big(\mathcal{K}\tilde{\mathcal{P}}_R(e)\Big)_i,$$

$$\Big(\tilde{\mathcal{P}}_R(e)\Big)_i=\Big[\operatorname{diag}(i_R)\mathcal{A}_R^\top e\Big]_i\cdot\frac{\zeta(x,t)}{Z(t)},\qquad Z(t)=\int_0^1\zeta(x,t)\,dx,$$

the electric network-semiconductor interface

$$j_S=L(q\mu_0U_TC_m)^{-1}(J_n+J_p-\partial_t j_{d,S})\quad\text{with}\quad j_{d,S}=\varepsilon_s\partial_x V,$$

$$V(0,t)=U_T^{-1}e_i(t)+V_{\rm bi}(0,t),\qquad V(1,t)=U_T^{-1}e_j(t)+V_{\rm bi}(1,t),$$

the thermal network-semiconductor interface

$$\hat{\boldsymbol{F}}^S=\mathcal{A}_S^{\rm th}\begin{pmatrix}J_{\rm th}^S(0,t)\\J_{\rm th}^S(1,t)\end{pmatrix},\qquad T_{L,C}=\mathcal{A}_S^{{\rm th}^\top}\hat{\boldsymbol{T}}T_0^{-1},$$

$$\text{with}\quad J_{\rm th}^S=L(q\mu_0U_T^2C_m)^{-1}\left(-\kappa_L\nabla T_L-E_cJ_n-J_w\right).$$

Chapter 6

Discretization of coupled network-device PDAEs

In the following we describe the discretization of the different subsystem occurring in the complete coupled system, consisting of the differential-algebraic electric and thermal network equations and the partial differential equations given by the energy-transport model. The focus thereby is on a proper choice of the time-discretization scheme, as it has to take into account the differential-algebraic character of the system. Moreover, we will apply a discretization scheme to the energy-transport equations that will allow to keep the positivity of the discrete charge carrier densities and the continuity of the device current densities.

For the time dependent system we apply Rothe's method, i.e. we discretize in time first. Thus we have to solve an elliptic PDAE in each time step. We notice, that employing the method of lines, instead, what seems suggestive for the parabolic system, does not allow to guarantee the positivity of the discrete particle densities, with the applied scheme for space discretization.

6.1 Time discretization with backward difference formulas

For the numerical integration of differential-algebraic equations (DAEs) we can employ Runge-Kutta methods or backward difference formulas (BDF). For Runge-Kutta methods applied to DAEs we refer to [**50**], for instance. Only implicit Runge-Kutta schemes are feasible for DAEs, and stiffly accurate methods provide the best properties. For instance, stiffly accurate methods for index-1 DAEs have the same convergence order as in the case

of the numerical integration of explicit ordinary differential equations. For other Runge-Kutta methods, order reduction in the algebraic part down to the stage order q occurs. For stiffly accurate methods for index-2 DAEs, an order reduction in the differential and algebraic part down to the order $q+1$ can be observed. For other methods, even stronger order reduction may occur.

Concerning BDF methods, k-step BDF (with $k < 7$) for index-1 DAEs are feasible for sufficiently small time steps, and they are convergent with the same order as in the case of explicit ordinary differential equations [**69**]. The numerical integration of index-2 DAEs with BDF is studied in [**24, 50**]. In [**96**], quasilinear index-2 DAEs, as they occur in circuit simulation, were examined. It has been shown that k-step BDF for $k < 7$ are feasible and weakly instable under suitable assumptions. The convergence order is the same as in the case of explicit ordinary differential equations.

In § 4.1, we made the conjecture, based on coupled drift-diffusion and network equations, that the index of the partial differential-algebraic system consisting of the energy-transport and MNA equations is not larger than two. Moreover we conjecture, that the index of the thermal network equations derived in § 2 is not larger than two. For the time discretization we employ BDFs. The simplest of those, the 1-step BDF, coincides with the implicit Euler method and is given by

$$\partial_t g(t_m) \approx (\triangle t_m)^{-1}\big(g^{(m)} - g^{(m-1)}\big),$$

where $g^{(k)}$ approximates $g(\cdot, t_k)$, and $\triangle t_m = t_{m+1} - t_m$.

As the BDF1 shows strong damping behavior, for certain applications it is preferable to employ the 2-step BDF, as its stability domain is significantly larger. For variable step sizes the BDF2 is given by

$$\partial_t g(t_{m+1}) \approx \alpha_{m+1} g^{(m+1)} - \alpha_m g^{(m)} + \alpha_{m-1} g^{(m-1)}, \tag{6.1}$$

where

$$\alpha_{m+1} = \frac{\triangle t_{m-1} + 2\triangle t_m}{\triangle t_m(\triangle t_{m-1} + \triangle t_m)}, \tag{6.2}$$

$$\alpha_{m-1} = \frac{\triangle t_m}{\triangle t_{m-1}(\triangle t_{m-1} + \triangle t_m)}, \qquad \alpha_m = \frac{\triangle t_{m-1} + \triangle t_m}{\triangle t_m \triangle t_{m-1}}, \tag{6.3}$$

For constant time step size $\triangle t$ the coefficients reduce to

$$\alpha_{m+1} = \frac{3}{2\triangle t}, \quad \alpha_m = \frac{2}{\triangle t}, \quad \alpha_{m-1} = \frac{1}{2\triangle t}.$$

We found that methods like Radau IIa are not suitable since the stiffness matrix coming from the finite-element discretization of the semiconductor equations does not provide an M-matrix after static condensation (see below

for details) and thus does not allow to keep positivity of the discrete carrier densities. Using BDF1 or BDF2 allows to keep the M-matrix property provided by the finite-element scheme, however, with restriction to the step size for the BDF2. Furthermore, higher-order schemes are not appropriate here, since the input signals may be discontinuous.

6.2 Space discretization using hybridized mixed finite elements

In the following we describe the discretization of the energy-transport equations coupled to the equations for the optoelectronic effects in the laser diode. The equations for simpler devices like photo diodes or *pn* diodes are discretized analogously. Solely the treatment of the recombination terms is slightly simpler. The discretization is described for time discretization with BDF1. BDF2 leads to a very similar treatment. We notice, that on from that point we consider the one-dimensional spatial model, only.

The Poisson equation is discretized in space by linear finite elements. Thus the discrete electric potential is piecewise linear and the approximation of the electric field $-V_x$ is piecewise constant. The waveguide equation (3.27) is discretized in space by standard finite elements, and the corresponding discretized eigenvalue problem is solved using the `eig` or `eigs` routine of `Matlab`®.

The energy-transport equations are discretized using the mixed finite-element method. We employ the drift-diffusion formulation (5.4)-(5.7) and omit the tilde superscript in the mobility parameters in the following.

After time discretization with the implicit Euler scheme for given V, T, p, S, $|\Xi|^2$, $\widetilde{g_n}$, and $\widetilde{J_n}$ from the previous iteration step, we can express the continuity equation at time $t_{m+1} = (m+1)\Delta t$ for the next iteration step by

$$-J_{j,x} + \sigma_j g_j = f_j, \quad J_j = g_{j,x} - \frac{g_j}{T_n} V_x, \quad j = 1, 2, \tag{6.4}$$

with $g_1 = g_n$ and $g_2 = g_w$, where the current densities $J_1 = J_n$ and $J_2 = J_w$ are given by (5.7) and

$$\sigma_1 = \widetilde{\sigma} + (\mu_n \triangle t)^{-1}, \tag{6.5}$$

$$\sigma_2 = \frac{3}{2} T_n \widetilde{\sigma} + (\mu_n \triangle t)^{-1} + (\mu_n \tau_0)^{-1} T_L, \tag{6.6}$$

$$f_1 = \widetilde{f} + (\mu_n \triangle t)^{-1} g_1^{(m)}, \tag{6.7}$$

$$f_2 = \frac{3}{2} T_n \widetilde{f} + (\mu_n \triangle t)^{-1} g_2^{(m)} - \widetilde{J_n} V_x + \frac{3}{2} T_a (\mu_n \tau_0)^{-1} \widetilde{g}_1. \tag{6.8}$$

Furthermore, (remark that it holds the relations $g_n = \mu_n n$, $g_p = \mu_p p$)

$$\widetilde{\sigma} = \mu_n^{-1}\Big(r(\mu_n^{-1}\widetilde{g}_1, p)p + C_n\mu_n^{-1}\widetilde{g}_1 p + C_p p^2 + Bp + v_g g_0|\Xi|^2 S\Big), \tag{6.9}$$

$$\widetilde{f} = r(\mu_n^{-1}\widetilde{g}_1, p)n_i + C_p p n_i^2 + C_n\mu_n^{-1}\widetilde{g}_1 n_i^2 + v_g g_0 n_{\rm th}|\Xi|^2 S, \tag{6.10}$$

where r is given as

$$r(n,p) = \frac{1}{\tau_p(n+n_i) + \tau_n(p+n_i)}$$

and $g_j^{(m)}$ is the value of g_j at time step t_m. We notice that for notational convenience we used the variable p instead of g_p. Moreover we notice that the recombination terms are partially approximated by values from the former iteration step, such that the continuity equations become linear in each iteration step.

If the zeroth-order term σ_i vanishes, the use of Raviart-Thomas finite elements in (6.4) provides a numerical scheme with a stiffness matrix which is an M-matrix, thus providing the positivity of the discrete particle density for positive boundary conditions. This property may not hold if $\sigma_i > 0$. In [**72**] Marini and Pietra have developed finite elements which guarantee the positivity of the particle densities for positive Dirichlet boundary data. We will show below that this property remains valid even for the Robin boundary conditions (3.21)-(3.22) with $\theta_{n/p} \geq 0$.

Next, we describe the discretization of (6.4) in the interval $(0,1)$ with Robin boundary conditions. For convenience, we omit the index j in (6.4). We introduce the uniform mesh $x_i = ih$, $i = 0, \ldots, N$, where $N \in \mathbb{N}$ and $h = 1/N$. In order to deal with the convection dominance due to high electric fields, we use exponential fitting. Assume in the following that the temperature is given by a piecewise constant function $\overline{T}_n$ (see (6.18) for the definition of $\overline{T}_n$) and that the electric potential V is a given piecewise linear function. Then we define a local Slotboom variable by $y = \exp(-V/\overline{T}_n)g$ in each subinterval $I_i = (x_{i-1}, x_i)$. Equation (6.4) can be written as

$$e^{-V/\overline{T}_n}J - y_x = 0, \quad -J_x + \sigma e^{V/\overline{T}_n}y = f \tag{6.11}$$

and the boundary conditions (3.21) transform to

$$y_x \cdot \nu - \theta_n(y_a - y) = 0 \quad \text{at } x = 0, 1, \tag{6.12}$$

where $y_a = e^{-V/\overline{T}_n}g_a$, and $g_a = \mu_n n_a$ (see § 5.1).

The ansatz space for the current density J consists of piecewise polynomials of the form $\psi_i(x) = a_i + b_i P_i(x)$ on each I_i with constants a_i, b_i and second-order polynomials $P_i(x)$ which are defined as follows. Let $P(x)$ be the unique second-order polynomial satisfying

$$\int_0^1 P(x)dx = 0, \quad P(0) = 0 \quad \text{and} \quad P(1) = 1.$$

Then $P(x) = 3x^2 - 2x$. We define $P_i(x)$ (depending on V) by

$$P_i(x) = -P\Big(\frac{x_i - x}{h}\Big) \quad \text{for } i_{\min} = i - 1,$$
$$P_i(x) = P\Big(\frac{x - x_{i-1}}{h}\Big) \quad \text{for } i_{\min} = i,$$

where $i_{\min}$ is the boundary node of I_i at which the potential attains its minimum. Notice that the minimum is always attained at the boundary since V is linear on I_i. In the case that V is constant in I_i, we define $P_i(x) = P((x - x_{i-1})/h)$.

Now we introduce as in [**34**] the finite-dimensional spaces

$$V_h = \{\psi \in L^2(0,1) : \psi(x) = a_i + b_i P_i(x) \text{ in } I_i,\ i = 1, \dots, N\},$$
$$W_h = \{\phi \in L^2(0,1) : \phi \text{ is constant in } I_i,\ i = 1, \dots, N\},$$
$$\Gamma_h = \{q \text{ is defined at the nodes } x_0, \dots, x_N\}.$$

The mixed-hybrid finite-element approximation of (6.11) is as follows: Find $J_h \in V_h$, $\overline{y_h} \in W_h$, and $y_h \in \Gamma_h$ such that

$$\sum_{i=1}^N \Big(\int_{I_i} Q_i J_h \psi dx + \int_{I_i} \overline{y_h} \psi_x dx - \Big[y_h \psi \Big]_{x_{i-1}}^{x_i} \Big) = 0, \tag{6.13}$$

$$\sum_{i=1}^N \Big(- \int_{I_i} J_{h,x} \phi dx + \int_{I_i} \sigma S_i^{-1} \overline{y_h} \phi dx \Big) = \sum_{i=1}^N \int_{I_i} f \phi dx, \tag{6.14}$$

$$\sum_{i=1}^N \big[q J_h \big]_{x_{i-1}}^{x_i} + q\theta_n (Q_1^{-1} y_0 + Q_N^{-1} y_N) = q\theta_n y_a (Q_1^{-1} + Q_N^{-1}), \tag{6.15}$$

for all $\psi \in V_h$, $\phi \in W_h$, and $q \in \Gamma_h$. The approximations

$$Q_i = \frac{1}{h} \int_{I_i} e^{-V(x)/\overline{T}_i} dx, \quad S_i = e^{-V_{\min}/\overline{T}_i}, \quad i = 1, \dots, N,$$

are introduced in order to treat accurately large gradients of the potential [**72**]. Here, $V_{\min}$ denotes the minimum value of V on I_i. Equation (6.13) is the weak formulation of the first equation in (6.11), together with the Slotboom transformation. Equation (6.14) is the discrete weak version of the second equation in (6.11). The third equation (6.15) expresses the weak continuity property of J_h together with the boundary conditions (6.12).

The variables J_h and $\overline{y_h}$ can be eliminated by static condensation. For this, we write the weak formulation in matrix-vector notation for the vectors of nodal values similarly as in [**52**]:

$$\begin{pmatrix} A & B^\top & -C^\top \\ -B & D & 0 \\ C & 0 & E \end{pmatrix} \begin{pmatrix} J_h \\ \overline{y_h} \\ y_h \end{pmatrix} = \begin{pmatrix} 0 \\ F \\ G_C \end{pmatrix}.$$

The matrices $A \in \mathbb{R}^{2N\times 2N}$, $B \in \mathbb{R}^{N\times 2N}$, $C \in \mathbb{R}^{(N+1)\times 2N}$ and $D \in \mathbb{R}^{N\times N}$ are given by the corresponding elementary matrices associated with the interval I_i, denoted by the superscript i:

$$A^i_{jk} = Q_i \int_{I_i} \psi_j \psi_k dx, \qquad B^i_{jk} = \int_{I_i} \phi_j \psi_{k,x} dx,$$
$$C^i_{jk} = \left[q_j \psi_k\right]_{x_{i-1}}^{x_i}, \qquad D^i_{jk} = S_i^{-1} \int_{I_i} \sigma \phi_j \phi_k dx,$$

where ψ_k, ϕ_k, and q_k are the canonical basis functions of the corresponding spaces. In the matrix $E \in \mathbb{R}^{(N+1)\times(N+1)}$, only the values

$$E_{11} = q_1 q_1 \theta_n Q_1^{-1},$$
$$E_{N+1,N+1} = q_{N+1} q_{N+1} \theta_n Q_N^{-1},$$

are non-zero. The vectors F and G_C represent the corresponding right-hand sides of (6.14) and (6.15), respectively.

Now, static condensation as in [**52**] can be applied. As the matrix A has a diagonal structure, it can be easily inverted, which allows to eliminate J_h. A similar argument for $BA^{-1}B^\top + D$ allows to eliminate y_h. This leads to the system

$$\widetilde{M} y_h = G, \tag{6.16}$$

where $\widetilde{M}$ and G are given by:

$$\widetilde{M} = CA^{-1}C^\top + E - CA^{-1}B^\top (BA^{-1}B^\top + D)^{-1} BA^{-1}C^\top,$$
$$G = G_C + CA^{-1}B^\top (BA^{-1}B^\top + D)^{-1} F.$$

If Dirichlet boundary conditions are considered, $E = 0$ and $G_C = 0$. In this case, Marini and Pietra proved that $\widetilde{M}$ is an M-matrix by showing that the elementary stiffness matrices are M-matrices. If Robin boundary conditions are prescribed, we observe that the matrix E does not have any contribution to internal elements. Thus, the corresponding elementary matrices are, as in the case of Dirichlet conditions, M-matrices. If $\theta_n > 0$, the contribution of E to the boundary elementary matrices consists in nonnegative entries to the diagonal. Thus, also the boundary elementary matrices have the M-matrix property. Adding all elementary matrices shows that $\widetilde{M}$ is an M-matrix.

In order to go back to the discrete natural unknown g_h, we use a discrete inverse Slotboom transformation. Multiplying $\widetilde{M}$ column by column by $e^{-V_i/\overline{T}_n}$, the final system for the unknown g_h becomes

$$M g_h = G. \tag{6.17}$$

Notice that M is an M-matrix since $\widetilde{M}$ does so, and thus, the positivity for the solution of (6.17) is guaranteed for positive right-hand side G. Actually,

G is positive if the right-hand side f in (6.4) is positive. This is the case for the electron density equation, since the separation of the recombination terms was done in such a way that f_1 and the zeroth-order term σ_1 are positive. An analogous discretization of the hole equations (5.6) ensures positivity for the discrete hole density as well. We cannot guarantee generally nonnegativity of the right-hand side for the energy equation since the term $-J_nV_x$ may be negative and large. However, we observed that $-J_nV_x$ is negative in few cases only, and by adjusting the step size in space and time we always obtained positive solutions.

The eliminated variables J_h, $\overline{y_h}$, or $\overline{g_h}$ can be computed a posteriori from the solution of (6.16) or (6.17) as in [**53**] and [**72**] by

$$\begin{aligned}\overline{y_h} &= \left[BA^{-1}B^\top + D\right]^{-1}\left(BA^{-1}C^\top y_h + F\right)\\ J_h &= A^{-1}\left(B^\top\left[BA^{-1}B^\top + D\right]^{-1}\left(-F - BA^{-1}C^\top y_h\right) + C^\top y_h\right).\end{aligned}$$

We notice that the constant part of the current approximation coincides with the current approximation suggested by Scharfetter and Gummel in [**83**]. As the applied Marini-Pietra elements can also be applied to a two-dimensional geometry, this scheme can be considered as an extension of the widespread Scharfetter-Gummel approximation.

In order to complete the scheme, we still have to specify how the piecewise constant temperature $\overline{T_n}$ is defined. The temperature is implicitly defined in terms of g_1 and g_2, $T_n = 2g_2/3g_1$. Hence, we set

$$\overline{T}_{n,i} = \frac{1}{2}(T_{n,i} + T_{n,i-1}), \quad \text{where } T_{n,i} = \frac{2g^i_{2,h}}{3g^i_{1,h}}. \tag{6.18}$$

Remark 6.1. *For time discretization with BDF1 we observe that the positivity of the discrete particle densities is fulfilled by the described discretization scheme without any restriction on the time step size $\triangle t$. If we employ BDF2 for the time discretization, however, the term f_1 in (6.7) changes into*

$$f_1 = \widetilde{f} + \alpha_m\mu_n^{-1}g_1^{(m)} - \alpha_{m-1}\mu_n^{-1}g_1^{(m-1)},$$

with α_m, α_{m-1} given in (6.3). In order to guarantee nonnegativity of f_1 we have to ensure that $\alpha_m\mu_n^{-1}g_1^{(m)} - \alpha_{m-1}\mu_n^{-1}g_1^{(m-1)} \geq 0$ what in the case of $g^{(m)} < g^{(m-1)}$ implies the restriction on the time step size

$$\triangle t_m \leq \frac{g^{(m)} + (g^{(m)}g^{(m-1)})^{\frac{1}{2}}}{g^{(m-1)} - g^{(m)}}\triangle t_{m-1}. \tag{6.19}$$

For $g^{(m)} \geq g^{(m-1)}$ no restriction on $\triangle t_m$ is needed as obviously $\alpha_m > \alpha_{m-1}$.

Remark 6.2. *The time discretized drift-diffusion equations for the holes* (5.6)-(5.7) *reads analogous to* (6.4)

$$J_{p,x} + \sigma_p g_p = f_p, \qquad J_p = -g_{p,x} - \frac{g_p}{T_L} V_x, \tag{6.20}$$

where the zeroth-order term and the right hand side are given by

$$\sigma_p = (\mu_p \triangle t)^{-1} + \mu_p^{-1}\big(r(n, \mu_p^{-1}\widetilde{g}_p)n + C_n n^2 + C_p n \mu_p^{-1}\widetilde{g}_p + Bn + v_g g_0 |\Xi|^2 S\big),$$
$$f_p = (\mu_p \triangle t)^{-1} g_p^{(m)} + r(n, \mu_p^{-1}\widetilde{g}_p)n_i + C_n n n_i^2 + C_p \mu_p^{-1}\widetilde{g}_p n_i^2 + v_g g_0 n_{\mathrm{th}} |\Xi|^2 S,$$

where $g_p^{(m)}$ denotes the solution from the former time step and $\widetilde{g}_p$ the solution from the former iteration step. For notational convenience we stated the dependency on the electron density in terms of n instead of g_n.

We notice that the modal gain in the stimulated emission term is approximated by $g = g_0(p - n_{\mathrm{th}})$ according to (3.26) as this guarantees the non-negativity of σ_p and f_p. The space discretization of (6.20) is accomplished analogous to the described procedure for the energy-transport equations. For details see [**72**].

Remark 6.3. *For non-optoelectronic devices like pn or ballistic diodes the same discretization technique applies. Solely the values of $\widetilde{\sigma}$ and $\widetilde{f}$ in* (6.9) *and* (6.10) *change into*

$$\widetilde{\sigma} = \mu_n^{-1}\Big(r(\mu_n^{-1}\widetilde{g}_1, p)p + C_n \mu_n^{-1}\widetilde{g}_1 p + C_p p^2\Big), \tag{6.21}$$
$$\widetilde{f} = r(\mu_n^{-1}\widetilde{g}_1, p)n_i + C_p p n_i^2 + C_n \mu_n^{-1}\widetilde{g}_1 n_i^2, \tag{6.22}$$

as we do not have to consider spontaneous and stimulated recombination effects. The expression σ_p and f_p in Remark 6.2 change analogously.

The described discretization technique applies to the case of isothermal and non isothermal lattice modeling likewise. We notice that for non isothermal lattice modeling the mobility parameters μ_n and μ_p have to be replaced by the values $\widetilde{\mu}_n$ and $\widetilde{\mu}_p$ given in (5.3).

6.3 Discretization of the heat flow equations

The heat flow equations in the thermal network as well as the heat flow equation for the semiconductor device are discretized in time by by BDF1 or BDF2, according to § 6.1. After time discretization with the implicit Euler scheme for given V, T_n, R, g_1 and J_p the heat flow equation at time $t_{m+1} = (m+1)\triangle t$ can be expressed as

$$-\operatorname{div}(\kappa_L \nabla T_L) + \sigma_L T_L = f_L, \tag{6.23}$$

with

$$\sigma_L = \frac{3}{2}\frac{g_1}{\mu_n \tau_0} - \frac{3}{2}R + S_L + \frac{\rho_L c_L}{\triangle t}, \tag{6.24}$$

$$f_L = \frac{3}{2}\frac{g_1}{\mu_n \tau_0} T_n - J_p \nabla V + R\big[E_g + \frac{3}{2}T_n\big] + S_L T_{\text{env}} + \frac{\rho_L c_L}{\triangle t} T_L^{(m)}. \tag{6.25}$$

Thereby $T_L^{(m)}$ determines the lattice temperature at the former time step t_m. For time discretization with BDF2 or variable step size the last term in (6.24) and (6.25) changes according to (6.2) and (6.3), respectively.

The time discretized version of the space distributed heat flow equations (in the network and for the device) are space-discretized by linear finite elements. Thus the distributed temperatures in the the thermal network are assumed to be piecewise linear. This coincides with a simple finite-difference approximation.

Chapter 7

Iterative algorithms

The complete thermoelectric network-device model, presented on page 62, obviously builds a complex system of equations. The numerical solution therefore enforces special consideration. The same holds for the models for the single devices, as for the laser diode presented on page 60. In both cases the solution can be determined using the Newton-method for the entire system, what either enforces the very expensive and moreover instable numerical computation of the corresponding Jacobian, or the direct implementation of the Jacobian. This, in turn, hampers the maintenance of the code and complicates the extension of the existing code, as simple changes in the model mostly influence the Jacobian. The numerical simulation of new and smaller semiconductor devices and integrated circuits enforces the modification of existing codes in order to allow for dependencies that could be neglected for bigger devices. Therefore the consideration and development of iterative solvers is of high interest in industrial application.

In this chapter we will give a description of the iterative solvers we developed and applied for the simulation of one-dimensionally modeled optoelectronic devices and for the thermoelectric simulation of bipolar electric devices. Moreover, we will state a simple iterative algorithm we applied to solve the coupled network-device systems presented in this work.

7.1 Computation of thermal equilibrium

As mentioned in § 3.2.2, the state of thermal equilibrium is a distinguished one in semiconductor devices. For the transient computations presented in this work we always assume the state of thermal equilibrium as initial state of the devices. Moreover, for stationary computations, like the determination of current-voltage characteristics, the thermal equilibrium values are used as initial guess for the Newton method or Gummel-type iterations as described below. Here we give a short description of the computation of the equilibrium values.

In the scaled formulation the equilibrium densities are given as

$$n_{\mathrm{eq}} = n_i e^{V_{\mathrm{eq}}}, \qquad p_{\mathrm{eq}} = n_i e^{-V_{\mathrm{eq}}},$$

where V_{eq} is the solution of the semilinear elliptic Poisson equation

$$\lambda^2 \Delta V = 2n_i \sinh(V_{\mathrm{eq}}) - C \qquad \text{in } \Omega_S, \tag{7.1}$$

with the boundary conditions

$$V_{\mathrm{eq}} = \operatorname{arcsinh}\left(\frac{C}{2n_i}\right) \quad \text{on } \Gamma_C, \qquad \nabla V_{\mathrm{eq}} \cdot \nu = 0 \quad \text{on } \Gamma_I.$$

Thus the system of energy-transport equations reduces to a semilinear Poisson equation and the state of thermal equilibrium can be computed by a damped Newton algorithm as described in Algorithm 1 (comp. [**51**]).

Algorithm 1 : Computation of equilibrium values

Initialize $V = \operatorname{arcsinh}\left(\frac{C}{2n_i}\right)$ in Ω_S

repeat

Set $n = n_i e^V$ and $p = n_i e^{-V}$

Solve

$$\lambda^2 \Delta \Psi - (p+n)\Psi = -\lambda^2 \Delta V + n - p - C \quad \text{in } \Omega_S$$
$$\Psi = 0 \quad \text{on } \Gamma_C \qquad\qquad \nabla \Psi \cdot \nu = 0 \quad \text{on } \Gamma_I$$

Set $V := V + t\Psi$ wit $t \in (0, 1]$

until *convergence*;

$V_{\mathrm{eq}} = V$

7.2 Nonequilibrium state for optoelectronic devices

Laser diode

For nonequilibrium states of electric devices several iteration procedures for the coupled system of drift-diffusion and Poisson equation have been proposed in literature. The first one was suggested by Gummel in [**49**]. In [**51, 52**] an extended Gummel-type iteration procedure is proposed for the stationary system of energy-transport, drift-diffusion and Poisson equation for bipolar devices, where the Chen model is used for the current relations in the energy-transport model.

We applied a Gummel-type iteration as described in [**51, 52**] to the model for the laser diode consisting of the energy-transport, drift-diffusion, Poisson-, waveguide- and rate equations (see page 60). For the simulation of the optoelectronic devices we assume the (scaled) lattice temperature

Algorithm 2 : Iterative solver for the laser model

repeat

(i) Let $\ell \in \mathbb{N}_0$ and $g_p^\star = g_p^{(\ell)}$, $g_n^\star = g_n^{(\ell)}$, $V = V^{(\ell)}$,$\overline{T}_n = T_n^{(\ell)}$.

(ii) Find S such that

$$S\big(1 - \triangle t v_g(2\mathrm{Im}(\beta^{(\ell)}) - \alpha_f)\big) = \widetilde{S} + B\mu_n^{-1} g_n^\star \mu_p^{-1} g_p^\star \triangle t.$$

(iii) **repeat**

(a) Set $V_n = V + U_n$ and find g_n in Ω_S such that

$$\begin{cases} -\operatorname{div} J_n + \sigma_1(g_p^\star, g_n^\star, \Xi^{(\ell)}, S, \triangle t) g_n = f_1(g_p^\star, g_n^\star, \Xi^{(\ell)}, S, \triangle t, \widetilde{g}_n), \\ J_n = \nabla g_n - \nabla V_n \overline{T}_n^{-1} g_n, \\ g_n + \theta_n^{-1} J_n \cdot \nu(x) = g_{1,a} \qquad \text{on } \Gamma_C; \end{cases}$$

(b) Set $V_p = V + U_p$ and find g_p in Ω_S such that

$$\begin{cases} -\operatorname{div} J_p + \sigma_p(g_p^\star, g_n^\star, \Xi^{(\ell)}, S, \triangle t) g_n = f_p(g_p^\star, g_n^\star, \Xi^{(\ell)}, S, \Delta t, \widetilde{g}_p), \\ J_p = -\nabla g_p - \nabla V_p g_p, \\ g_p - \theta_p^{-1} J_p \cdot \nu(x) = g_{p,a} \qquad \text{on } \Gamma_C; \end{cases}$$

(c) Set $n = \mu_n^{-1} g_n$, $p = \mu_p^{-1} g_p$ and $V_1 = V + \delta V$, where δV solves in Ω_S

$$\begin{cases} \lambda^2 \Delta(\delta V) - (p+n)\delta V = -\lambda^2 \Delta V + n - p - C, \\ \delta V = 0 \qquad \text{on } \Gamma_C; \end{cases}$$

(d) Set $g_n^\star := g_n$, $g_p^\star := g_p$, and $V := V_1$;

until $\|\delta V\|_2 < \min(tol_{\mathrm{int}}, d_1(\delta T)^{d_2})$, *with* δT *from step* (v);

(iv) Set $V_n = V + U_n$ and find g_w in Ω_S such that

$$\begin{cases} -\operatorname{div} J_w + \sigma_2(g_p^\star, g_n^\star, \Xi^{(\ell)}, S, \triangle t) g_w = f_2(g_p^\star, g_n^\star, \Xi^{(\ell)}, S, \Delta t, \widetilde{g}_w), \\ J_w = \nabla g_w - \nabla V_n \overline{T}_n^{-1} g_w, \\ \nabla g_w \cdot \nu - \theta_n(g_{w,a} - g_w) = \frac{3}{2}\theta_n g_{n,a}(\overline{T}_n - T_a) + \frac{3}{2} g_n \nabla V \cdot \nu(x) \quad \text{on } \Gamma_C \end{cases}$$

(v) Compute $\overline{T}_n = 2g_w/3g_n$ and $\delta T = \|\overline{T}_n - T_L\|_2$.

(vi) Define $V^{(\ell+1)} = V + \delta V$, where δV is the solution of (iii.c).

(vii) Find $\Xi^{(\ell+1)}$ and $\beta^{(\ell+1)}$ in Ω_S such that

$$\begin{cases} \big(\Delta + \frac{\omega^2}{c^2}\varepsilon_{\mathrm{opt}}\big)\Xi^{(\ell+1)} = (\beta^{(\ell+1)})^2 \Xi^{(\ell+1)}, \\ \Xi^{(\ell+1)} = 0 \qquad \text{on } \Gamma_C. \end{cases}$$

(viii) Set $g_n^{(\ell+1)} := g_n$, $g_w^{(\ell+1)} := g_w$, $g_p^{(\ell+1)} := g_p$, and $T_n^{(\ell+1)} := \overline{T}_n$.

until *convergence*;

to be constant $T_L = 1$. To solve the model equations for the laser diode at time $t_{m+1} = (m+1)\triangle t$, we take as initial values of the iteration the solution of the previous time step, $g_n^{(0)} = \widetilde{g}_n$, $g_w^{(0)} = \widetilde{g}_w$, $g_p^{(0)} = \widetilde{g}_p$, $V^{(0)} = \widetilde{V}$, $S^{(0)} = \widetilde{S}$, $\Xi^{(0)} = \widetilde{\Xi}$, and $\beta^{(0)} = \widetilde{\beta}$, here denoted with a tilde. Notice that in the one-dimensional situation, $\partial\Omega_S = \Gamma_C = \{0, 1\}$. We set $g_{n,a} = \mu_n n_a$, $g_{w,a} = \frac{3}{2}\mu_n n_a T_a$ and $g_{p,a} = \mu_p p_a$. The iterative procedure for the laser diode then is given in Algorithm 2. Recall that the value $\overline{T}_n$ is determined according to (6.18).

We stop the iteration procedure if the relative difference of two consecutive iterations of the discrete values $(g_n^{(\ell)}, g_w^{(\ell)}, g_p^{(\ell)}, T_n^{(\ell)})$, $(S^{(\ell)}, \Xi^{(\ell)})$ are smaller in the Euclidean norm than the tolerances $\mathrm{tol}_{\mathrm{el}}$ and $\mathrm{tol}_{\mathrm{op}}$, respectively. We notice that the values ∂V as well as ∂T in Algorithm 2 are determined as the Euclidean norm of the corresponding discrete values.

The described scheme performs best for $\mathrm{tol}_{\mathrm{int}} = 10^{-6}$, $d_1 = 10^{-4}$, and $d_2 = 0.3$. Moreover, we have taken $\mathrm{tol}_{\mathrm{el}} = \mathrm{tol}_{\mathrm{op}} = 10^{-5}$. The boundary layers can be significantly reduced if we take $\theta_n = \theta_p = 2500$.

The discretization of the rate equation given in Algorithm 2.(ii) makes it necessary it to impose the restriction $\triangle t < 1/v_g(2\mathrm{Im}(\beta^{(\ell)}) - \alpha_f)$ on the time step to ensure the positivity of S. The choice $\triangle t = 10^{-12}\,\mathrm{s}$ proved to be appropriate for all presented simulations.

To achieve convergence if the applied voltage between two time steps changes abruptly (e.g. digital signal) and for stationary computations, the iterative scheme in Algorithm 2 is embedded into a continuation method for the applied bias, given in Algorithm 3. In the simulations, we have taken $\triangle V = 0.1\,\mathrm{V}$.

Algorithm 3 : Continuation of applied bias

repeat

(i) Apply the iterative Algorithm 2 for the applied voltage $\widetilde{V}_a = V_{a,\mathrm{old}} + \triangle V$ until the tolerance or the maximum number of iterations is reached. As an initial guess for all variables, the values from the former voltage step are used;

(ii) If the tolerance is achieved, set $V_{a,\mathrm{old}} = \widetilde{V}_a$, otherwise decrease voltage step size $\triangle V := \triangle V/2$;

until $\widetilde{V}_a = V_{\mathrm{ap}}$;

Photo diode

For the simulation of the photo diode, the iterative Algorithm 2 changes slightly. The solution of the rate equation (ii) and the solution of the waveguide equation (vii) become obsolete. The remaining algorithm then differs

only slightly from that one proposed in [**52**].

For the photo diode we additionally have to take into account, that the irradiation might change strongly between to time steps. In order to avoid failure of our algorithm that uses the values from the former time step as starting values, we embed the version of Algorithm 2 for the photo diode into a continuation method for the irradiation power analogous to Algorithm 3. In the simulations the value of $\triangle P = 2\,\mathrm{mW}$ worked well.

Algorithm 4 : Continuation of irradiation

repeat

(i) Apply the iterative algorithm for the irradiation $\widetilde{P} = P_{\mathrm{old}} + \triangle P$ until the tolerance or the maximum number of iterations is reached. As an initial guess for all variables, the values from the former irradiation step are used;

(ii) If the tolerance is achieved, set $P_{\mathrm{old}} = \widetilde{P}$, otherwise decrease the irradiation step size $\triangle P := \triangle P/2$;

until $\widetilde{P} = P_{\mathrm{in}}$;

7.3 Iterative solver including the heat equation

For non isothermal simulation we have to include the heat flow equation into the solver. Moreover we have to consider the temperature dependency of the mobilities (see (3.12), (5.3)). A simple extension of the solver presented in [**52**] proved to be successful for all considered examples. We present the iterative solver for bipolar thermoelectric simulation without consideration of optical effects. Thus, according to Remark 6.3, we only consider Shockley-Read-Hall and Auger recombination. The global iteration is given in Algorithm 5. The expressions $\sigma_1, \sigma_2, \sigma_p, f_1, f_2$ and f_p are given in (6.5)-(6.8) and Remark 6.2. The corresponding values of $\widetilde{\sigma}$ and $\widetilde{f}$ are given in Remark 6.3.

To solve the model equations we take as initial values for the iteration the solution of the previous time step, $g_n^{(0)} = \widetilde{g}_n$, $g_w^{(0)} = \widetilde{g}_w$, $g_p^{(0)} = \widetilde{g}_p$, $V^{(0)} = \widetilde{V}$ and $T_L^{(0)} = \widetilde{T}_L$, here denoted with a tilde. We notice that the initial values for the electron temperature $\overline{T}_n^{(0)}$ are determined according to (6.18).

We stop the iteration procedure, if the relative difference of two consecutive iterations of the discrete values $(g_n^{(\ell)}, g_w^{(\ell)}, g_p^{(\ell)}, T_n^{(\ell)}), T_L^{(\ell)}$ is smaller in the Euclidean norm than the tolerance tol. The iterative scheme performs best for $tol = 10^{-5}$ with the parameters $tol_{\mathrm{int}} = 10^{-3}$, $d_1 = 10^{-2}$ and $d_2 = 0.28$ (compare [**52**]).

The instruction to update the mobilities in Algorithm 5.(vii) seems to

Algorithm 5 : Iterative solver for non isothermal models

repeat

(i) Let $\ell \in \mathbb{N}_0$ and $g_p^\star = g_p^{(\ell)}$, $g_n^\star = g_n^{(\ell)}$, $V = V^{(\ell)}$, $\overline{T}_n = T_n^{(\ell)}$, $T_L = T_L^{(\ell)}$.

(ii) **repeat**

(a) Set $V_n = V + U_n$ and find g_n in Ω_S such that

$$\begin{cases} -\operatorname{div} J_n + \sigma_1(g_p^\star, g_n^\star, \triangle t) g_n = f_1(g_p^\star, g_n^\star, \triangle t, \widetilde{g}_n), \\ J_n = \nabla g_n - \nabla V_n \overline{T}_n^{-1} g_n, \\ g_n + \theta_n^{-1} J_n \cdot \nu(x) = g_{1,a} \qquad \text{on } \Gamma_C; \end{cases}$$

(b) Set $V_p = V + U_p$ and find g_p in Ω_S such that

$$\begin{cases} -\operatorname{div} J_p + \sigma_p(g_p^\star, g_n^\star, \triangle t) g_n = f_p(g_p^\star, g_n^\star, \Delta t, \widetilde{g}_p), \\ J_p = -\nabla g_p - \nabla V_p T_L^{-1} g_p, \\ g_p - \theta_p^{-1} J_p \cdot \nu(x) = g_{p,a} \qquad \text{on } \Gamma_C; \end{cases}$$

(c) Set $n = \mu_n^{-1} g_n$, $p = \mu_p^{-1} g_p$ and $V_1 = V + \delta V$, where δV solves in Ω_S

$$\begin{cases} \lambda^2 \Delta(\delta V) - (p+n)\delta V = -\lambda^2 \Delta V + n - p - C, \\ \delta V = 0 \qquad \text{on } \Gamma_C; \end{cases}$$

(d) Set $g_n^\star := g_n, g_p^\star := g_p$, and $V := V_1$;

until $\|\delta V\|_2 < \min(tol_{\text{int}}, d_1(\delta T)^{d_2})$, *with* δT *from step* (iv);

(iii) Set $V_n = V + U_n$ and find g_w in Ω_S such that

$$\begin{cases} -\operatorname{div} J_w + \sigma_2(g_p^\star, g_n^\star, \triangle t) g_w = f_2(g_p^\star, g_n^\star, \Delta t, \widetilde{g}_w), \\ J_w = \nabla g_w - \nabla V_n \overline{T}_n^{-1} g_w, \\ \nabla g_w \cdot \nu - \theta_n(g_{w,a} - g_w) = \frac{3}{2}\theta_n g_{n,a}(\overline{T}_n - T_a) + \frac{3}{2} g_n \nabla V \cdot \nu(x) \quad \text{on } \Gamma_C \end{cases}$$

(iv) Compute $\overline{T}_n = 2g_w/3g_n$ and $\delta T = \|\overline{T}_n - \widetilde{T}_n\|_2$.

(v) Define $V^{(\ell+1)} = V + \delta V$, where δV is the solution of (ii.c).

(vi) Find T_L in Ω_S such that

$$\begin{cases} -\operatorname{div}(\kappa_L \nabla T_L) + \sigma_L(g_n, g_p, \triangle t) T_L = f_L(g_n, g_p, V, \triangle t, \widetilde{T}_L), \\ -\kappa_L \nabla T_L = \nu \cdot \frac{T_L - T_{\text{env}}}{R_{\text{th}}} \qquad \text{on } \Gamma_C \end{cases}$$

(vii) Set $\mu_n = \mu_{n,0}\big(\frac{T_0}{T_L}\big)^{\alpha_n - 1}$ and $\mu_p = \mu_{p,0}\big(\frac{T_0}{T_L}\big)^{\alpha_p - 1}$

(viii) Set $g_n^{(\ell+1)} := g_n$, $g_w^{(\ell+1)} := g_w$, $g_p^{(\ell+1)} := g_p$, $T_n^{(\ell+1)} := \overline{T}_n$ and $T_L^{(\ell)} := T_L$.

until *convergence*;

contradict the temperature dependency given in (3.12) (notice that $T_0 = 1$ in the scaled formulation). We remark that the difference between these expressions is incorporated in the drift-diffusion formulation of the problem, see (5.3).

7.4 Coupled network-device system

To make use of the iterative algorithms described above, also in the coupled network-device system, it is necessary to consider iterative algorithms. The proper iteration of arbitrary circuit-device systems is far from being trivial and the development of proper iterative solvers for large circuit-device systems builds an own field of research.

Algorithm 6 : Gauß-Seidel iteration for coupled systems

Start with values from former time step
$e = \widetilde{e}$, $\hat{\boldsymbol{T}} = \widetilde{\hat{\boldsymbol{T}}}$, $\boldsymbol{T}^d = \widetilde{\boldsymbol{T}}^d$, $T_L = \widetilde{T}_L$, $j_S = \widetilde{j}_S$, $J_{\text{th}} = \widetilde{J}_{\text{th}}$,
repeat

(i) Solve device equation using iterative scheme from above
$[T_L, j_S, J_{\text{th}}] = \text{solve\_device\_equation}(e, T_L, \hat{\boldsymbol{T}}, \boldsymbol{T}^d, \triangle t)$

(ii) Solve electric network equations with Newton method
$e = \text{solve\_MNA\_equations}(e, j_S, \hat{\boldsymbol{T}}, \boldsymbol{T}^d, \triangle t)$

(iii) Solve thermal network equations
$[\hat{\boldsymbol{T}}, \boldsymbol{T}^d] = \text{solve\_thermal\_network}(e, T_L, J_{\text{th}}, \triangle t)$

until *convergence*;

For the coupled device-circuit systems considered in this work, we applied a Gauß-Seidel-type iteration. We alternately solve the electric network, thermal network and device equations. The scheme is roughly described in Algorithm 6. We stop the iteration procedure, as in the previous section, when the relative difference of two consecutive iterations of the discrete coupling values $(e, \hat{\boldsymbol{T}}, \boldsymbol{T}^d, T_L, j_S, J_{\text{th}})$ is smaller than the given tolerance *tol*. In all considered simulations we applied a value of $tol = 10^{-6}$.

For notational convenience, we only mention the values that contribute to the coupling of the different subsystems. We notice, that the device and the electric network equations are coupled via the node potentials e and the semiconductor current j_S according to (4.7) and (4.8) (or § 5.4 for the scaled model). Moreover the device and the thermal network equations are coupled according to § 4.2 (for the scaled model see also § 5.4) via the lattice temperature T_L and the temperature values in the lumped and distributed thermal network elements $\hat{\boldsymbol{T}}$ and $\boldsymbol{T}^d$, respectively. Finally the thermal and electric network equations are coupled on the one hand via the Joule heat production term (4.21) dependent on the current through the resistors, that

can be expressed in terms of the node potentials e (see (1.1)). On the other hand the electric and thermal network equations are coupled via the temperature in the resistors according to (4.18), given as the temperature in the corresponding lumped or distributed thermal element. We remark that in our model we only consider semiconductor devices and resistors as thermally relevant elements of the circuits. In case of considering further elements as thermally relevant, the coupling between electric and thermal network extends to those elements as well.

For much larger circuit-device system than the systems considered in this work a more advanced iteration technique will be required, like damped iterative schemes, for instance.

Chapter 8

Numerical examples

In this chapter we will present numerical examples clarifying the importance of the consideration of thermal effects in semiconductor devices and moreover in electric circuits. Firstly, we take into account the thermal effects by means of the energy-transport model what corresponds to taking into account the thermal energy of charge carriers. We will present examples showing the magnitude of thermal effects in *pn* diodes modeled by the energy transport model. Moreover, we will give a numerical discussion for the choice of boundary conditions as discussed in § 3.2.1. We will compare the results for the energy-transport equations with Dirichlet and Robin-type boundary conditions.

Additionally, we will present an example for the coupling of the energy-transport equations for devices with the MNA-equations for electric networks in order to include thermal effects of charge carriers into the simulation of electric circuits. We will compare our results to those achieved by the coupling of drift-diffusion equations and MNA-equations for the coupled network-device system as presented in [**99**].

In further examples we employ for the first time the energy-transport model to optoelectronic devices like laser- and photo diodes and show the influence of the thermal effects onto the signal output of those devices. We will present an example for an optoelectronic device-network system, showing that the thermal effects of the charge carriers in the device influence the electric behavior of the entire circuit.

In a second step we will extend the thermal simulation of devices by including non-isothermal modeling of the lattice temperature as presented in § 3.4. We will present the influence of lattice heating onto the electrical behavior of ballistic diodes and *pn* diodes. We will show the dependency of the lattice temperature on the choice of boundary conditions by employing Dirichlet as well as Robin-type boundary conditions.

In a last step we will consider numerical examples for the complete electro-thermal network-device coupling where besides particle and lattice

heating the thermal interaction between the circuit elements is taken into account.

8.1 Energy-Transport model with different boundary conditions

A *pn* diode with time-dependent voltage

Parameter	Physical meaning	Numerical value
L_y	extension of device in y-direction	$6 \cdot 10^{-7}\,\mathrm{m}$
L_z	extension in z-direction	$10^{-6}\,\mathrm{m}$
q	elementary charge	$1.6 \cdot 10^{-19}\,\mathrm{As}$
ϵ_s	permittivity constant	$10^{-12}\,\mathrm{As/Vcm}$
U_T	thermal voltage at $T_L = 300K$	$0.026\,\mathrm{V}$
μ_n/μ_p	low-field carrier mobilities	$1500/450\,\mathrm{cm}^2/\mathrm{Vs}$
τ_n/τ_p	carrier lifetimes	$10^{-6}/10^{-5}\,\mathrm{s}$
n_i	intrinsic density	$10^{16}\,\mathrm{m}^{-3}$
τ_0	energy relaxation time	$4 \cdot 10^{-13}\,\mathrm{s}$

Table 8.1: Physical parameters for a silicon *pn* diode.

As first example we consider a silicon *pn* diode with a time-dependent voltage source. The diode is assumed to be homogeneous in the y- and the z-direction such that a one-dimensional approach is suitable. The diode is modeled by the scaled energy-transport equations in drift-diffusion formulation (5.4)-(5.8). In order to unscale the current densities and to obtain a current (and not a current density), the size of the diode in the y- and z-direction is specified (see Table 8.1). The quasi one-dimensional diode consists of a p-doped region with length $L/2$ and minimum doping profile $-C_m$ and of a n-doped region with the same length and with a maximum doping of C_m. We have used the values $L = 0.1\,\mu\mathrm{m}$ or $L = 0.6\,\mu\mathrm{m}$ and $C_m = 10^{22}\,\mathrm{m}^{-3}$ or $C_m = 5 \cdot 10^{23}\,\mathrm{m}^{-3}$, respectively. The doping profile is slightly smoothed using the tanh function (see, e.g. [**57**]). The circuit operates with 1 GHz, i.e., the applied voltage equals $v(t) = V_0 \sin(2\pi\omega t)$ with maximum voltage $V_0 = 1.5\,\mathrm{V}$ and frequency $\omega = 10^9\,\mathrm{Hz}$. The physical parameters are collected in Table 8.1. We refer to [**86**] for more details about carrier life-times

We have used a uniform spatial grid with 101 nodes and a uniform time step $\triangle t = 10^{-13}\,\mathrm{s}$. The time step is rather small; this can be explained by the fact that we need careful computations at the switching point when the voltage changes from forward to backward bias and vice versa. An adaptive time stepping procedure would certainly allow to choose larger time steps;

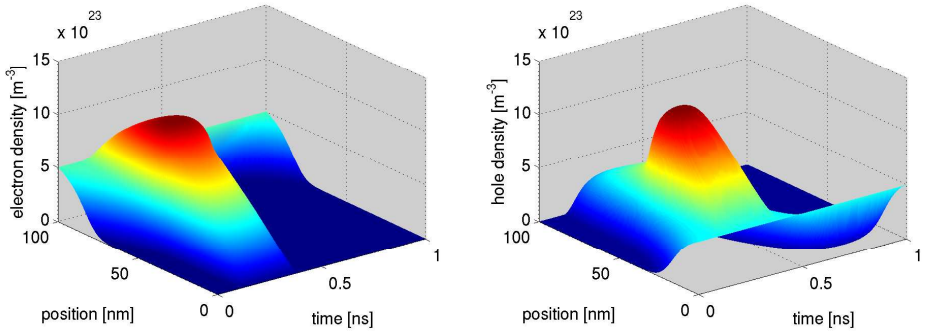

Figure 8.1: Electron (left) and hole (right) concentration in a *pn* diode with length $L = 0.1\mu$m and maximum doping concentration $C_m = 5 \cdot 10^{23}$ m^{-3} for a sinusoidal input signal $v(t) = 1.5\ \sin(2\pi 10^9 Hzt)$V.

we plan to implement this in the future.

Initially, the semiconductor device is assumed to be in thermal equilibrium, i.e., the total current of electrons and holes vanishes. Thus, the initial current densities are taken to be zero. The initial displacement current is then defined by $j_{d,S}(\cdot,0) = \lambda^2(V_{\text{eq}})_x$, where V_{eq} denotes the thermal equilibrium potential given by (7.1). The definition of $j_{d,S}$ ensures that equation (5.9) is fulfilled. Summarizing, the initial conditions read as follows:

$$\begin{aligned} &V = V_{\text{eq}}, && T_n = 1, && j_S = 0, && j_{d,S} = \lambda^2(V_{\text{eq}})_x, \\ &g_n = \mu_n n_{\text{eq}}, && g_w = \tfrac{3}{2}\mu_n n_{\text{eq}}, && g_p = \mu_p p_{\text{eq}}, \end{aligned} \tag{8.1}$$

where $n_{\text{eq}} = n_i e^{V_{\text{eq}}}$ and $p_{\text{eq}} = n_i e^{-V_{\text{eq}}}$ are the thermal equilibrium particle densities.

At the contacts Γ_C for the first computations we employ Dirichlet boundary conditions for g_n, g_w, g_p, T_n and V. This is

$$g_n = \mu_n n_a, \quad g_w = \frac{3}{2}\mu_n n_a, \quad g_p = \mu_p p_a, \quad T_n = 1, \quad V = V_{\text{ap}} + V_{\text{bi}},$$

with n_a, p_a given in (3.18) and $V_{\text{bi}} = \operatorname{arcsinh}\left(\frac{C}{2n_i}\right)$. We notice that in the one-dimensional model $\Gamma_C = \{0,1\}$ and $\Gamma_I = \emptyset$. For more-dimensional simulation see (3.14) for the boundary conditions on Γ_I.

In Figure 8.1 we present the particle densities in the 100 nm *pn* diode with a maximum doping of $C_m = 5 \cdot 10^{23}$ m^{-3} during one oscillation of the voltage source. We observe the expected behavior that for forward bias the device is full of charge carriers. For backward bias we observe a depletion region that due to the smallness of the device covers almost the entire device.

In Figure 8.2 we present the thermal energy density in *pn* diodes with different size L and different maximum doping concentrations C_m. We observe that a higher doping profile gives a larger energy density as it provides

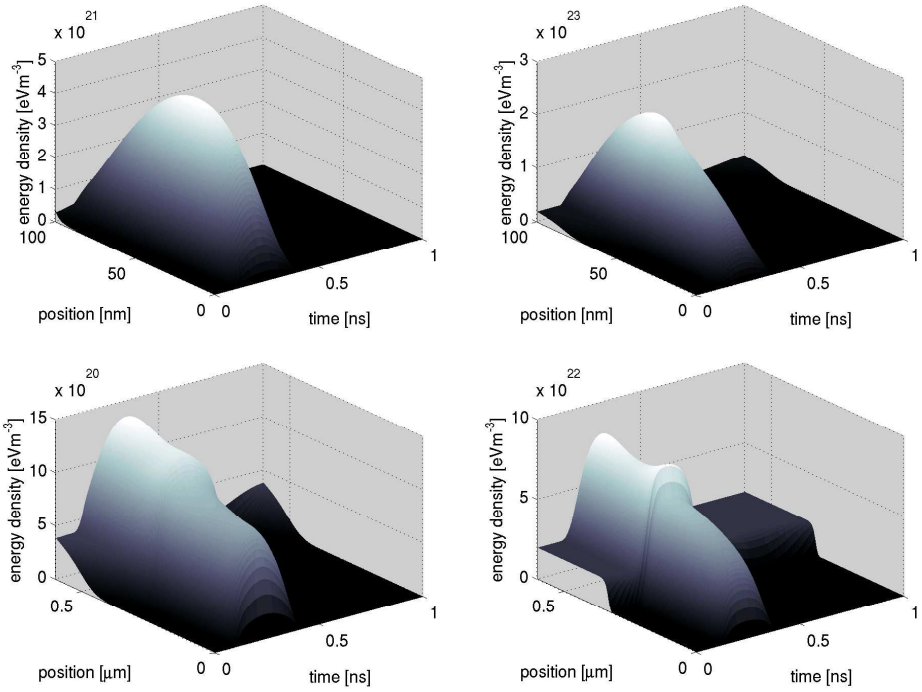

Figure 8.2: Energy density in a *pn* diode with lengths $L = 0.1\mu$m (upper row), $L = 0.6\mu$m (lower row) and maximum doping concentrations $C_m = 10^{22}$ m^{-3} (left column), $C_m = 5 \cdot 10^{23}$ m^{-3} (right column) for the sinusoidal input signal.

more (high-energetic) electrons in the device. The energy density also increases for smaller devices. This coincides with the experience that smaller devices heat up stronger than larger ones.

The electron temperature can be considered as the average thermal energy per electron. The corresponding electron temperature for the devices with $C_m = 5{\cdot}10^{23}\text{m}^{-3}$ during the oscillation of the voltage source is depicted in Figure 8.3. In the 600 nm device we observe an increase in the forward biased diode up to 873 K, in the 100 nm device the electrons heat up in the forward biased case up to 2509 K. For reverse bias the electron temperature increases even more. However, as for reverse bias the device is depleted and only few charge carriers are in the device, the high electron temperature does not contribute to a high thermal energy in the device (comp. Figure 8.2) and the thermal effects are not of high interest. Moreover, in Figure 8.3 (left) we observe a strong boundary layer for the temperature for forward bias at the p-doped contact corresponding to $x = 0$.

This boundary layer also occurs in the 600 nm device with $C_m = 10^{22}$ m^{-3} as we can see in Figure 8.4. There the temperature is depicted at various

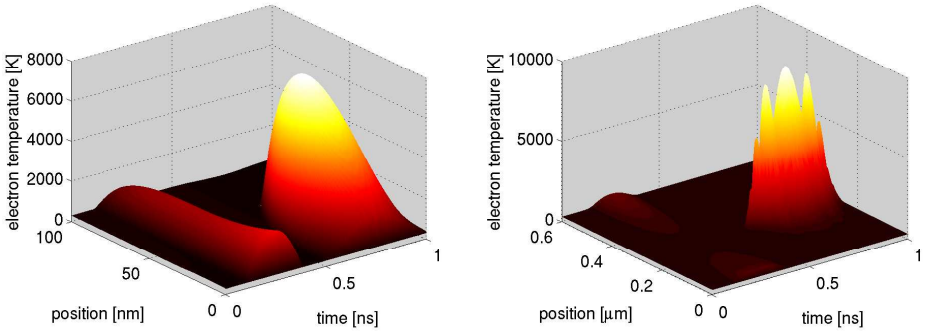

Figure 8.3: Electron temperature in a *pn* diode with lengths $L = 0.1\mu$m (left), $L = 0.6\mu$m (right) and maximum doping concentration $C_m = 5 \cdot 10^{23}$ m^{-3} for a sinusoidal input signal.

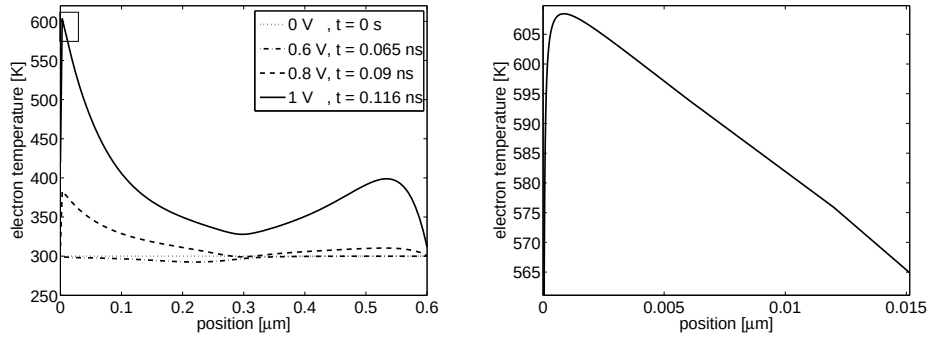

Figure 8.4: Left: Electron temperature in a $0.6\,\mu$m diode with maximum doping level of $10^{22}\,\mathrm{m}^{-3}$ for different times t and corresponding voltages $v(t)$. Right: Zoom for the bias $v(t) = 1\,\mathrm{V}$.

times t_i (and corresponding voltages $v(t_i)$). We observe hot electrons in the n-region and close to the p-doped terminal. At the junction, cooling effects occur for moderate applied voltages. This thermoelectric effect is well known in *pn* diodes and it has important implications for the device design in which heat management is needed (see, for instance, [**77**]).

At the left p-doped terminal, we observe the boundary layer which can be resolved only in very high resolution (see Figure 8.4 (right)). In fact, there are boundary layers also for the electron density n as well as for the energy density $w = \frac{3}{2}nT_n$ (Figure 8.5 (left)). This seems to indicate that the use of Dirichlet boundary conditions for n and w (or, equivalently, for n and T_n) is not appropriate.

Therefore in a second step we apply the boundary conditions of Robin-type (3.20)-(3.22). The scaled version of the boundary conditions is given in (5.10)-(5.11). These Robin-type boundary conditions for g_n, g_w and g_p

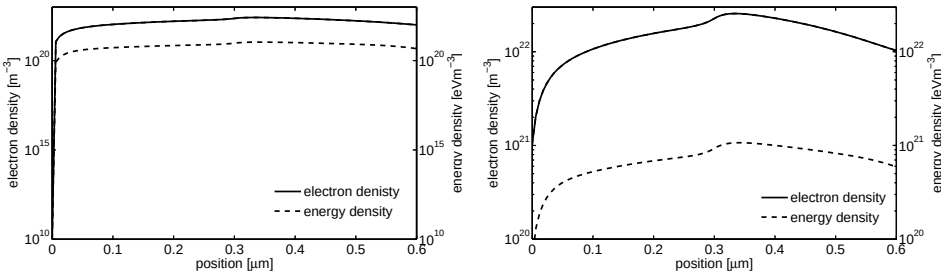

Figure 8.5: Electron and energy density in a pn diode with length $L = 0.6\mu$m with maximum doping level of $10^{22}\,\mathrm{m}^{-3}$ for the bias $v(t) = 1\,\mathrm{V}$. With Dirichlet boundary conditions for n, w, T (left) and with Robin boundary conditions with $\theta_n = 25$ (right).

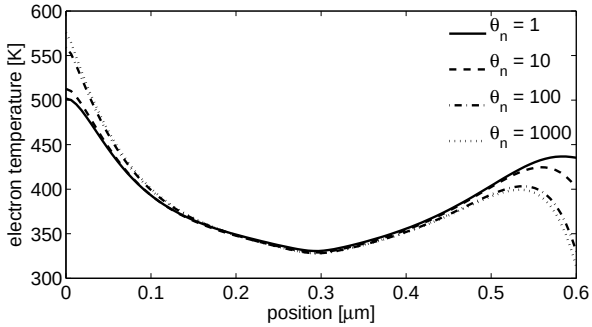

Figure 8.6: Electron temperature in a pn diode with length $L = 0.6\mu$m with maximum doping level of $C_m = 10^{22}\,\mathrm{m}^{-3}$ for the bias $v(t) = 1\,\mathrm{V}$ with different boundary condition parameters θ_n.

interpolate between Dirichlet and Neumann conditions. Clearly, a derivation of suitable higher-order boundary conditions from the Boltzmann equation in the energy-transport context would be necessary, but we postpone such an analysis to a future work. Furthermore, the boundary condition for the temperature should be compatible with the principle of local energy balance [**100**]. We do not analyze this property since we are more interested in the numerical solution of the coupled system of PDAEs.

Thanks to the new boundary conditions, the boundary layers for n and w disappear for an appropriate choice of the parameter θ_n (Figure 8.5 (right)). The dependency of the electron temperature T_n on this parameter is shown in Figure 8.6. These results indicate that the choice of the Robin-parameter is crucial for the temperature profile at the boundary. On the other hand, it can be observed that the current values are almost independent of the choice of θ_n and θ_p.

8.2 Electric network-device coupling for a rectifier circuit

Rectifying circuit

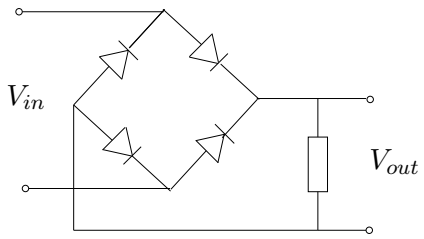

Figure 8.7: Rectifying circuit.

The second example is concerned with a rectifying circuit containing four *pn* silicon diodes (Figure 8.7). Each of the diodes has the length $L = 0.1\,\mu$m (and $L_y = 0.1\,\mu$m, $L_z = 2\,\mu$m) or $L = 1\,\mu$m (and $L_y = 1\,\mu$m, $L_z = 20\,\mu$m) and a maximum doping of $10^{22}\,\mathrm{m}^{-3}$. The remaining physical parameters are listed in Table 8.1. The resistance in the circuit equals $R = 100\,\Omega$ and the voltage source is given by $v(t) = V_0 \sin(2\pi\omega t)$ with $V_0 = 5\,\mathrm{V}$ and $\omega = 1\,\mathrm{GHz}$ or $\omega = 10\,\mathrm{GHz}$. As initial conditions we assume thermal equilibrium for each diode as described in the previous section. For the circuit variables we assume the node potentials e as well as the current through the voltage source i_v to be zero:

$$e = 0, \quad i_v = 0. \tag{8.2}$$

For the coupled network-device problems we mentioned that the determination of initial values is not arbitrary as the system is of differential algebraic character. Thus we have to ensure a consistent initialization. The determination of consistent initial values is not a trivial task. Lamour presented a `MATLAB`® source code that allows to compute consistent initial values from an appropriate initial guess for DAEs with an (tractability) index up to two (see, e.g.[**62, 63**]). As guess for the initial values we start with the semiconductor devices in thermal equilibrium. Moreover, we assume the node potentials and the current in the circuit to be zero, see (8.2), and the displacement current to fulfill (5.9), i.e. $j_{S,d}(\cdot, 0) = -\lambda^2 (V_{\mathrm{eq}})_x$. Furthermore, the temperature of all thermally relevant devices we assumed to coincide with the scaled temperature $T_0 = 1$. A computation according to [**63**] showed that this choice is already numerically consistent.

For the diodes in the Graetz circuit, we may employ Dirichlet or Robin boundary conditions as these conditions affect the behavior of the temperature on the boundary but less the current values. Only the profile of the

h/L	$RE(n)$	$RE(w)$	$RE(p)$	$RE(V)$	$RE(T_n)$	$RE(j_S)$	$RE(circ)$
0.04	$8.7 \cdot 10^{-2}$	$1.3 \cdot 10^{-1}$	$6.8 \cdot 10^{-2}$	$2.3 \cdot 10^{-2}$	$1.0 \cdot 10^{-1}$	$1.1 \cdot 10^{-1}$	$1.5 \cdot 10^{-2}$
0.02	$3.5 \cdot 10^{-2}$	$5.3 \cdot 10^{-2}$	$2.7 \cdot 10^{-2}$	$1.2 \cdot 10^{-2}$	$7.3 \cdot 10^{-2}$	$5.0 \cdot 10^{-2}$	$6.9 \cdot 10^{-3}$
0.01	$1.1 \cdot 10^{-2}$	$1.7 \cdot 10^{-2}$	$8.0 \cdot 10^{-3}$	$4.1 \cdot 10^{-3}$	$4.7 \cdot 10^{-2}$	$1.7 \cdot 10^{-2}$	$2.3 \cdot 10^{-3}$
0.005	$2.4 \cdot 10^{-3}$	$3.9 \cdot 10^{-3}$	$1.8 \cdot 10^{-3}$	$1.1 \cdot 10^{-3}$	$2.3 \cdot 10^{-2}$	$4.1 \cdot 10^{-3}$	$5.7 \cdot 10^{-4}$
rate	1.73	1.67	1.75	1.47	0.72	1.60	1.59

Table 8.2: Relative error (RE) for different space step sizes. The time step size is $\triangle t = 10^{-12} s$.

$\triangle t$	$RE(n)$	$RE(\epsilon)$	$RE(p)$	$RE(V)$	$RE(T_n)$	$RE(j_S)$	$RE(circ)$
10	$2.0 \cdot 10^{-3}$	$1.6 \cdot 10^{-3}$	$1.9 \cdot 10^{-3}$	$6.0 \cdot 10^{-4}$	$5.6 \cdot 10^{-3}$	$2.1 \cdot 10^{-3}$	$3.6 \cdot 10^{-4}$
8	$1.5 \cdot 10^{-3}$	$1.1 \cdot 10^{-3}$	$1.4 \cdot 10^{-3}$	$5.2 \cdot 10^{-4}$	$4.5 \cdot 10^{-3}$	$1.6 \cdot 10^{-3}$	$3.0 \cdot 10^{-4}$
5	$7.3 \cdot 10^{-4}$	$5.7 \cdot 10^{-4}$	$6.8 \cdot 10^{-4}$	$3.5 \cdot 10^{-4}$	$2.8 \cdot 10^{-3}$	$1.5 \cdot 10^{-3}$	$2.2 \cdot 10^{-4}$
4	$5.5 \cdot 10^{-4}$	$4.1 \cdot 10^{-4}$	$5.1 \cdot 10^{-4}$	$3.1 \cdot 10^{-4}$	$2.7 \cdot 10^{-3}$	$1.4 \cdot 10^{-3}$	$1.8 \cdot 10^{-4}$
rate	1.38	1.51	1.41	0.66	0.76	0.56	0.74

Table 8.3: Relative error (RE) for different time step sizes. The space step size is $h = 0.0025L$; $\triangle t$ is measured in units of 10^{-13} s.

electron density changes slightly. Here, for simplicity, we have employed Robin conditions with a value of $\theta_n = \theta_p = 2500$.

The numerical simulations are performed on a uniform grid with 51 nodes for each diode. For simplification, we employed the constant time step 0.5 ps. This time step is needed for accurate computations for the diodes at reverse bias and at the switching point. The implementation of an adaptive time-stepping would generally allow to choose much larger time steps.

The numerical convergence is tested on a numerical solution on a fine grid with 401 nodes and time step $\triangle t = 5 \cdot 10^{-14}$ s. The reference solution simulates the circuit during one oscillation in the time interval $[0, 10^{-10}\,\text{s}]$. In Tables 8.2 and 8.3 the relative errors of the discrete values with respect to the Euclidean norm and the numerical convergence orders are depicted. Recall that $w = \frac{3}{2} n T_n$ denotes the thermal energy. The relative error *RE(circ)* of the circuit is the Euclidean error of the discrete node potentials and branch current.

The spatial convergence orders for the densities and the temperature are slightly smaller than those obtained for the energy-transport equations [**34**] for single devices which shows that the coupling to the circuit equations plays an important role. The temperature T_n is obtained from the electron density n and the energy density w by averaging the quantity $T_n = 2w/3n$, which may explain the rather low convergence order of T_n. The temporal convergence orders are smaller than those with respect to space discretization, probably due to the coupling.

In Figure 8.8 the energy density in one of the diodes during one oscillation of the circuit for two different device sizes and frequencies is presented. Here, we observe that the energy density for both cases is in the same order

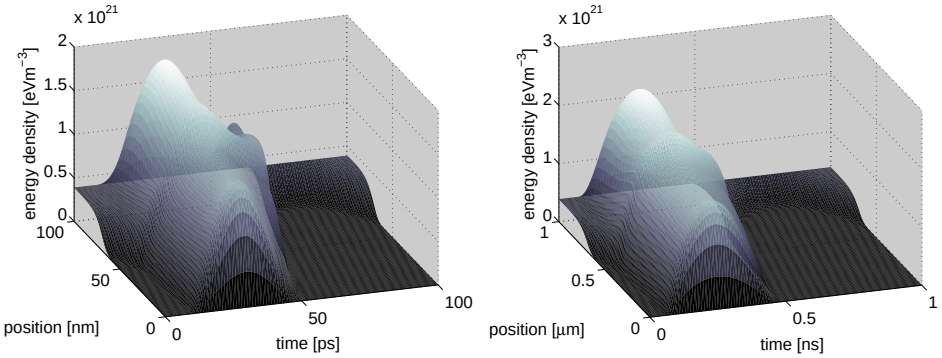

Figure 8.8: Energy density in a *pn* diode with size $L = 0.1\,\mu$m and frequency 10 GHz (left); $L = 1\,\mu$m and frequency 1 GHz (right).The maximum doping is $C_m = 10^{22}\,\mathrm{m}^{-3}$.

of magnitude and is slightly higher in the larger device. The (ten times) smaller device was driven with a (ten times) shorter signal. Thus we observe that in smaller devices the charge carriers heat up significantly faster. This coincides with the observation from the first example, where the thermal energy density in smaller devices, for devices driven by the same signal, was significantly higher (comp. Figure 8.2).

Next, we investigate the behavior of the current through one diode and through the circuit using the transient or stationary energy-transport equations (ET) and the transient drift-diffusion model (DD). Figure 8.9 shows the current from simulations of a $1\,\mu$m diode in a 1 GHz circuit. The figure clearly shows the rectifying behavior of the circuit. The largest current is obtained from the drift-diffusion model since we have assumed a constant electron mobility such that the drift is unbounded with respect to the modulus of the electric field. The stationary energy-transport model is not able to catch the capacitive effect at the junction. Similar statements hold for the output signal of the circuit.

Finally, we consider a Graetz circuit with a larger frequency of 10 GHz and smaller device size of $0.1\,\mu$m. The current through one of the diodes of the circuit and the output signal of the circuit is presented in Figure 8.10. Here, the differences between the three models are more pronounced. Clearly, the capacitive effect is larger for this rather high frequency. As in the previous example, the stationary model cannot capture this effect. Moreover, we observe a slight time shift between the stationary and the transient energy-transport equations.

With the examples in this section we have presented for the first time the numerical coupling of the transient energy-transport model for semiconductor devices with circuit equations from modified nodal analysis, leading to a system of partial differential-algebraic equations. The numerical com-

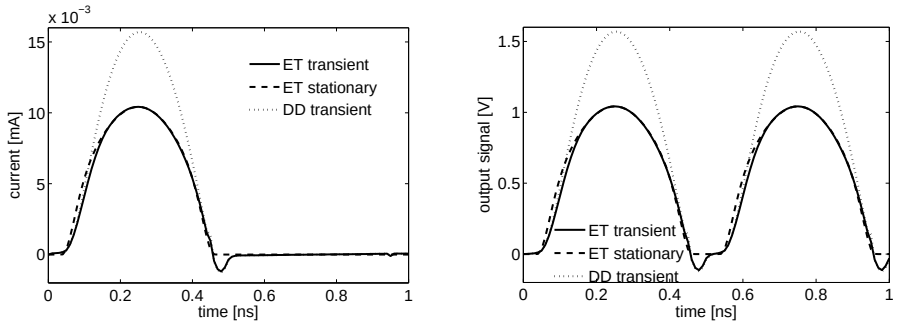

Figure 8.9: Left: Current through a 1 μm diode in a 1 GHz circuit. Right: Output signal of the circuit.

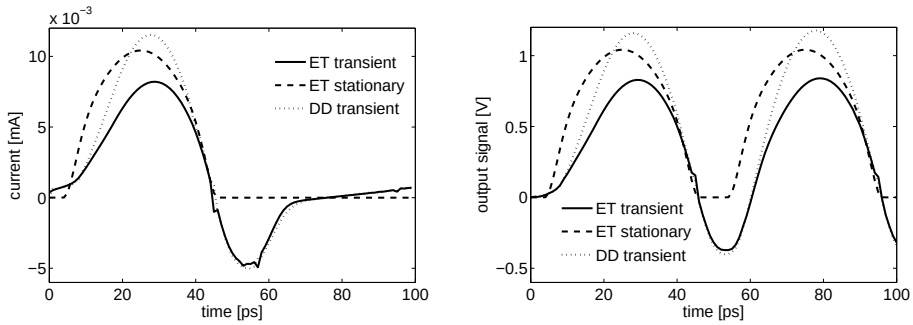

Figure 8.10: Left: Current through a 100 nm diode in a 10 GHz circuit. Right: Output signal of the circuit.

parison with the coupled system of the drift-diffusion and network equations shows the strong influence of the carrier heating on the current density. In some physical situations, the stationary energy-transport model seems to provide reasonable results, compared to the other two models. However, in high-frequency circuits, the use of the transient model seems to be necessary.

We have also compared the effect of the boundary conditions for the device. Boundary layers which appear when standard Dirichlet conditions for the particle density and energy density are employed disappear if appropriate Robin boundary conditions for these variables are used.

8.3 Optoelectronic network-device coupling

In the next example we present the numerical coupling of optoelectronic device models described in § 3.3 with the electric network equations described in § 1. As in this work we present the model and simulation of optoelectronic devices based on the energy-transport equations for the first time, we firstly present the results of the single device simulation.

Parameter	Physical meaning	Numerical value
L_y	extension of the device in y-direction	$10^{-6}\,\mathrm{m}$
L_z	extension in z-direction	$10^{-5}\,\mathrm{m}$
q	elementary charge	$1.6 \cdot 10^{-19}\,\mathrm{As}$
U_T	thermal voltage at 300 K	$0.026\,\mathrm{V}$
$U_{n,0}/U_{p,0}$	band potentials in active region	$0.1/-0.1\,\mathrm{V}$
C_n/C_p	Auger recombination parameters[**65**]	$10^{-43}/10^{-42}\,\mathrm{m^6 s^{-1}}$
B	spontaneous recombination parameter[**2**]	$10^{-16}\,\mathrm{m^3 s^{-1}}$
τ_n/τ_p	carrier lifetimes[**65**]	$10^{-6}/10^{-5}\,\mathrm{s}$
τ_0	energy relaxation time[**34**]	$4 \cdot 10^{-13}\,\mathrm{s}$
n_{th}	threshold density[**2**]	$10^{24}\,\mathrm{m^{-3}}$
α_{bg}	optical background loss[**2**]	$4000\,\mathrm{m^{-1}}$
α_f	facet loss[**2**]	$5000\,\mathrm{m^{-1}}$
ϵ_0	permittivity constant[**65**]	$8.85 \cdot 10^{-12}\,\mathrm{As(Vm)^{-1}}$
$\epsilon_s^A/\epsilon_s^G$	material permittivity[**65**]	$12.1 \cdot \epsilon_0/12.9 \cdot \epsilon_0$
μ_n^A/μ_n^G	electron mobilities[**65**]	$2300/8300\,\mathrm{cm^2(Vs)^{-1}}$
μ_p^A/μ_p^G	hole mobilities[**65**]	$145/400\,\mathrm{cm^2(Vs)^{-1}}$
$\mu_{\mathrm{opt}}^A/\mu_{\mathrm{opt}}^G$	refractive index[**65**]	3.3/3.15
n_i^A/n_i^G	intrinsic density[**65**]	$2.1 \cdot 10^9/2.1 \cdot 10^{12}\,\mathrm{m^{-3}}$
g_0^G	differential gain in GaAs (see [**2, 28**])	$3 \cdot 10^{-21}\,\mathrm{m^2}$
ω	angular frequency (wave length 870 nm)	$2.17 \cdot 10^{-15}\,\mathrm{Hz}$

Table 8.4: Physical parameters for a laser diode of $Al_{0.7}Ga_{0.3}As$ and GaAs. The parameters with superscript A denote the values for $Al_{0.7}Ga_{0.3}As$, and those with superscript G denote the values for GaAs. The parameters without superscript are valid for both materials.

Laser diode

The complete scaled model for a laser diode is presented on page 60 and consists of the energy-transport equations for the electrons, the drift-diffusion equations for the holes, the Poisson equation for the electric potential coupled to the waveguide equation for the optical field intensity and the rate equation for the number of photons in the device to cover the optical effects.

We consider a $GaAs/Al_{0.7}Ga_{0.3}As$ p-i-n laser diode under various bias conditions. The one-dimensional diode has the length $1\,\mu$m consisting of a p-doped part with length $0.45\,\mu$m, a low-doped (intrinsic) part with length $0.1\,\mu$m, and an n-doped region with length $0.45\,\mu$m. The doping concentrations are $-10^{24}\,\mathrm{m^{-3}}$ in the p-doped, $10^{18}\,\mathrm{m^{-3}}$ in the low-doped region, and $10^{24}\,\mathrm{m^{-3}}$ in the n-doped part. The doping profile is slightly smoothed by use of the tanh function [**57**]. The band potentials, consisting of the constant values $U_{n,0}$, $U_{p,0}$, respectively, in the active region and zero elsewhere, are also slightly smoothed. The values for $U_{n,0}$ and $U_{p,0}$ are rough approximations according to the contact potential computations in [**31**]. The remaining physical parameters for the diode are collected in Table 8.4. For the computations we have employed a uniform spatial grid with 101 nodes

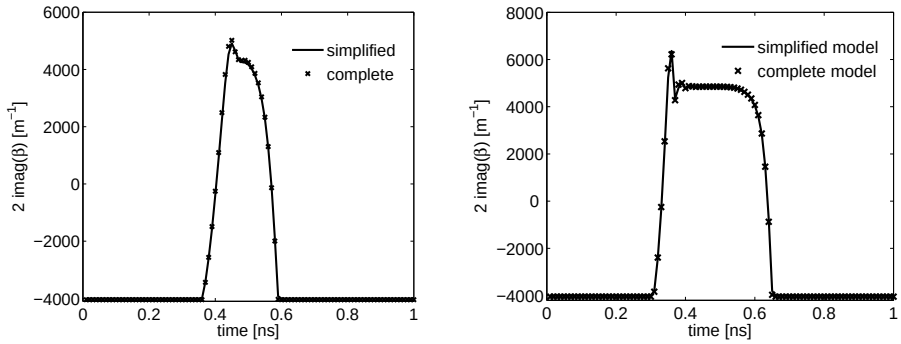

Figure 8.11: Laser diode biased with a sinusoidal signal $V_0 \sin(2\pi 10^9\,\mathrm{Hz}\,t)$. Comparison of the modal gain $2\mathrm{Imag}(\beta)$ during one oscillation computed from the complete and the simplified model with applied bias of $V_0 = 2\,\mathrm{V}$ (left) and $V_0 = 3\,\mathrm{V}$ (right).

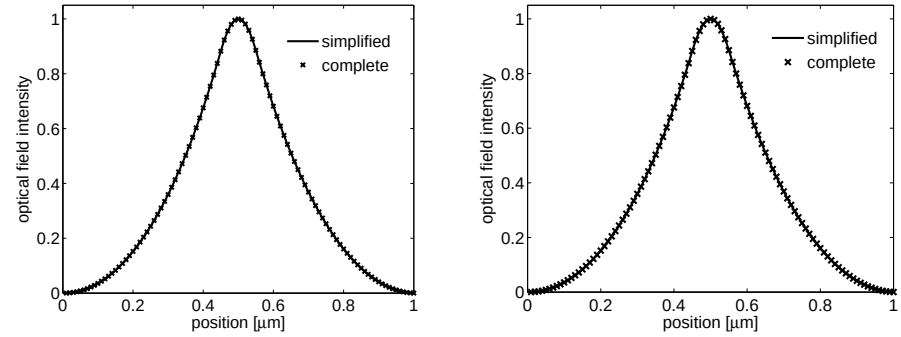

Figure 8.12: Laser diode biased with a sinusoidal signal $V_0 \sin(2\pi 10^9\,\mathrm{Hz}\,t)$. Intensity distribution of the optical field at the maximum bias of $V_0 = 2\,\mathrm{V}$ (left) and $V_0 = 3\,\mathrm{V}$ (right).

and a time step size of 1 ps.

First we consider the response of the laser diode to various voltage signals computed with the complete model including the waveguide equation (3.27) and compare the results to the simplified model in which the effective index approximation has been applied, see (3.30). For the transient simulations, we assume that the device is initially in thermal equilibrium without any optical field. The initial conditions are thus

$$g_n = \mu_n n_{\mathrm{eq}}, \quad g_w = \frac{3}{2}\mu_n n_{\mathrm{eq}}, \quad g_p = \mu_p p_{\mathrm{eq}}, \quad V = V_{\mathrm{eq}}, \quad T_n = 1, \quad S = 0$$

at time $t = 0$, where $n_{\mathrm{eq}}, p_{\mathrm{eq}}$ and V_{eq} represent the thermal equilibrium values (see § 3.2.2 or § 7.1).

The laser diode is biased with a sinusoidal signal $v(t) = V_0 \sin(2\pi\omega t)$

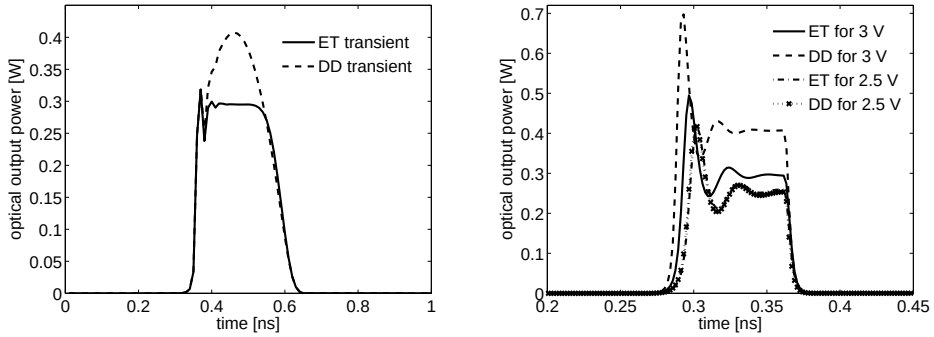

Figure 8.13: Response of the laser diode to the sinusoidal input signal $3\sin(2\pi 10^9\,\mathrm{Hz}\,t)\,\mathrm{V}$ (left) and to the digital input signal with frequency 5 GHz and duration 100 ps.

with amplitudes $V_0 = 2\,\mathrm{V}$ and $V_0 = 3\,\mathrm{V}$ and frequency $\omega = 1\,\mathrm{GHz}$. In Figure 8.11 the modal gain $2\mathrm{Im}(\beta)$ computed from (3.27) is compared with the approximation (3.30) during one oscillation of the input signal. The signal exceeds the threshold voltage for about $0.4\,\mathrm{ps} \le t \le 0.6\,\mathrm{ps}$. We see that the simplified model well approximates the modal gain, even for larger applied voltage. Below the threshold voltage, both modal gains coincide with the background loss. Figure 8.12 shows the intensity distribution $|\Xi|^2$ of the optical field at time $t = 5 \cdot 10^{-10}\,\mathrm{s}$. The approximated intensity distribution agrees very well with the intensity distribution computed from the complete model. These results motivate the use of the simplified model for the following simulations.

In Figure 8.13 the output signal is presented for various applied voltages and the (transient) drift-diffusion (DD) and energy-transport (ET) models. The left figure shows the optical output power from a sinusoidal signal with 1 GHz. The overshoot of the energy-transport model at about $t = 0.4\,\mathrm{ns}$ is caused by the transient response of the device. The differences between the drift-diffusion and energy-transport models become more significant at larger applied voltage as seen in the right figure for a digital signal. This is expected since the energy-transport equations include thermal effects.

Next, we present the steady characteristics of the laser diode (Figure 8.14). The left figure shows a current saturation in case of the energy-transport model. This behavior cannot be observed for the drift-diffusion model as the mobility μ_n is assumed to be constant and hence, the drift $-\mu_n V_x$ is unbounded in the electric field. When the relaxation time becomes smaller, the characteristics seem to converge to the curve of the drift-diffusion model. This can be understood from the fact that a vanishing relaxation time forces the particle temperature to relax to the constant lattice temperature. The power-current characteristics are shown in the right

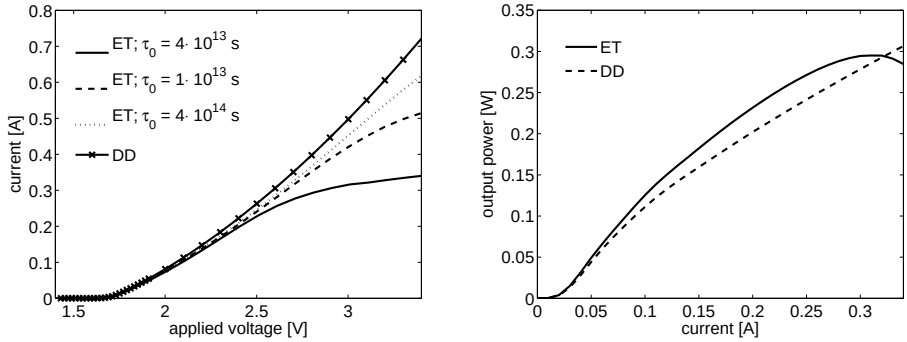

Figure 8.14: Characteristics of the laser diode using the drift-diffusion and energy-transport models with different relaxation times. Left: Current-voltage characteristics. Right: Power-current characteristics.

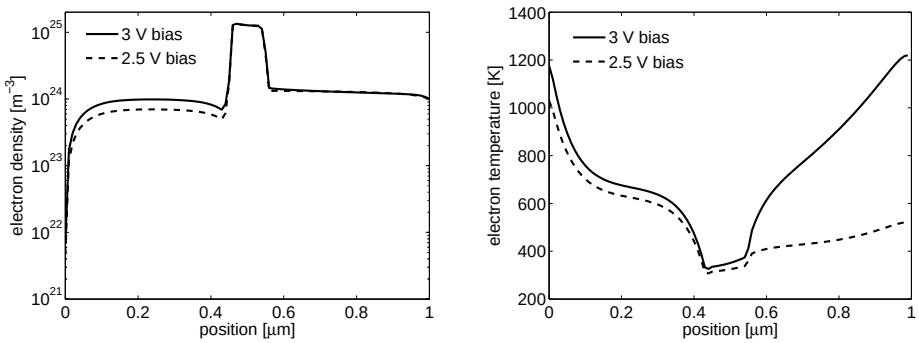

Figure 8.15: Electron density (left) and electron temperature (right) in the laser diode for different forward bias.

figure. For both models we observe the presence of a threshold current of about 8 mA and an approximate linear behavior for currents between 0.1 A and 0.3 A. The output power computed from the drift-diffusion model is linearly increasing even for larger currents. For the energy-transport model, however, the output power diminishes for large currents. A similar effect has been observed in [**14**] using the drift-diffusion model for higher lattice temperatures (also see [**2**], Chap. 7). This indicates the importance of including thermal effects even in optoelectronic devices.

Finally, Figure 8.15 shows the stationary electron density and temperature in the device for two different forward bias. We clearly see the carrier confinement in the active region. Hot electrons are present mainly in the p-doped region and the temperature becomes minimal at the p-i heterojunction. This minimum is a well known thermoelectric effect at p-n junctions, see [**77**]. For larger applied bias, the electron temperature becomes large also in the n-doped region.

Parameter	Physical meaning	Numerical value
L_y	extension of device in y-direction	$10^{-5}\,\mathrm{m}$
L_z	extension in z-direction	$10^{-4}\,\mathrm{m}$
η	quantum efficiency	0.5
r	surface reflectivity	0.3
α_{ab}	absorption	$5000\,\mathrm{m}^{-1}$

Table 8.5: Physical parameters for a silicon p-i-n photo diode.

Photo diode

As a model for a photo diode we consider a one-dimensional vertical silicon p-i-n photo diode with length $6\,\mu$m consisting of a p-doped part of $2\,\mu$m length doped with $-5{\cdot}10^{22}\,\mathrm{m}^{-3}$, an intrinsic region of 2μm length doped with $5 \cdot 10^{17}\mathrm{m}^{-3}$, and an n-doped region of length $2\,\mu$m doped with $5 \cdot 10^{22}\mathrm{m}^{-3}$. Again, the doping profile is slightly smoothed. The physical parameters of silicon are listed in Table 8.1 and the optical parameters for the diode are listed in Table 8.5. The geometry of the device is similar to that of [**93**]. For the following numerical tests we employ a uniform grid with 101 nodes and the time step 5 ps.

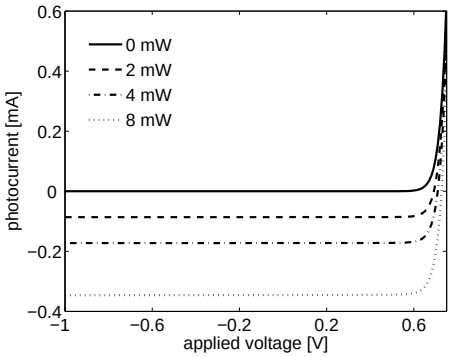

Figure 8.16: Dark current and photo current in the photo diode for various irradiation intensity.

In Figure 8.16 the dark current (no irradiation) and the photo current (positive irradiation) under backward bias are presented. The current increases significantly with increasing irradiation, proving that our model well reflects the typical behavior of a photo diode.

In the following numerical tests, the diode is driven by the backward bias of 0.2 V. The response of the device to a sinusoidal irradiation signal with amplitude 60 mW and frequency 1 GHz and to a digital signal with duration 200 ps are shown in Figure 8.17. Thereby the sinusoidal input signal is

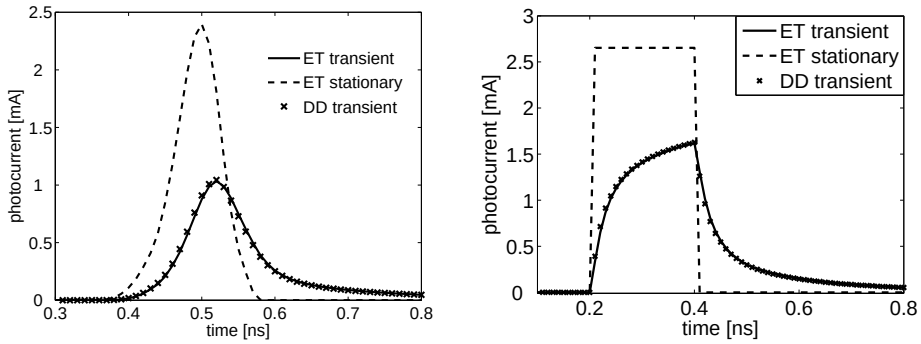

Figure 8.17: Response of the photo diode under backward bias of 0.2V for various irradiation signals. Left: Sinusoidal signal $P(t) = 60\sin(2\pi 10^9\,\mathrm{Hz}\,t)\,\mathrm{mW}$. Right: Digital signal with amplitude 60 mW and duration 200 ps.

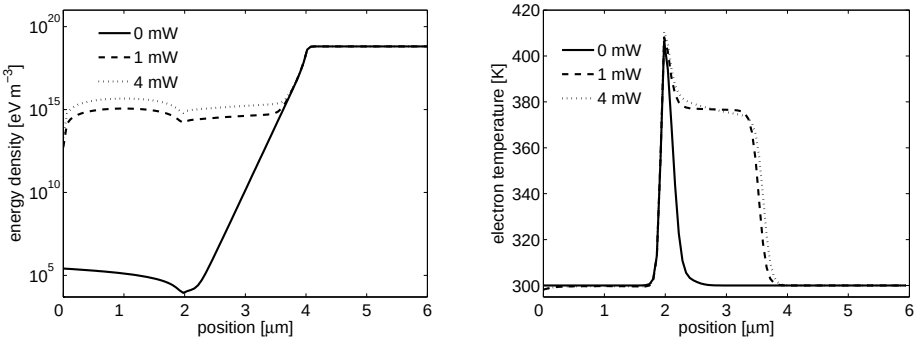

Figure 8.18: Electron energy density (left) and temperature (right) in the photo diode under backward bias of 0.2 V for various irradiation power.

used as a rough approximation of a lightpulse as observed in Figure 8.13 for the drift-diffusion model. We observe that the stationary energy-transport model does not give satisfactory results. The numerical results of the drift-diffusion and the energy-transport models are similar since the photo currents are rather small.

The stationary electron energy density and temperature are presented in Figure 8.18. The energy density (left figure) strongly increases in the p-doped and intrinsic regions with increasing irradiation. This is mainly caused by the increase of photo electrons in these regions since the temperature only increases in the intrinsic part of the device.

High-pass filter including optoelectronic devices

After the single device simulation of optoelectronic devices, in this section we consider the laser and photo diode as part of a small electric circuit (see Figure 8.19). In the considered example the laser diode is biased with a time-dependent voltage. The transmitted laser signal is received by the photo diode coupled to a high-pass filter only passing frequencies larger than the cutoff frequency. The filter consists of the photo diode, a capacitor, and three resistors. For numerical simulation the model equations for the photo diode - stationary or transient energy-transport and drift-diffusion in the following - are coupled to the MNA-equations for the high-pass filter.

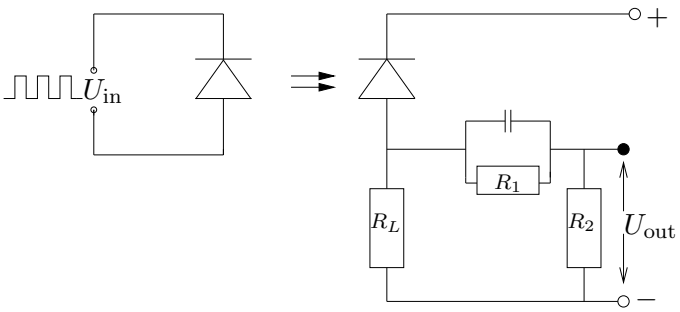

Figure 8.19: Photo diode with a high-pass filter.

As time-dependent voltage source for the laser diode we apply digital input signals with a value of 2.5 V and 3 V and frequencies of 1 GHz and 5 GHz. The photo diode is backward biased with 0.2 V. as in the previous section.

For the capacitance in the high-pass filter we assume a value of 10 pF, for the resistances $R_1 = 1\,\text{M}\Omega$ and $R_2 = 100\,\Omega$. For the load resistance, we have chosen a value of $R_L = 1\,\text{k}\Omega$.

The output of the laser diode, which in turn is the input for the photo diode, and the signal output of the high-pass filter for a 2.5 V digital signal U_{in} are shown in Figure 8.20 (upper row) for stationary and transient device simulations. The results for the high-pass output voltage computed with the stationary and transient energy-transport models differ significantly. This is expectable as the applied frequency is too large to be resolved by the stationary model. On the other hand, the differences betweenthe results

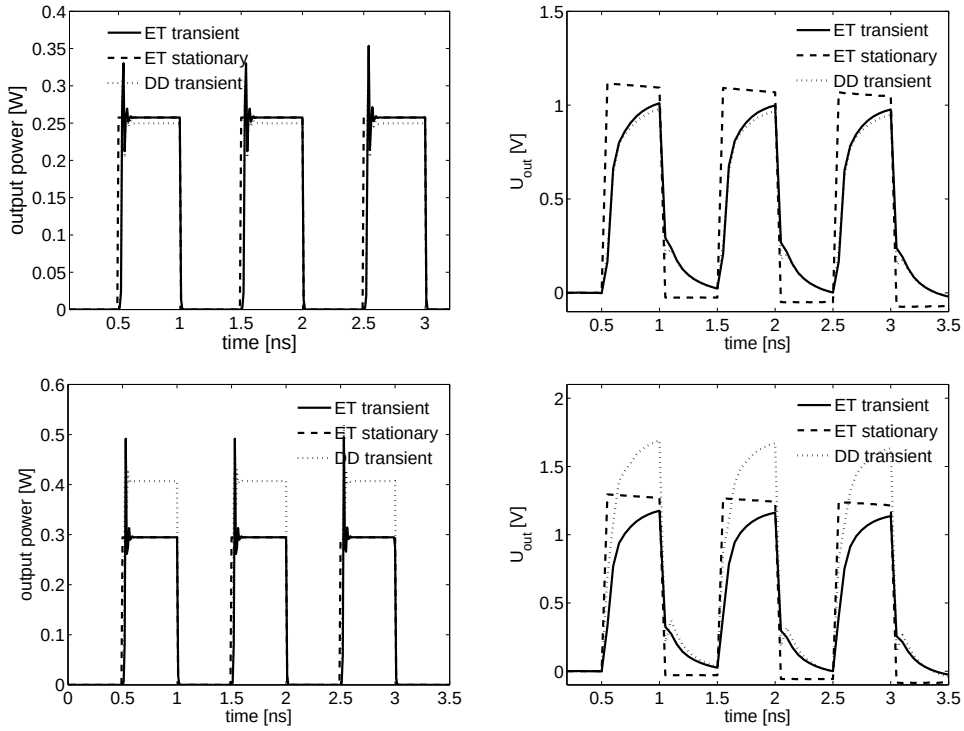

Figure 8.20: Output of the laser diode (left) and the high-pass filter (right) computed from the drift-diffusion and energy-transport models for a 1 GHz digital input signal with bias 2.5 V (upper row) and 3 V (lower row).

computed with the drift-diffusion and the energy-transport equations are minor. This behavior, however, changes drastically when the digital signal becomes larger. Figure 8.20 (lower row) shows the output signals of the laser diode and the high-pass filter for a digital signal of 3 V. There we observe that the output from the drift-diffusion model is significantly larger than that from the energy-transport equations.

The effect of a larger frequency is shown in Figure 8.21. We have employed a digital signal with a five times larger frequency than that of Figure 8.20. Again, the large frequency cannot be resolved by the stationary model.

In order to verify the filter effect, we apply digital signals of 2.5 V with various frequencies using the stationary energy-transport model (Figure 8.22). The use of the stationary model is justified by the chosen frequencies and applied voltage. The numerical results show that only high frequencies provide a significant output signal showing the high-pass behavior.

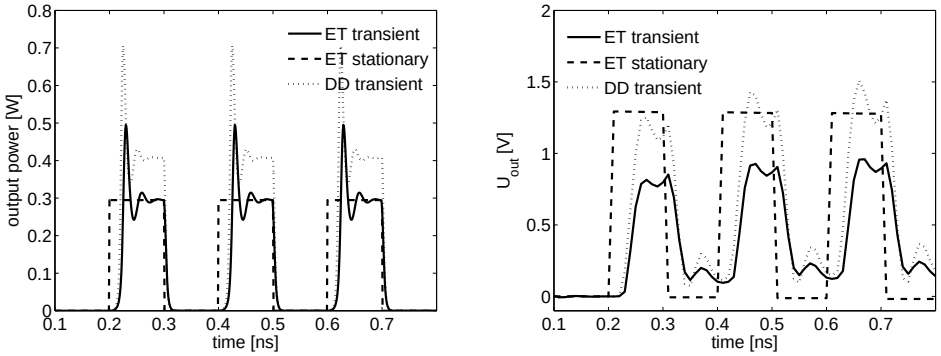

Figure 8.21: Output of the laser diode (left) and the high-pass filter (right) computed from the drift-diffusion and energy-transport models for a 5 GHz digital input signal with bias 3 V.

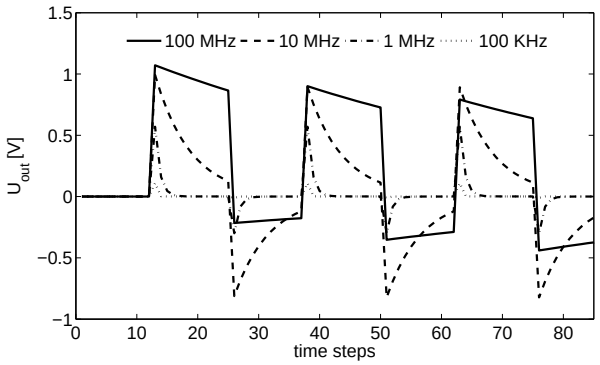

Figure 8.22: Output of the high-pass filter for input signals of various frequencies.

8.4 Lattice heating in semiconductor devices

So far we have clarified the influence of thermal effects in semiconductor devices by taking into account the thermal energy of the majority charge carriers. We have seen, that the influence on the electrical behavior is significant and thus even the impact on the electrical behavior of complete circuits can no longer be neglected.

Besides the heating of the charge carriers we expect also the heating of the crystal lattice to have significant influence on the electrical behavior of the devices. We notice that the electron temperature is a measure for the average thermal energy of the free electrons and does not coincide with the temperature of the crystal lattice.

In this section we will consider the influence of lattice heating onto the electrical behavior of single semiconductor devices

8.4.1 Ballistic diodes

As a first numerical example including the lattice heating modeled in § 3.4 we consider the one-dimensional n^+-n-n^+ ballistic silicon diode. The ballistic diode can be considered as a simple one-dimensional model of a MOS-transistor. The device domain is given by $\Omega_S = (0, L)$. The n^+ regions with a size of 100 nm each are characterized by a maximum doping concentration of $5 \cdot 10^{23}\,\mathrm{m}^{-3}$. The 400 nm long n-channel is characterized by a minimum doping concentration of $2{\cdot}10^{21}\,\mathrm{m}^{-3}$. The doping profile is smoothed by use of the tanh function. The device is modeled by the unipolar energy-transport model (for electrons only) consisting of the mass- and energy-conservation together with the constitutive current relations coupled to the unipolar Poisson equation. The physical parameters of silicon can be found in Table 8.1.

As boundary conditions in the boundary nodes $x = 0$ and $x = L$ (remember that in the scaled 1D-model $\partial\Omega_S = \Gamma_C = \{0, 1\}$) we assume Robin-type conditions for the electron density n and homogenous Neumann conditions for the electron temperature T_n, i.e.

$$J_n \cdot \nu = \theta_n(g_{n,a} - g_n), \qquad \nabla T_n \cdot \nu = 0 \qquad \text{on } \Gamma_c, t > 0. \tag{8.3}$$

Here $g_{n,a} = \mu_n n_a$ with n_a given in (3.18). The Robin parameter is chosen as $\theta_n = 2500$. As initial values we assume the device to be in thermal equilibrium, i.e.

$$g_n = \mu_n n_{\mathrm{eq}}, \quad V = V_{\mathrm{eq}}, \quad T_n = 1 \qquad \text{in } \Omega_S. \tag{8.4}$$

The described device can be considered as a standard-example for the simulation of semiconductor devices. The device has been considered and simulated with the energy-transport model in [**34, 52, 9**] and by use of hydrodynamic models in [**8, 10**]. In [**74**] the same device has been simulated

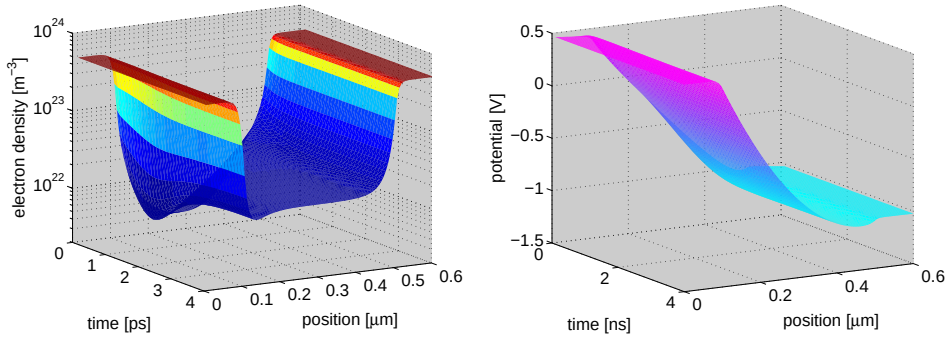

Figure 8.23: Electron density and electric potential in a ballistic diode biased with 1.5 V started with thermal equilibrium.

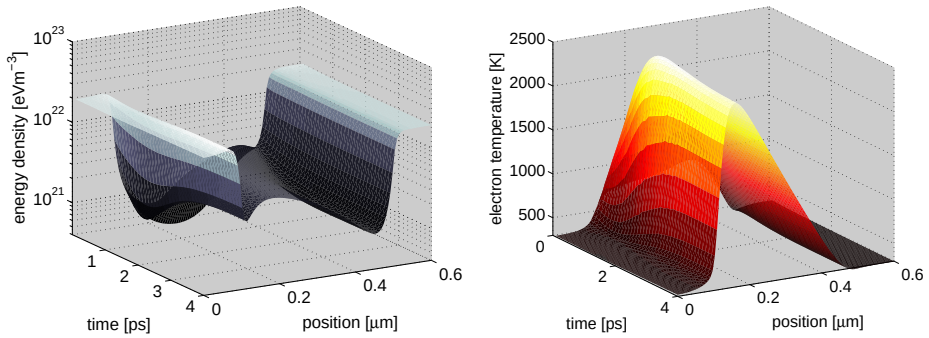

Figure 8.24: Energy density and electron temperature in a ballistic diode biased with 1.5 V started with thermal equilibrium.

using a simplified energy-transport model coupled to the heat flow equation for the lattice temperature. There, Dirichlet boundary conditions for the lattice temperature have been considered.

Due to the presence of that many comparable results we consider this example partially as a validation of our model. We firstly simulate the device without consideration of the lattice temperature. We perform the simulation for an applied bias of 1.5 V and observe the convergence of the device to a stationary state. The simulations are performed on a grid with 101 nodes using a time step size of $2 \cdot 10^{-13}$ s. The results are presented in Figure 8.23 and Figure 8.24. We observe the expected behavior and see that the device takes around 3-4 ps to reach the stationary state. This coincides with the simulation results presented in [**56**]. Moreover the electron and energy density as well as the potential and the electron temperature show the expected behavior. The electron temperature reaches a maximum value of 2344 K what is in good accordance to the results in [**34**]. Moreover we see that the choice of Neumann boundary conditions for T_n does not have

Parameter	Physical meaning	Numerical value
κ_L	thermal conductivity	$130\,\mathrm{W/(mK)}$
c_L	heat capacity	$700\,\mathrm{J/K/kg}$
ρ_L	material density	$2329\,\mathrm{kg/m^3}$
α_n	mobility power law parameter	2
R_{th}	thermal contact resistance	$0 - 10^{-7}\,\mathrm{s\ m^2/W}$
S_L	radiation parameter	$0 - 4 \cdot 10^{15}\,\mathrm{W/(m^3K)}$

Table 8.6: Thermal properties of silicon.

significant influence (compared to Dirichlet ones), as the temperature almost coincides with the ambient temperature at the boundary, anyhow.

In the next step we additionally include lattice heating and thus the unipolar form of the heat flow equation (5.12) into the model:

$$\rho_L c_L \partial_t T_L - \mathrm{div}(\kappa_L \nabla T_L) = \frac{3}{2} n \frac{T_n - T_L}{\tau_0} - S_L(T_L - T_{\mathrm{env}}).$$

The additionally necessary thermal parameters for silicon are listed in Table 8.6. In the following we compare the results we get for different choices of boundary conditions for the lattice temperature T_L, i.e. Dirichlet or Robin-type boundary condition

$$T_L = T_0 = 1, \qquad \text{or} \qquad -\kappa_L \nabla T_L = \nu \cdot \frac{T_L - T_0}{R_{\mathrm{th}}} \qquad \text{on } \Gamma_C, t > 0, \quad (8.5)$$

with different values for the thermal resistance R_{th}. The thermal radiation is neglected for the moment (i.e. $S_L = 0$). Again we assume thermal equilibrium as initial values for the device as in (8.4). Then the initial values for the lattice temperature are given (in the scaled form) as

$$T_L(0) = 1 \qquad \text{in } \Omega_S. \quad (8.6)$$

In Figure 8.25 (left) we see the evolution of the lattice temperature in the device for a bias of 1.5 V, where Dirichlet boundary conditions have been applied. We observe that the temperature increases by less than 1 K, what coincides with the simulation results presented in [**74**]. This can not be considered as a significant increase of temperature. The prescription of Dirichlet boundary conditions corresponds to the assumption of infinite heat flux across the boundary. This physically questionable assumption together with the high thermal conductivity of silicon causes a very rapid drain of heat, what results in the small temperature increase. This changes, if we assume the more realistic Robin-type boundary conditions and take into account the thermal resistance of the contacts instead. For a choice of $R_{\mathrm{th}} = 10^{-8}\ \mathrm{m^2K/W}$ (compare [**43**]) the increase of temperature becomes more obvious as we see from Figure 8.25 (right). Due to the high thermal

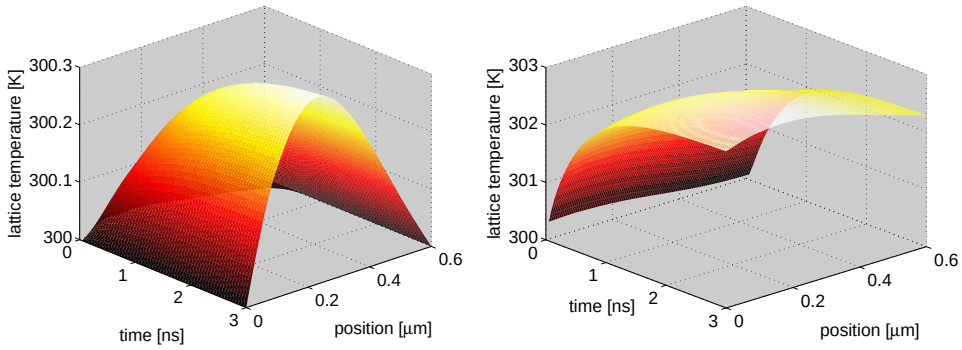

Figure 8.25: Lattice temperature in a ballistic diode biased with 1.5 V started with thermal equilibrium. Computation for different boundary conditions. Left: Dirichlet, Right: Robin type with $R_{\text{th}} = 10^{-8}\text{m}^2\text{K/W}$.

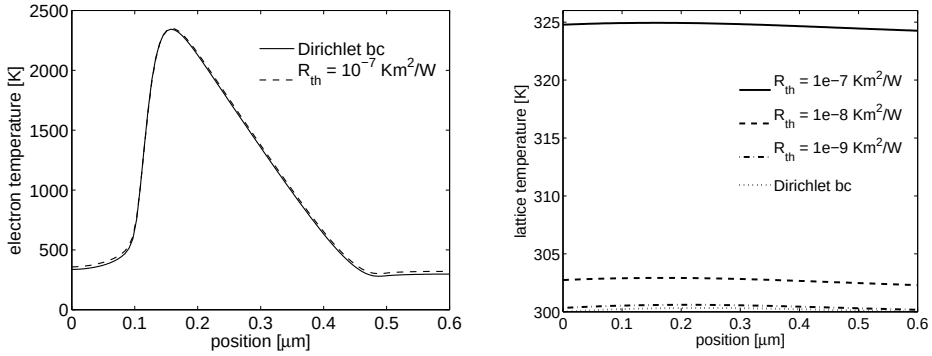

Figure 8.26: Electron and lattice temperature in a ballistic diode biased with 1.5 V started with thermal equilibrium for different boundary conditions.

conductivity the lattice temperature does not differ strongly within the device. Furthermore we see in Figure 8.25 that the heat effects of the lattice take much longer to reach the stationary state than the electrical effects do (compare Figures 8.23-8.24).

In Figure 8.26 we depict the influence of the boundary conditions for T_L on the electron and lattice temperature within the device. Obviously, we see that the electron temperature does not change significantly even for a very high thermal resistance. In contrast, we observe a tremendous increase of the lattice temperature with increasing thermal resistance. We remark that the choice of $R_{\text{th}} = 10^{-7}\,\text{m}^2\text{W/K}$ might be unrealistically high and that we neglected radiation in the simulation.

To clarify the impact of the lattice heating onto the electrical behavior of the considered device we compare the IV-characteristic of the energy-transport model with constant lattice temperature to the one with variable

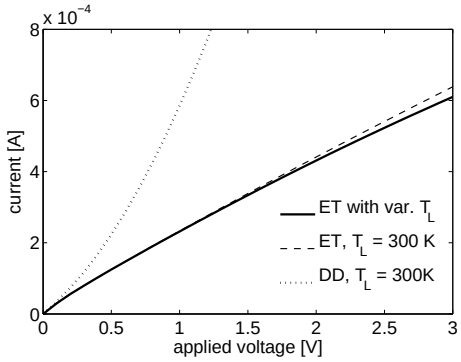

Figure 8.27: IV-characteristic for the ballistic diode modeled with the drift-diffusion model and the energy-transport model with constant and variable lattice temperature.

lattice temperature, see Figure 8.27. The simulation was performed under the assumption of Robin boundary conditions with $R_{\text{th}} = 10^{-8}\,\text{m}^2\text{W/K}$ and radiation was neglected. Nonetheless we observe that the influence onto the IV-curve is rather small and becomes obvious for very high applied bias only. This shows that for devices of the chosen size of around 500 nm the influence of lattice heating seems to be negligible. For comparison the IV-curve computed with the drift-diffusion model is depicted and again we see that the thermal effects of the charge carriers can not be neglected even for big devices.

50 nm-channel ballistic diode

In industrial application it is observed that thermal effects in semiconductor devices become stronger with decreasing device extension. As a second example we therefore consider a smaller ballistic diode with a total length of $L = 250$ nm. The n-channel has a length of 50 nm and the n^+-regions have a length of 100 nm each. The doping concentrations are the same as for the previous example. The described device has been modeled and simulated with an energy-transport model in [**9**] and with the hydrodynamic model in [**56**], in both cases without consideration of the lattice heating. As in application smaller devices are driven by smaller bias we simulate the 50 nm channel diode with a bias of 1V. Again we apply thermal equilibrium (8.4) and (8.6) as initial conditions and boundary conditions as in (8.3). For the lattice temperature T_L we assume Robin-type boundary conditions as in (8.5) with $R_{\text{th}} = 10^{-8}$ m^{2}K/W. As radiation parameter we apply the value of $S_L = 4 \cdot 10^{15}\,\text{W}/(\text{m}^3)\text{K}$. If we assume an extension of the device in y- and z-direction of 250 nm, as well, this parameter corresponds to a transmission of approximately $6 \cdot 10^{-4}$ W/K for the entire device or 10^9 W/(m^{2}K), what

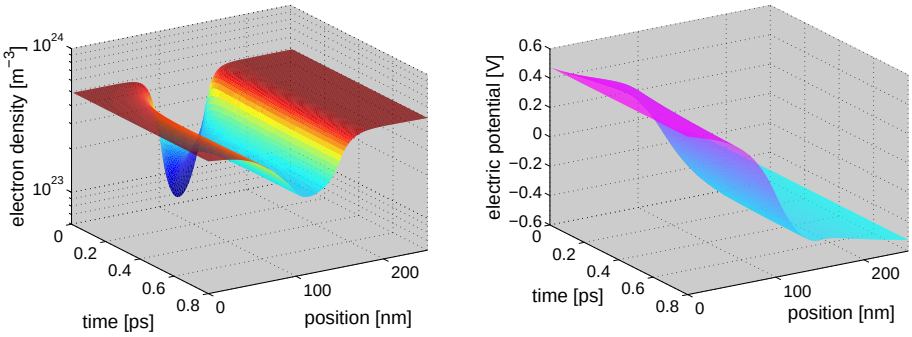

Figure 8.28: Electron density and electric potential in a ballistic diode with 50nm channel biased with 1 V started with thermal equilibrium.

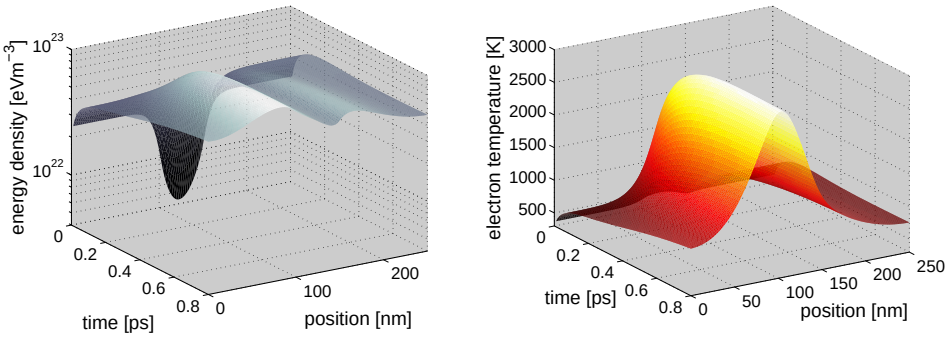

Figure 8.29: Energy density and electron temperature in a ballistic diode with 50 nm channel biased with 1 V started with thermal equilibrium.

is significantly too high (compare [**16**]).

We perform the simulation on a spatial grid with 101 nodes and apply a time step size of 10^{-14} s to resolve the transient response of the device to the abrupt increase of bias.

For sake of completeness in Figures 8.28-8.29 we present the transient behavior of all considered variables in the model. We observe that the electrical values reach the stationary state considerably faster than in the first example. Comparing the 400 nm to the 50 nm channel device, we observe a similar smooth distribution of the electric potential in the devices. For the small device, however, we observe that the electron density in the channel increases significantly compared to the predefined doping concentration. For the ballistic diode of the first example we observed a difference between electron density in the channel and the electron density in the n^+-layers of two magnitudes, whereas for the smaller device this difference is significantly smaller. This in turn results in a considerably higher thermal energy in and around the channel as we clearly see from Figure 8.29 (left). The presence of

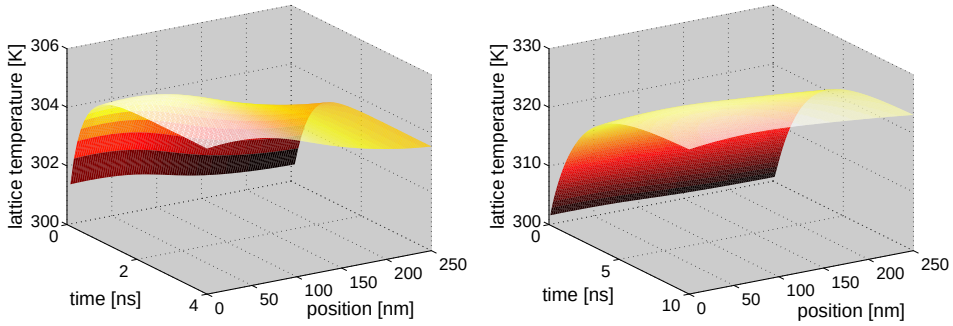

Figure 8.30: Lattice temperature in a ballistic diode with 50nm channel biased with 1 V started with thermal equilibrium. Computation with consideration of radiation (left) and without (right).

more high energetic charge carriers clarifies the reason for stronger thermal effects in smaller devices.

Moreover the electron temperature (the average thermal energy per electron) is depicted in Figure 8.29 (right). It reaches a maximum value of 2860 K for the bias of 1V what again is higher than in the bigger device. Additionally we observe that the prescription of Neumann boundary conditions for the electron temperature T_n has influence on the temperature distribution as the temperature does not relax to ambient or lattice temperature at the boundary.

In [**9, 56**] the same device is simulated for a smaller bias. The qualitative behavior of our results are in good accordance with the results presented there.

The lattice temperature of the device is shown in Figure 8.30 (left). Again we observe that the lattice temperature takes much more time to reach the stationary state. Moreover, we observe an increase of the lattice temperature of around 5 K under the consideration of very high thermal radiation to environment. To compare the effect of lattice heating to lattice heating in the 600 nm device, we perform the same simulation without consideration of radiation. The corresponding result for the lattice temperature is depicted in Figure 8.30 (right). There we get a lattice temperature of around 325 K compared to 302 K in the 600 nm device. This clearly shows that smaller devices heat up significantly more.

The results for the stationary computations of the electron and lattice temperature for 1 V bias are shown in Figure 8.31, where we clearly see that the electron temperature does not relax to the lattice temperature at the boundary. Moreover we see that the lattice heating also affects the electron temperature even though this effect is not very high.

Lastly we want to examine the influence of lattice heating onto the elec-

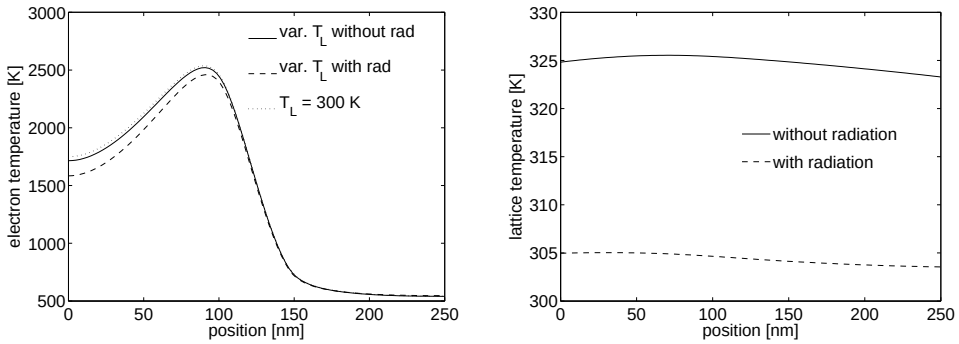

Figure 8.31: Stationary computation of electron and lattice temperature in a ballistic diode with 50nm channel biased with 1 V started with thermal equilibrium for different boundary conditions.

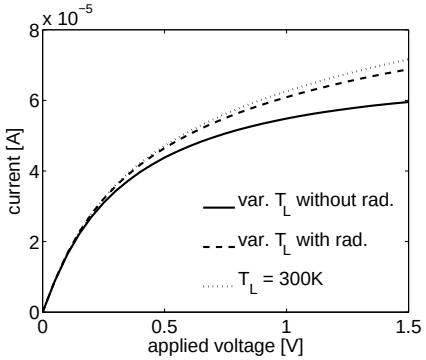

Figure 8.32: IV-characteristic for the 50nm channel ballistic diode modeled with the drift-diffusion model and the energy-transport model with constant and variable lattice temperature.

trical behavior of the device. In Figure 8.32 we present the current-voltage characteristic computed with and without consideration of lattice heating. We observe that for the smaller device the difference between the two curves becomes more obvious even for smaller applied bias. We see that with decreasing radiation the influence onto the electrical performance becomes even stronger. We notice that we model the thermal radiation by the term $S_L(T_L - T_{\text{env}})$ with constant environmental temperature. In application, this is not always given, as the environmental temperature might increase due to continuous radiation from the considered and the surrounding elements in electric circuits. An increase of T_{env}, in turn, decreases the thermal radiation what then again would increase lattice heating and influence the electrical performance of the device. We remark that the considered radiation parameter has been chosen very high and might be unrealistic.

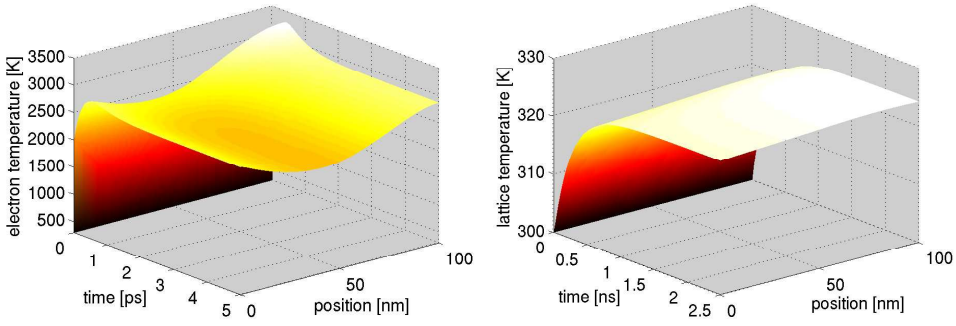

Figure 8.33: Transient computation of electron and lattice temperature in a 100 nm *pn* diode with maximum doping concentrations $C_m = 5 \cdot 10^{23}$ m^{-3} for the abrupt forward bias of 1.5 V.

In any case the simulation of lattice heating seems to get more important due to the miniaturization trend in semiconductor development.

8.4.2 Bipolar *pn* diodes

To examine the lattice heating in bipolar devices we consider the 100 nm silicon *pn* diode from § 8.1 where the maximum doping concentration is given as $C_m = 5 \cdot 10^{23}\,\mathrm{m}^{-3}$. The device is modeled by the energy-transport equations for the electrons, the drift-diffusion equations for the holes coupled to (scaled version of) the heat flow equation (5.12). If not mentioned explicitly we assume a radiation parameter of $S_L = 4 \cdot 10^{15}$ W/(m^{3}K).

As initial values we again assume the device to be in thermal equilibrium (8.1). The Robin-type boundary conditions for n and p are given by (3.21) with $\theta_n = \theta_p = 2500$, and for T_n we again employ homogenous Neumann boundary conditions (3.20). For the lattice temperature T_L we generally assume Robin boundary conditions (8.5) with a thermal resistance $R_{\mathrm{th}} = 10^{-8}\,\mathrm{sm}^2/\mathrm{W}$. If we use different boundary conditions this is stated explicitly.

Firstly we apply a forward bias of 1.5 V to the device in thermal equilibrium and observe the transient response of the electron and lattice temperature in Figure 8.33. We observe a strong and quick increase of the electron temperature in the entire device. Moreover we see, in contrast to the unipolar devices we hitherto considered, a kind of temperature overshoot in the beginning. The temperature increases to a maximum value of around 3300 K in the n-region and then slowly decreases again towards the stationary state. Furthermore, we observe the minimum of the electron temperature around the *pn* junction, what is a well known effect in bipolar devices.

The lattice temperature on the other hand increases significantly slower than the electron temperature and additionally does not show the mentioned overshoot. However, we observe a significant increase of around 25 K of the

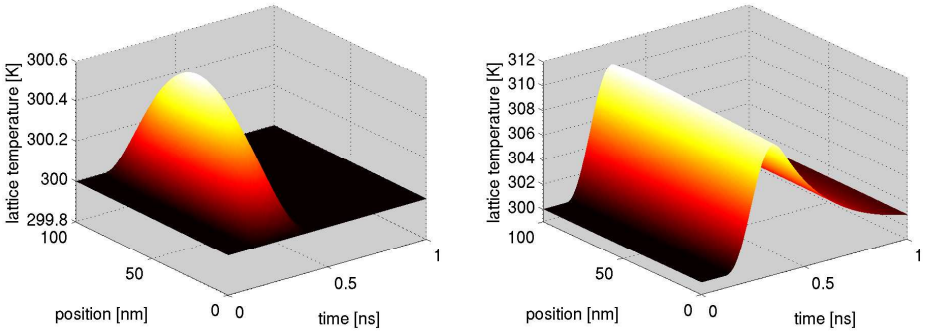

Figure 8.34: Lattice temperature in a 100 nm *pn* diode with maximum doping concentrations $C_m = 5 \cdot 10^{23}$ m^{-3} for the sinusoidal input signal. Left: with Dirichlet boundary conditions; Right: Robin conditions with $R_{\text{th}} = 10^{-8}$ m^2 K/W.

lattice temperature in the stationary state.

To consider the lattice heating of the device for time dependent bias, we bias apply the dependent voltage $v(t) = 1.5 \sin(2\pi 10^9 \text{Hz} t)$ V to the device. In Figure 8.34 we depict the results for the lattice temperature simulated for one oscillation of the source for the mentioned Robin-type boundary conditions (right) compared to the results for Dirichlet boundary conditions (left). For the choice of Dirichlet boundary conditions we observe an increase by less than 1 K for forward bias. During the reverse bias alternation the lattice cools down quickly to the equilibrium temperature again. The effect of relaxing to the environmental temperature for backward bias is physically reasonable as the device is depleted of charge carries and thus no heating can occur. The rather small temperature increase of 0.6 K is expected as the assumption of Dirichlet boundary conditions corresponds to the assumption of infinite temperature flux across the boundary, what does not rebuild the realistic case.

For the prescription of Robin-type boundary conditions we observe a considerably higher increase of the lattice temperature T_L for the forward bias alternation. As lattice heating happens rather slow, compared to the electrical effects, we observe that the maximum of the lattice temperature is considerably smaller than the value for the stationary state under the bias of 1.5 V (compare Figure 8.33). Moreover, Figure 8.34 (right) shows that the relaxation of the lattice temperature during the backward bias alternation happens even slower. Thus after a complete oscillation we still observe a slightly higher lattice temperature than 300 K.

Accordingly, for increasing number of oscillations we expect increasing lattice temperature as well. This accumulation can be observed in Figure 8.35 where we depicted the lattice temperature during three oscillations

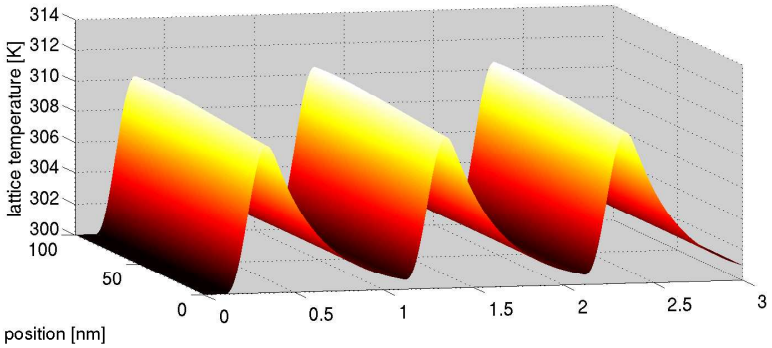

Figure 8.35: Lattice temperature in a 100 nm *pn* diode with maximum doping concentrations $C_m = 5 \cdot 10^{23}$ m^{-3} for a sinusoidal input signal $v(t) = 1.5\ \sin(2\pi 10^9 Hzt)$V.

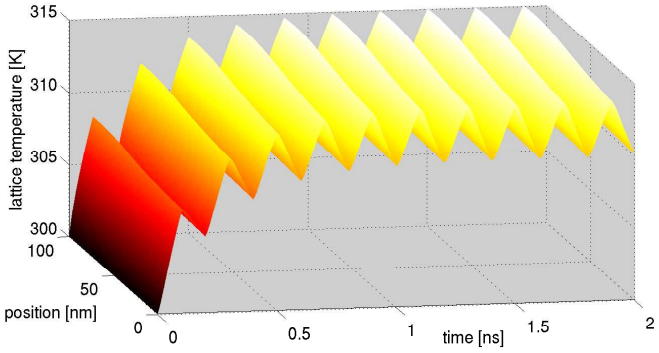

Figure 8.36: Lattice temperature in a 100 nm *pn* diode with maximum doping concentrations $C_m = 5 \cdot 10^{23}$ m^{-3} for a 1.5 V digital input signal with a frequency of 5 GHz.

of the sinusoidal voltage source. We see that the maximum values of T_L during the alternation increases slightly with increasing number of oscillations.

This effect becomes even more obvious if we apply a signal with a higher frequency. In Figure 8.36 we show the transient behavior of the lattice temperature in the device during 10 oscillations of a digital input signal of 1.5 V with a frequency of 5 GHz. Due to the higher frequency the maximum bias of 1.5 V is applied for a shorter duration per oscillation and consequently the maximum temperature during the first alternation is smaller than we observed for the 1 GHz signal in Figure 8.35. In turn the backward biased period is shortened as well an thus the period of temperature relaxation. Thus the lattice heating due to the mentioned accumulation becomes more

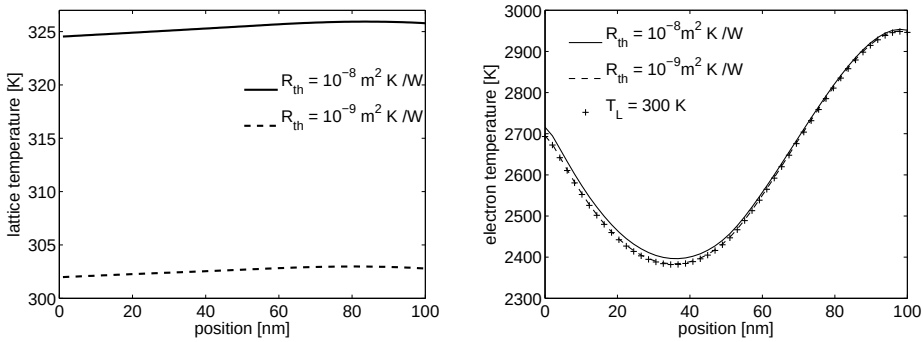

Figure 8.37: Lattice and electron temperature in a *pn* diode with maximum doping concentrations $C_m = 5{\cdot}10^{23}$ m^{-3} for 1.5 V bias for different boundary parameters with consideration of radiation. Stationary computation.

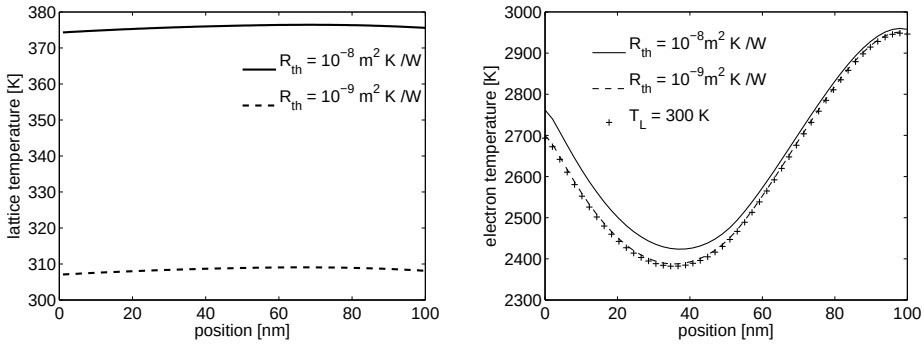

Figure 8.38: Lattice and electron temperature in a *pn* diode with maximum doping concentrations $C_m = 5{\cdot}10^{23}$ m^{-3} for 1.5 V bias for different boundary parameters without consideration of radiation. Stationary computation.

obvious for signals with higher frequency. After a few oscillations the maximum temperature value of around 315 K is reached for the maximum forward bias of 1.5 V. However, the maximum temperature value reached by the bias with the digital signal is below the value the stationary computation predicts, see Figure 8.37. This intensifies the advantages of the transient model compared to the stationary one.

To clarify the importance of a proper choice of the values for the contact resistance R_{th} and the radiation parameter S_L for realistic simulations in Figures 8.37 and 8.38 we show the results for the stationary computations of the lattice and the electron temperature for different choices of the these parameters. We see that the choice of a smaller thermal resistance significantly reduces the lattice heating and moreover Figure 8.38 shows that the results strongly depend on the consideration of thermal radiation. Furthermore we see that the influence of the lattice heating onto the electron temperature is

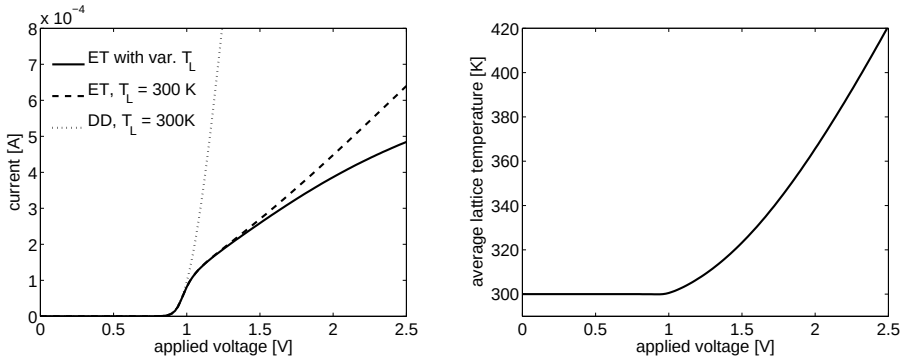

Figure 8.39: Left: IV-characteristic for the *pn* diode computed with the drift-diffusion and the energy-transport model. Right: Averaged lattice temperature in the *pn* diode for different applied bias. Stationary computations..

small, but we observe that higher lattice temperature also causes a higher electron temperature what is expected by the model equations.

Finally, we depict the current-voltage characteristics of the considered device for our model and compare the result to those achieved be the energy-transport model with constant lattice temperature and the drift-diffusion model in Figure 8.39 (left). We see that for the considered device, heating of the crystal lattice influences the electrical performance. The effect increases with increasing applied voltage. In Figure 8.39 (right) we show the average lattice temperature in the device dependent on the applied voltage. For high applied bias the lattice temperature computed with our model increases even up to 420 K. We notice that a bias of 2.5 V for the considered device might by unrealistic. Nonetheless, the graphs in Figure 8.39 show that with increasing lattice temperature the electrical behavior of the device changes compared to the model with constant lattice temperature. Thus, if we consider (as for the previous example) that the radiation might decrease due to increasing environmental temperature, the lattice heating might influence the electrical performance of the semiconductor devices even more than depicted here.

8.5 Thermoelectric simulation of a frequency multiplier

As the final numerical example we consider the frequency multiplier depicted in Figure 8.40. The circuit consists of a voltage source inducing an oscillatory signal with the eigenfrequency of the first oscillator. The signal is transported to the second oscillator via the *pn* diode and due to the nonlinear behavior of the device a mixture of overtones occurs. For the second oscillator it holds $C_2 = C_1/2$ and $L_2 = L_1/2$ such that it resonates with the double frequency and other frequencies are damped out.

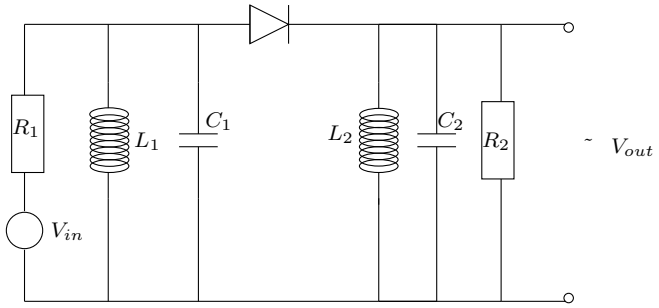

Figure 8.40: Frequency multiplier

Parameter	Physical meaning	Numerical value
R_1/R_2	resistances	$100/1000\Omega$
C_1	capacitance	$(3.2 \cdot 2\pi)^{-1} \cdot 10^{-10}\,\mathrm{F}$
L_1	inductance	$(3.2 \cdot 2\pi)^{-1} \cdot 10^{-6}\,\mathrm{H}$
κ_R	heat conductivity of resistors	$237\,\mathrm{W/(mK)}$
c_R	heat capacity of resistors	$900\,\mathrm{J/(kgK)}$
ρ_R	material density of resistors	$2700\ \mathrm{kg/(m^3)}$
L_R	length of resistors	$10^{-6}m$
A_R	cross section of resistors	$10^{-7}m$
α_1	1st thermal coefficient(see [**16**])	$1/(273\,K)$
α_2	2nd thermal coefficient (see [**16**])	$1/(273\,K)^2$

Table 8.7: Electrical and thermal parameters of the frequency multiplier

The frequency multiplier is stimulated with the time dependent voltage signal $v(t) = 3 \cdot \sin(3.2 \cdot 2\pi \cdot 10^9 \mathrm{Hz}\, t)$. The parameters are chosen such that the first oscillator resonates at a frequency of 3.2 GHz.

We only consider the resistors and the device in the circuit to be thermally relevant elements. We thermally model the resistors as thermal lines and the device according to § 3.4. Thus the only thermally lumped elements are the artificial nodes modeling the contacts between the resistors and the device. We notice, that the temperature at the contacts coincides with the temperature at the boundary of the thermal lines. For the device, however, the contact temperature are applied in terms of Robin boundary conditions as described in 3.53. All necessary electrical and thermal parameters of the circuit elements can be found in Table 8.7.

As *pn* diode in the circuit we consider a silicon diode of 100 nm with a maximum doping profile of $3 \cdot 10^{23}\,\mathrm{m}^{-3}$ in the n doped region and minimum of $-3 \cdot 10^{23}\,\mathrm{m}^{-3}$ in the p doped region. As thermal radiation parameter we assume a value of $S_L = 4 \cdot 10^{15}\,\mathrm{W/(m^3K)}$. We assume a thermal contact resistance of $R_{\mathrm{th}} = 10^{-8}\,\mathrm{sm^2/W}$. The remaining parameters are listed in Tables 8.1 and 8.6.

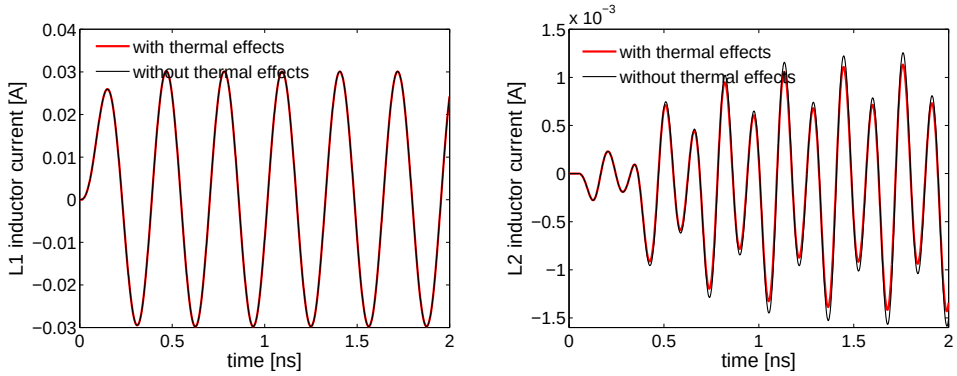

Figure 8.41: Inductor currents for L1 (left) and L2 (right) in the frequency multiplier.

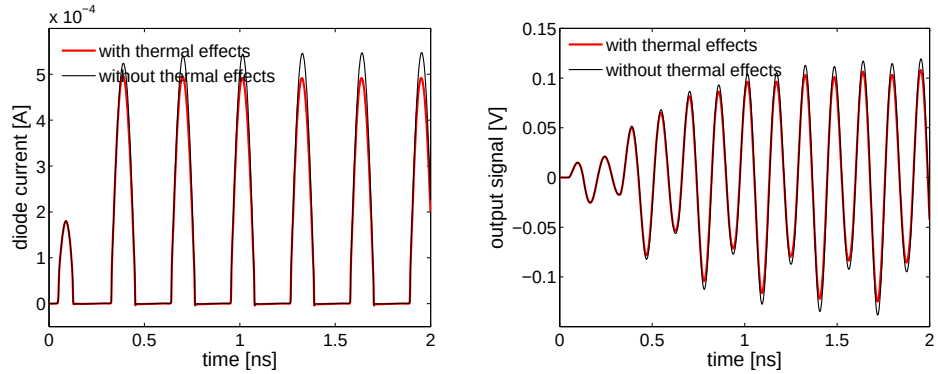

Figure 8.42: Diode current (left) and output signal of the frequency multiplier.

In Figure 8.41 the currents through the inductances L_1 and L_2 are depicted for the first 2 nanoseconds of the oscillation. We clearly see the double frequency in the second oscillator. We observe that the amplitude in the second oscillator is not constant. This is due to the fact, that we observe a damped oscillation in the second oscillator between two excitations caused by the diode signal (see Figure 8.42 (left)). The corresponding output signal is depicted in the right graph of Figure 8.42, where we again can observe the double frequency.

Moreover from Figures 8.41 - 8.42 we observe a difference in the maximum output values between the simulation including and without thermal considerations. This difference, however, is mainly caused by the thermal effects in the device, as we namely observe, that the current through the first inductor (Figure 8.41 (left)) does not differ. Moreover we see that the excitation signal for the second oscillator, namely the diode current, is smaller in the case of included thermal considerations. This finally causes

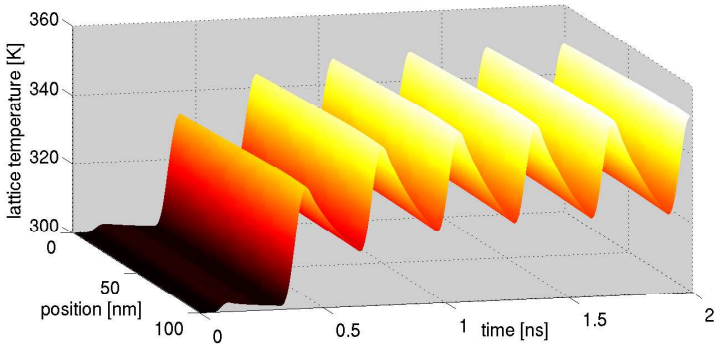

Figure 8.43: Lattice temperature of the diode in the frequency multiplier.

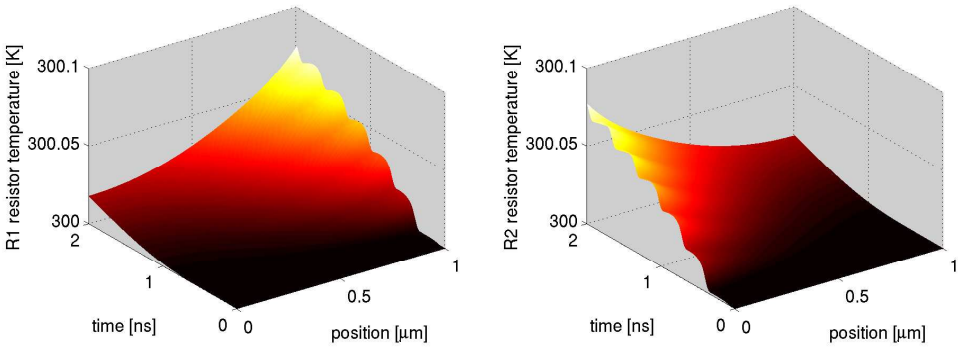

Figure 8.44: Temperature of the resistors R1 (left) and R2 (right) in the frequency multiplier.

the difference in the output signals.

Finally the transient behavior of the distributed temperature values is shown in Figures 8.43 - 8.44. For the diode temperature we see the expected behavior as observed in the single device simulation in Figures 8.35 and 8.36. The resistor heating however happens significantly slower. After 2 nanoseconds an increase of temperature of less than 0.1 K can be observed. Thus the influence onto the resistivity according to (4.18) is very small and the thermal effects in the resistors do not influence the current in the first oscillator (see Figure 8.41). However, we clearly see that the temperature in the resistor is higher at the contact connected to the diode, caused by the heat exchange with the significantly hotter device.

Summary and outlook

The trend of miniaturization in electrotechnology enforces refined circuit and device modeling for enhancement of existing circuit simulators. The hitherto widespread compact model approach meets the new demands with high effort, only. Moreover, due to decreasing size of devices and increasing packing density on chips and integrated circuits thermal effects become predominant and affect the signal behavior of circuits significantly. Thus, device and circuit models without consideration of thermal effects won't be suitable in the near future. Moreover, stationary models won't meet the demands as higher frequencies are used.

Using the one-dimensional transient energy-transport model for devices allows for consideration of thermal effects in terms of the charge carrier temperature or thermal energy, respectively. The model represents a system of elliptic and parabolic partial differential equations. The electric network is represented by a system of differential algebraic equations resulting from the widespread modified nodal approach. The systems are coupled via boundary conditions.

More accurate thermal device modeling is achieved by non isothermal modeling of the lattice temperature by the widespread heat flow equation. The corresponding source term for the parabolic differential equation is derived under thermodynamic as well as phenomenological considerations. The mutual thermal interaction between network elements is modeled by an accompanying thermal network consisting of lumped and distributed versions of the heat flow equation for thermally relevant elements in the network. Depending on the topology of the network, the thermal model is represented by a system differential or differential algebraic equations.

Thermal and electric systems are coupled via temperature-dependent material parameters and heat production terms in electric elements. Thermal and electric effects are strongly coupled via source terms of the heat flow equation and energy conservation law in the device model. The complete thermoelectric model for circuit-device systems is represented by a system of elliptic and parabolic partial differential algebraic equations. About the index of the coupled system no results are known up to now.

For time discretization of the complete system the A-stable BDF2 is applied to account for the differential algebraic character of the problem.

The application of the Marini-Pietra hybridized mixed finite element scheme for space-discretization of the device model equations allows to keep the positivity of discrete charge carrier densities as well as the continuity of the device current. The application of exponential fitting allows for a good approximation of large gradients of the electric potential.

Iterative algorithms for the solution of the discretized device equations allow for the simulation of electric and optoelectronic devices without the expensive computation of derivatives.

The presented examples clarify that hot carrier effects affect the signal behavior of electric and optoelectronic devices. The results for the coupled system of energy-transport and network equations show, that the consideration of hot carrier effects in devices is imported for detailed circuit simulation. With decreasing size of devices the impact of lattice heating becomes stronger. The presented examples show that for devices with size or channel length of around 50 - 100 nm lattice heating influences the electrical performance of devices, considerably. This makes it necessary to include lattice heating into circuit and device simulators for efficient and reliable circuit simulation in the future.

Finally the question about the index of the complete coupled system or the system of network and energy-transport equations remains open. The determination of the index for the coupled system is surely an exiting starting point for future research and will lead to more efficient and reliable simulation of the system. The presented coupling strategy might be enhanced to the case of two- or more dimensional device models to allow for detailed simulation of circuits containing transistors. Further on, for efficient simulation of arbitrary circuit-device systems the improvement of the presented iterative algorithms will be an interesting field of research in the future.

Appendix A

Notation

Physical constants

Speed of light in vacuum	c	$2.99792 \cdot 10^{8}$ m/s
Reduced Planck constant	$\hbar$	$1.05457 \cdot 10^{-34}$ Js
Boltzmann constant	k_B	$1.38066 \cdot 10^{-23}$ J/K
Elementary charge	q	$1.60218 \cdot 10^{-19}$ C
Permittivity in vacuum	ε_0	$8.85418 \cdot 10^{-12}$ As/(Vm)

Symbols

$t, \triangle t$	time variable, time step size
x, h	space variable, spatial step size
$\alpha_{\mathrm{bg}}, \alpha_f, \alpha$	background/ facet/total loss of photons in laser diode
α_{ab}	optical absorption of photo diode material
β	eigenvalue of Helmholtz equation
$c_L, c^d, \hat{c}^l$	heat capacity of lattice/distributed/lumped elements
d_c	width of laser cavity
e	node potentials in electric network
$\varepsilon_{\mathrm{opt}}$	dielectric function of laser
ε	semiconductor permittivity constant
η	quantum efficiency of photo diode material
g_R	conductivity of resistor
$g(n), g_0$	optical gain, differential gain
i	branch currents in electric network; imaginary number
i_C, i_L, i_R	current through capacitors/inductors/resistors
i_s, i_v	current of current/voltage sources
j_S	semiconductor current density at all terminals
θ_n, θ_p	Robin-parameter for electron/hole density
κ_i, κ_L	heat conductivity of i-th thermal line/semiconductor lattice
m_n, m_d, m_l	number of thermal nodes/distributed/lumped elements
μ_n, μ_p	electron/hole mobility

μ_{opt}	refractive index
ν	outer normal
$n, n_a, n_i, n_{\text{th}}$	electron/quasi-equilibrium/intrinsic/threshhold density
n_n, n_R, n_S	number of circuit nodes/resistive branches/device terminals
p, p_a	hole/quasi-equilibrium hole density
q	elementary charge
r	surface reflectivity
$\rho_L, \rho^d, \hat{\rho}^l$	material density of device lattice/distributed/lumped thermal elements
τ_n, τ_p	electron/hole lifetime
$\tau_0, \tau_{0,p}$	energy relaxation time for electrons/holes
v	branch voltages in electric network
u	total internal energy density
u_n, u_p	internal energy density of electrons/holes
u_w, u_{w_p}	thermal energy density of electrons/holes
u_E, u_L	internal energy density of electric field/device lattice
v	branch voltages in electric network
v_C, v_L, v_R, v_s	voltage at capacitors/inductors/resistors/voltage sources
v_g	group velocity of photons
w, w_p	thermal energy density of electrons/holes
w_a	quasi-equilibrium thermal energy density of electrons
ω	angular frequency of light
A	area of irradiation of the photo diode
A^d	cross section of distributed thermal element
$\mathcal{A}, \mathcal{A}_d^{\text{th}}$	incidence matrix of electric/thermal network
$\mathcal{A}_S^{\text{th}}$	thermal incidence matrix of semiconductor device
$\mathcal{A}_C, \mathcal{A}_L$	incidence matrix of capacitors/inductors
$\mathcal{A}_R, \mathcal{A}_S$	incidence matrix of resistors/devices
$\mathcal{A}_I, \mathcal{A}_V$	incidence matrix of current/voltage source branches
B	spontaneous recombination factor
C_n, C_p	electron/hole Auger recombination coefficient
$\mathcal{C}$	capacitance of capacitors
C	doping profile
$\Gamma, \Gamma_I, \Gamma_C$	boundary/insulating boundary/contacts of the device
E	electric field
E_c, E_v	conduction/valence band
E_g, E_G	energy gap of low/wide gap material
$\hat{\boldsymbol{F}}^S, \hat{\boldsymbol{F}}^d$	thermal flux from device/thermal line into thermal nodes
F_k^S	thermal flux through semiconductor contact k
$\Phi_L, \widetilde{\Phi}_L$	Magnetic flux variable/function through inductors
$\mathcal{G}$	Matrix $\partial g_R / \partial v$
G_{opt}	generation rate of photons
H	heat source

$\boldsymbol{I}$	unity matrix
$\boldsymbol{I}_{\mathrm{th}}$	Domain $[0, L_{\mathrm{th}}]$ of thermal lines
J_n, J_p, J_d	electron/hole/displacement current density
J_{tot}	total current density
$J^d_{\mathrm{th}}, J^S_{\mathrm{th}}$	thermal flux density of thermal lines/devices
J_u	total energy flux density
J^n_u, J^p_u	internal energy flux density of electrons/holes
J_w, J_{w_p}	thermal energy flux density of electrons/holes
J^E_u, J^L_u	internal energy flux density of electric field/device lattice
$\mathcal{L}$	inductivity of inductors
L, L_{th}, L_C	length (diameter) of device/thermal line/laser cavity
$\mathcal{K}, \hat{\mathcal{K}}$	matrix identifying electric branches with thermal branches/nodes
$M, \hat{M}, \hat{\boldsymbol{M}}$	thermal mass of distributed/lumped elements/thermal nodes
$\mathcal{M}$	matrix to identify lumped thermal elements with nodes
N_c, N_v	effective density of states in conduction/valence band
$\lvert\Xi\rvert^2$	optical field intensity
$P_i, \hat{P}$	electro-thermal source of distributed/lumped element
$\hat{\boldsymbol{P}}, \boldsymbol{P}$	electro-thermal source of thermal nodes/lines
$\mathcal{P}_R, \tilde{\mathcal{P}}_R$	distributed/lumped electro-thermal source of resistor
$P_{\mathrm{in}}, P_{\mathrm{out}}$	optical irradiation power/ optical output power
$Q_C, \widetilde{Q}_C$	charge variable/function of capacitors
Q_S	total charge of semiconductor device
$R, R_{\mathrm{Au}}, R_{\mathrm{SRH}}$	complete/Auger/Shockley-Read-Hall recombination
R_{th}	thermal resistance
S	number of photons
S_L, S_i	transmission function for device/thermal line
$\hat{S}, \hat{\boldsymbol{S}}$	transmission function for lumped element/thermal nodes
T_a, T_L, T_n, T_p	ambient/lattice/electron/hole temperature
T_{env}	temperature of environment
$\hat{\boldsymbol{T}}, \boldsymbol{T}^d$	temperature in thermal nodes/thermal lines
$\tilde{\boldsymbol{T}}^d$	average temperatures in the thermal lines as lumped values
$\boldsymbol{T}^d_0, \boldsymbol{T}^d_1$	left/right boundary values for temperatures in thermal lines
T^d_i	temperature in i-th distributed thermal element
$\hat{\boldsymbol{T}}^l$	temperature in all lumped thermal elements
T^S	semiconductor temperature in thermal network
T^S_D	Dirichlet boundary values for T^S
V	electric potential
$V_{\mathrm{ap}}, V_{\mathrm{bi}}$	applied/built-in potential
V_n, V_p	effective potential for electrons/holes
$V_{B,n}, V_{B,p}$	band potential for electrons/holes
$\hat{V}^l$	physical volume of a lumped thermal element
W, W_p	Fokker-Planck relaxation term for electrons/holes
Ω_S, Ω_c	domain of device/transver cross section of cavity

Appendix B

List of Figures

Bibliography

[1] M. S. Adler. Accurate calculations of the forward drop and power dissipation in thyristors. *IEEE Trans. El. Dev.* 25:16-22, 1970.

[2] G. P. Agrawal and N. K. Dutta. *Semiconductor Lasers. Second Edition.* Van Nostrand Reinhold, New York, 1993.

[3] G. Albinus, H. Gajewski and R. Hünlich. Thermodynamic design of energy models for semiconductor devices. Preprint No. 573. WIAS Berlin, 2000.

[4] G. Alì, A. Bartel, and M. Günther. Parabolic differential-algebraic models in electrical network design. *Multiscale Model. Simul.* 4, 813-838, 2005.

[5] G. Alì, A. Bartel, M. Günther, and C. Tischendorf. Elliptic partial differential-algebraic multiphysics models in electrical network design. *Math. Models Meth. Appl. Sci.* 13, 1261-1278, 2003.

[6] G. Alì, M. Carini. Energy-transport models for semiconductor devices and their coupling with electric networks. *Proceedings to WSCP 2006.*

[7] P. S. André, P. Antunes, A. L. J. Teixeira, and J. L. Pinto. Simplified heat exchange model for semiconductor laser diodes and thermal parameters extraction. *Laser Phys. Lett.* 2, 525-528, 2005.

[8] A. M. Anile, M. Junk, V. Romano and G. Russo. Cross-validation of numerical schemes for extended hydrodynamical models of semiconductors. *M3AS* 6:833-861, 2000.

[9] A. M. Anile, A. Marrocco, V. Romano and J. M. Sellier. 2D numerical simulation of the MEP energy-transport model with a finite elements scheme. *J. Comp. El.* 4:231-259, 2005.

[10] A. M. Anile, V. Romano and G. Russo. Extendend hydrodynamic model of carrier transport in semiconductors. *SIAM J. Appl. Math.* 61:74-101, 2000.

[11] D. Arnold. Mixed finite element methods for elliptic problems. *Comput. Meth. Appl. Mech. Engin.* 82, 281-300, 1990.

[12] G. Baccarani and M. Wordemann. An investigation on steady-state velocity overshoot in silicon. *Solid-State Electr.* 28:407-416, 1985.

[13] U. Bandelow, R. Hünlich and T. Koprucki. Simulation of static and dynamic properties of edge-emitting multipile qunatum-well-lasers. *IEEE J. Sel. Topics Quantum Electron.* 9:798-806, 2003.

[14] U. Bandelow, H. Gajewski and R. Hünlich. Fabry-Perot Lasers: Thermodynamic-Based Modeling. In: J. Piprek (ed.), *Optoelectronic Devices. Advanced Simulation and Analysis.* Springer, Berlin, 63-85, 2005.

[15] U. Bandelow, M. Radziunas, V. Z. Tronciu, H. J. Wünsche, and F. Henneberger. Tailoring the dynamics of diode lasers by passive dispersive reflectors. In: R. H. Binder et al. (eds.), *Physics and Simulation of Optoelectronic Devices VIII.* Proceedings of SPIE 3944, 536-545, 2000.

[16] A. Bartel. *Partial differential-algebraic models in chip design - Thermal and semiconductor problems.* PhD-thesis, Universität Karlsruhe, 2003.

[17] A. Bartel, M. Günther. From SOI to abstract electric-thermal-1D multiscale modeling for first order thermal effects. *Math. Comput. Modell. Dynam. Syst.* 9(1):25-44, 2003.

[18] N. Ben Abdallah, P. Degond and S. Génieys. An energy transport model for semiconductors derived from Boltzmann equation. *J. Stat. Phys.* 84,1:205-231, 1996.

[19] N. Ben Abdallah and P. Degond. On a hierarchy of macroscopic models for semiconductors. *J. Math. Phys.* 37:3308-3333, 1996.

[20] J. Bielefeld, G. Pelz, H. B. Abel and G. Zimmer. Dynamic SPICE-simulation on the electrothermal behaviour os SOI MOSFETs. *IEEE Trans. Elec. Dev.* 42(11): 1968-1995, 1995.

[21] K. Bløtekjær. Transport equations for electrons in two-valley semiconductors. *IEEE Trans. El. Dev.* 17:38-47, 1970.

[22] M. Bodestedt. *Index Analysis of Coupled Systems in Circuit Simulatiom.* Licentiate Thesis, Lund University, Sweden, 2004.

[23] M. Bodestedt and C. Tischendorf. PDAE models for integrated circuits and perurbation analysis. To appear in *Math. Comput. Model. Dynam. Sys.*, 2007.

[24] K. Brennan, S. Campell, and L. Petzold. *Numerical Solution of Initial-Value Problems in Differential-Algebraic Equations.* North-Holland, New York, 1989.

[25] F. Brezzi, M. Fortin. *Mixed and hybrid finite element methods*, Springer, New-York, 1991.

[26] F. Brezzi, L. Marini, S. Micheletti, P. Pietra, R. Sacco, and S. Wang. Discretization of semiconductor device problems. In: W. Schilders and E. ter Maten (eds.), *Handbook of Numerical Analysis. Numerical Methods in Electromagnetics.* Elsevier, Amsterdam, Vol. 13, 317-441, 2005.

[27] D. Chen, E. Kan, U. Ravaioli, C. Shu, and R. Dutton. An improved energy transport model including nonparabolicity and non-Maxwellian distribution effects. *IEEE Electr. Dev. Lett.* 13:26-28, 1992.

[28] P. A. Chen, C. Y. Chang, and C. Juang. Analysis of differential gain in GaAs/AlGaAs quantum well lasers. *J. Appl. Phys.* 76 (1994), 85-91.

[29] W. W. Chow, S. W. Koch, and M. Sargent III. *Semiconductor-Laser Physics.* Springer, 1997.

[30] A. Chryssafis and W. Love. A computer-aided analysis of one-dimensional thermal transients in n-p-n power transistors. *Solid-State Electron.* 22:249-256, 1979.

[31] S. L. Chuang. *Physics of Optoelectronic Devices.* Wiley, New York, 1995.

[32] Crosslight Software Inc. *Crosslight Device Simulation Software Information.* www.crosslight.com, 2005.

[33] P. Degond, S. Génieys, and A. Jüngel. A system of parabolic equations in nonequilibrium thermodynamics including thermal and electrical effects. *J. Math. Pures Appl.* 76, 991-1015, 1997.

[34] P. Degond, A. Jüngel, and P. Pietra. Numerical discretization of energy-transport models for semiconductors with non-parabolic band structure. *SIAM J. Sci. Comp.* 22:986-1007, 2000.

[35] P. Degond, C. D. Levermore and C. Schmeiser. A note on the energy-transport limit of the semiconductor Boltzmann equation. *Proc. of Transport in transition regimes (Minneapolis, MN, 2000)*, IMA Vol. Math. Appl., 135, Springer, 2004.

[36] Ch. Deml, P. Türkes. Fast simulation techniques for power electronic circuits with widely different time constants. *IEEE Trans. on Ind. Appl.* 35(3):657-662, 1999.

[37] K. Einwich, P. Schwarz, P. Trappe, and H. Zojer. Simulatorkopplung für den Entwurf komplexer Schaltkreise der Nachrichtentechnik. In: 7. ITG-Fachtagung "Mikroelektronik für die Informationstechnik", Chemnitz (1996), 139-144.

[38] H. Elschner. Exakte Berechnung der Verlustdichte in Halbleitern. *Nachrichtentech. Elektron.* 29: 415:418, 1979.

[39] D. Estevez Schwarz. *Consistent initialization for index-2 differential algebraic equations and its application to circuit simulation.* PhD thesis, Humboldt-Universität zu Berlin, 2000.

[40] M. Friedrich. *Ein analytisches Modell zur Simulation von Silizium-Germanium Heterojunction-Bipolartransistoren in integrierten Schaltungen.* PhD-thesis, Ruhr-Universität Bochum, 2002.

[41] H. Gajewski and K. Gröger. Semiconductor equations for variable mobilities based on Boltzmann statitics or Fermi-Dirac statistics. *Math. Nachr.*, 140:7-36, 1989.

[42] S. P. Gaur and D. H. Navon. Two-dimensional carrier flow in a transistor structure under nonisothermal conditions. *IEEE Trans. El. Dev.* 23:50-57, 1976.

[43] T. Grasser. *Mixed-Mode Device Simulation.* PhD-thesis, Technische Universität Wien, 1999.

[44] K. Gröger. Initial boundary value problems from semiconductor device theory. *ZAMM*, 67(8):345:355, 1987.

[45] M. Günther and U. Feldmann. CAD based electric modeling in industry. Part I: Mathematical structure and index of network equations. *Surv. Math. Ind.* 8:97-129, 1999.

[46] M. Günther. *Partielle differential-algebraische Systeme in der numerischen Zeitbereichsanalyse elektrischer Schaltungen.* Number 343 in Fortschritt-Berichte VDI, Reihe 20, Rechnerunterstützte Verfahren. VDI Verlag, Düsseldorf, 2001, Habilitation.

[47] M. Günther. A PDAE model for interconnected linear RLC networks. *Mathematical and Computer Modelling of Dynamical Systems* 7(2):189-203, 2001.

[48] M. Günther, U. Feldmann, E.J.W. ter Maten. Modelling and discretization of circuit problems. In: W.H. Schilders and E. J. W. ter Maten (eds.), *Numerical Methods in Electromagnetics*, North-Holland, Amsterdam, 2003.

[49] H.K. Gummel. A self-consistent iterative scheme for one-dimensional steady-state transistor calculations. *IEEE Trans. El. Dev.,* ED-11:455-465, 1964.

[50] E. Hairer and G. Wanner. *Solving Ordinary Differential Equations II.* Springer, Berlin, 1991.

[51] S. Holst. *Mixed Finite-Element Methods for Elliptic Convection-dominated Problems arising in Semiconductor Problems.* PhD-thesis, Johannes Gutenberg-Universität Mainz, 2005.

[52] S. Holst, A. Jüngel, and P. Pietra. A mixed finite-element discretization of the energy-transport equations for semiconductors. *SIAM J. Sci. Comput.* 24, 2058-2075, 2003.

[53] S. Holst, A. Jüngel, and P. Pietra. An adaptive mixed scheme for energy-transport simulations of field-effect transistors. *SIAM J. Sci. Comput.* 25, 1698-1716, 2004.

[54] C.W. Ho, D. A. Ruehli and P. A. Brennan. The modified nodal approach to network analysis. *IEEE Trans. Circuits and Systems* 22(6):504-509, 1975.

[55] G. R. Jones, R. J. Jones and W. French. Infrared HgCdTe Optical Detectors. In: J. Piprek (ed.), *Optoelectronic Devices. Advanced Simulation and Analysis.* Springer, Berlin,381-403, 2005.

[56] A. Jüngel and S. Tang. A relaxation scheme for the hydrodynamic equations for semiconductors. *Appl. Numer. Math.* 56, 899-915, 2002.

[57] A. Jüngel and S. Tang. Numerical approximation of the viscous quantum hydrodynamic model for semiconductors. *Appl. Numer. Math.* 43, 229-252, 2002.

[58] M. Knaipp. *Modellierung von Temperatureinflüssen in Halbleiterbauelementen.* PhD-thesis, Technische Universität Wien, 1998.

[59] K. Konno, O. Matsushima, D. Navarro and M. Miura-Mattausch. *High frequency response of p-i-n photodiodes analyzed by an analytical model in Fourier space.* J. Appl. Phys. 96:3839-3844, 2004.

[60] N. Korneyev, M. Radziūnas, H. J. Wünsche, and F. Henneberger. Mutually injecting semiconductor lasers: simulations for short and zero delay. In: D. Lenstra et al. (eds.), *Semiconductor Lasers and Laser Dynamics.* Proceedings of SPIE 5452, 63-70, 2004.

[61] T. Kujanpää and J. Roos. *Efficient Initialization of Artificial Neural Network Weights for Electrical Component Models* Book of Abstracts

of SCEE 2006, Sinaia, Romania, Sept. 17-22, 2006, pp. 47-48. (The full 12-page paper will be published in a post-conference book.)

[62] R. Lamour. Code for index determination and calculation of consistent initial values for DAEs with tractability index. Online at Humboldt Universität Berlin: URL: *http://www.mathematik.hu-berlin.de/%7ELamour/software/matlab/index.html*.

[63] R. Lamour. *Index Determination for DAEs.* Preprint No. 01-19 Humboldt-University of Berlin, Institut of Mathematics.

[64] R. Lamour. Index determination and calculation of consistent initial values for DAEs. *Computers Math. Appl.* 50, 1125-1140, 2005.

[65] M. E. Levinshtein. *Handbook series on semiconductor parameters.* World Scientific, London, 1996.

[66] W. Li, X. Li, and W.-P. Huang. A traveling-wave model of laser diodes with consideration for thermal effects. *Optical Quantum Electr.* 36, 709-724, 2004.

[67] J. Litsios, B. Schmithüsen, U. Krumbein, A. Schenk, E. Lyumkis, B. Polsky, and W. Fichtner. *DESSIS 3.0 Manual*. ISE Integrated Systems Engineering, Zürich, 1996.

[68] M. Lundstrom. *Fundamentals of carrier transport.* Second edition. Cambridge Universtity Press, Cambridge, 2000.

[69] R. März. Numerical methods for differential-algebraic equations. *Acta Numerica* (1992), 141-198.

[70] R. März. Differential algebraic systems anew. *Appl. Num. Math.* 42:315-335, 2002.

[71] R. März. Differential algebraic systems with properly stated leading term and MNA-equations. Technical Report 2002-13, Institut für Mathematik, Humboldt-Universität zu Berlin, 2002.

[72] L. D. Marini and P. Pietra. New mixed finite element schemes for current continuity equations. *COMPEL* 9, 257-268, 1990.

[73] P. A. Markowich, C. A. Ringhofer and C. Schmeiser. *Semiconductor Equations*. Springer, 1990.

[74] E. Medina and M. Pagani. *Multi-Physics modeling and numerical simulation of electrothermal effects in semiconductor devices.* Master-thesis, Politecnico di Milano, 2006.

[75] P. M. Morse and H. Feshbach. *Methods of Theoretical Physics.* McGraw-Hill, New York, 1953.

[76] L. W. Nagel. SPICE2: A computer program to simulate semiconductor circuits. Technical Report UCB/ERL M520, University of California, Berkeley, 1975.

[77] K. Pipe, R. Ram, and A. Shakouri. Bias-dependent Peltier coefficient and internal heating in bipolar devices. *Phys. Rev. B* 66(12):125316, 2002.

[78] J. Piprek. Semiconductor optoelectronic devices. Academic Press, Amsterdam, 2003.

[79] J. Piprek and S. Li. GaN-based Light-Emitting Diodes. In: J. Piprek (ed.), *Optoelectronic Devices. Advanced Simulation and Analysis.* Springer, Berlin, 293-312, 2005.

[80] F. Poupaud. Diffusion approximation of the linear semiconductor Boltzmann equation. *J. on Asymp. Anal.* 4:293-317, 1991.

[81] W. Van Roosbroeck. Theory of flow of electrons and holes in germanium and other semiconductors. *Bell Syst. Techn. J.* 29:560-607, 1950.

[82] F. Rotella. *Mixed circuit and device simulation for analysis, design, and optimization of opto-electronic, radio frequency, and high speed semiconductor devices.* PhD thesis, Stanford University, 2000.

[83] D. Scharfetter and H. K. Gummel. Large-signal analysis of a silicon Read diode oscillator. *IEEE Trans. Elec. Dev.* ED-16:64-77, 1969.

[84] C. Schmeiser and A. Zwirchmayr. Elastic and drift-diffusion limits of electron-phonon interaction in semiconductors. *Math. Models Meth. Appl. Sci.* 8:37-53, 1998.

[85] D. Schroeder. *Modeling of Interface Carrier Transport for Device Simulation.* Computational Microelectronics, Springer, 1990.

[86] D. K. Schroder. Carrier lifetimes in silicon. *IEEE Trans. Electron Dev.* 44(1):160-170, 1997.

[87] S. Selberherr. *Analysis and simulation of semiconductor devices.* Springer, 1984.

[88] M. Selva Soto and C. Tischendorf. Numerical analysis of DAEs from coupled circuit and semiconductor simulation. *Appl. Numer. Math.* 53:471-488, 2005.

[89] D. K. Sharma and K. V. Ramanathan. Modeling thermal effects on MOS I-V characteristics. *IEEE Electron. Dev. Lett.* EDL-4:362-364, 1983.

[90] H. Spiro. *Simulation integrierter Schaltungen.* Oldenburg, 1990.

[91] A. Stach. Simulation von MOSFET-Schaltungen. Diplomarbeit, Technische Universität Wien, 1996.

[92] R. Stratton. Diffusion of hot and cold electrons in semiconductor barriers. *Phys. Rev.* 126:2002-2014, 1962.

[93] G. Suzuki, K. Konno, D. Navarro, N. Sadachika, Y. Mizukane, O. Matsushima, and M. Miura-Mattausch. Time-domain-based modeling of carrier transport in lateral p-i-n photodiode. *Proceedings of the International Conference of Semiconductor Processes and Devices (SISPAD 2005)*, 107-110.

[94] T. N. Swe and K. S. Yeo. An accurate photodiode model for DC and high frequency SPICE circuit simulation. In: *Technical Proceedings of the 2001 International Conference on Modeling and Simulation of Microsystems*, Nanotech 2001 Vol. 1, 362-365, 2001.

[95] U. Tietze and C. Schenk. *Halbleiter-Schaltungstechnik.* Springer, Berlin, 1970.

[96] C. Tischendorf. *Solution of Index-2 Differential-Algebraic Equations and its Application to Circuit Simulation.* PhD thesis, Humboldt-Universität zu Berlin, 1996.

[97] C. Tischendorf. Topological index calculation of differential-algebraic equations in circuit simulation. *Surveys Math. Industr.* 8:187-199, 1999.

[98] C. Tischendorf. Modeling circuit systems coupled with distributed semiconductor equations. In: K. Antreich, R. Bulirsch, A. Gilg, and P. Rentrop (eds.), *Modeling, Simulation, and Optimization of Integrated Circuits*, Internat. Series Numer. Math. 146:229-247, 2003.

[99] C. Tischendorf. *Coupled systems of differential algebraic and partial differential equations in circuit and device simulations.* Habilitation thesis, Humboldt Universität zu Berlin, 2003.

[100] G. Wachutka. Rigorous thermodynamic treatment of heat generation and conduction in semiconductor device modeling. *IEEE Trans. CAD* 9:1141-1149, 1990.

[101] G. Wachutka. Consistent treatment of carrier emission and capture kinetices in electrothermal and energy transport models. *Microelectronics Journal* 26:307-315, 1995.

[102] P. Wen, M. Sanchez, M. Gross, O. Kibar, S. C. Esener. New photon density rate equation for Fabry-Perot semiconductor optical amplifiers (FP SOAs). In: P. Blood et al. (eds.), *Physics and Simulation of Optoelectronic Devices X*. Proceedings of SPIE 4646:243-250, 2002.

[103] A. Yamnahakki. Second-order boundary conditions for the drift-diffusion equations for semiconductors. *Math. Models Meth. Appl. Sci.* 5, 429-455, 1995.

Index